CONTROL ANALYSIS OF INTEGRATED FUEL CELL SYSTEMS WITH ENERGY RECUPERATION DEVICES

by

Vasilios Tsourapas

A dissertation submitted in partial fulfillment
of the requirements for the degree of
Doctor of Philosophy
(Naval Architecture and Marine Engineering)
in The University of Michigan
2007

Doctoral Committee:
Associate Professor Jing Sun, Co-Chair
Professor Anna G. Stefanopoulou, Co-Chair
Professor Michael G. Parsons
Associate Research Scientist Michael Kokkolaras

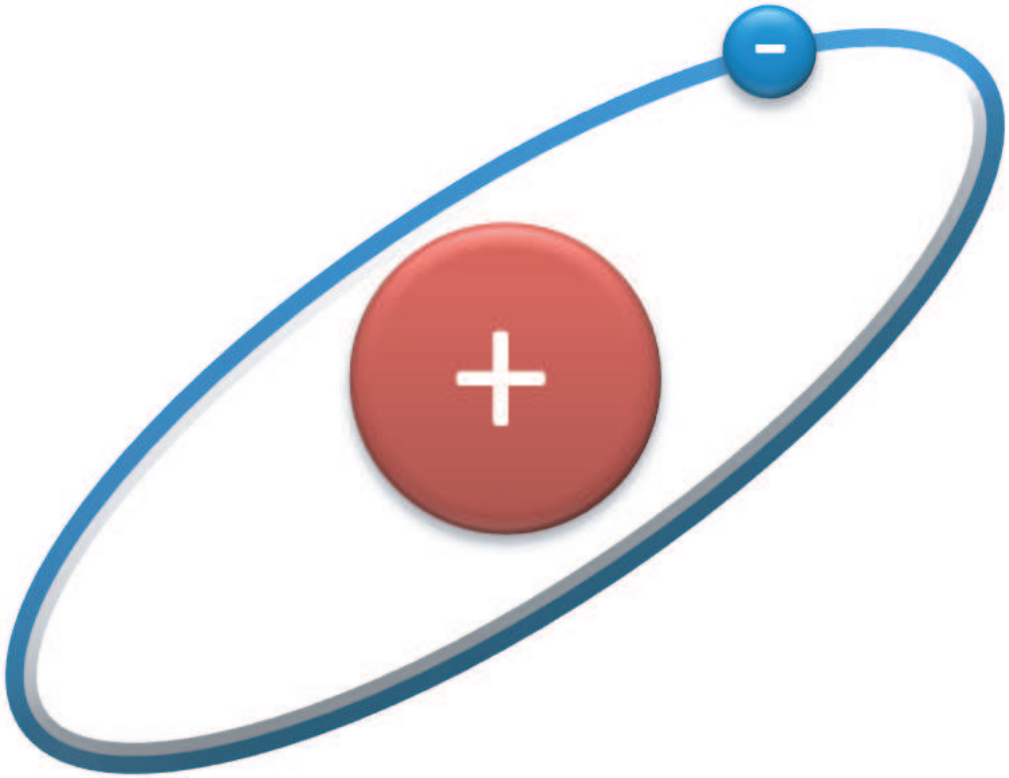

Hydrogen is the most abundant element in the Universe

To my parents

ACKNOWLEDGEMENTS

It has been almost four years (Sep 2003 - May 2007) since I started my Ph.D. study at the University of Michigan. This work would not have been possible without the help and support of my family, professors, lab-mates and friends.

I would like to express my gratitude to my academic advisors, Professor Jing Sun and Professor Anna Stefanopoulou, for their guidance throughout those four years. Their insights and suggestions made this work possible. Even though my productivity had its ups and downs, their continuous support and patience allowed the completion of my goal. Also, I would like to thank the members of my Ph.D. committee, Professor Michael Parsons and Dr. Michael Kokkolaras, who were a great resource for suggestions and encouragement.

All my friends and colleagues were a valuable support for helping me overcome significant obstacles in my research. I would especially like to thank Handa Xi, Amey Karnik, Gayathri Seenumani, Reza Ghaemi and the rest of the RACE lab mates, Denise McKay and the rest of the Fuel Cell Control Systems Laboratory mates and finally my loving half, Ana-Maria, and friends Stelios Paparizos and Dimitris Delis amongst many others.

I also like to acknowledge the Office of Naval Research, the U.S. Army, United Technologies, the Department of Defense, the Automotive Research Center of the University of Michigan and the Naval Architecture and Marine Engineering Department of the University of Michigan for their financial support towards my Ph.D. research.

Finally, the biggest thanks goes to my family, my dad, mom and sister, who even though they 5000 miles away, they were what kept me pursuing and struggling for accomplishing my goal.

TABLE OF CONTENTS

LIST OF FIGURES

Figure

LIST OF TABLES

Table

NOMENCLATURE

IHPS model nomenclature

Symbol

A_{cell}	Area of each cell in FC stack
F	Farraday's Constant
I_{st}	FC Current
M	Molar weight
N_{cell}	Number of cells in FC stack
P	Pressure
Q	Heat
Q_{LHV}	Lower Heating Value
Q_{obs}	Observability gramian
R	Gas Constant
T	Temperature
U_{H_2}	H_2 FC Utilization
V	Volume
W	Mass Flow
ΔH	Enthalpy of formation
η	Efficiency
c_P	Specific Heat
m	Mass
u_a	Air Setpoint
u_f	Fuel Setpoint
x	Mass fraction

Sub(Super)scripts

CH_4 or f	Methane
H_2	Hydrogen
O_2	Oxygen
*	Denotes Optimal/Desired Values
a	Air
bed	Property of the reactor bed
in	Incoming flow Property
nom	Nominal Value
out	Outgoing flow Property
ref	Reference Value

Acronyms

FC	Fuel Cell
FPS	Fuel Processor System
an/AN	Anode
bl/BL	Blower
cb/CB	Catalytic Burner
$cpox/CPOX$	Catalytic Partial Oxidizer
hds/HDS	Hydro-Desulphurizer
$hex\ h/c\ /HEX$	Heat exchanger hot/cold side
mix/MIX	Mixer
$tank$	Tank
$wrox/WROX$	Water Gas Shift & Preferential Oxidizer

SOFC/GT model nomenclature

Symbols

η_{hc}	Compressor isentropic efficiency
η_{ht}	Turbine isentropic efficiency
c_P	Heat capacity (J/kgK)
A_c	Cell area (m^2)
E	Energy (J)
H_{abs}	Absolute enthalpy (J/mole)
I_{st}	Stack current - input (A)
i	Current density (A/m^2)
J	Shaft inertia (kgm^2)
k	Orifice Coefficient ($kg/sPa^{0.5}$)
m	Mass (kg)
M	Molar Weight (kg/mole)
N	Shaft rotational speed (rpm)
p	Pressure (Pa)
P_{gen}	Generator power - input (W)
P_{net}	Net power output (W)
P^d_{net}	Net power demand (W)
P_{fc}	Fuel Cell Power output (W)
P_c	Compressor power (W)
P_t	Turbine power (W)
R	Universal Gas Constant (J/K.mole)
T	Temperature (K)
U_{st}	Stack voltage (V)
V	Volume (m^3)
$c_{(\cdot)}$	Concentration of species $(\cdot)$ (mole)
W	Flow (kg/s)

Abbreviations

C	Compressor
CB	Catalytic burner
FOM	Full order model
GEN	Generator
RoA or R_A	Region of attraction
ROM	Reduced order model
SOFC	Solid oxide fuel cell
T	Turbine

ABSTRACT

CONTROL ANALYSIS OF INTEGRATED FUEL CELL SYSTEMS WITH ENERGY RECUPERATION DEVICES

by

Vasilios Tsourapas

Co-Chairs: Jing Sun and Anna G. Stefanopoulou

This work is focused on control-oriented analysis of integrated fuel cell systems that incorporate energy recuperation mechanisms. The high complexity of such fuel cell systems calls for precise control and regulation of multiple inputs. The need for robust and efficient steady state and transient operation imposes the need for intelligent control schemes. The models of two fuel cell systems are developed in this work and used for the design of feedback controllers. It is shown, through simulation, that the proposed controllers enhance the performance and meet the operating constraints.

The two plants considered in this dissertation are (i) a catalytic partial oxidation fuel processor system (FPS) coupled with a proton exchange fuel cell and a catalytic burner (CB) and (ii) a hybrid solid oxide fuel cell and gas turbine (SOFC/GT) system. Both systems rely on energy recuperation devices (ERDs), such as a catalytic burner or a gas turbine, for achieving high fuel efficiency. Through model-based open loop analysis the FPS is shown to exhibit fuel cell H_2 starvation and reactor overheating while the SOFC/GT system is prone to shutdown during load transitions without proper feedback in place. It is identified that the transient issues can be resolved through reactant ratio control and load filtering for the FPS and the SOFC/GT systems, respectively.

Using the insights from the open loop analysis, feedback control schemes are designed to address the transient issues. For the FPS, an observer-based linear controller, that utilizes temperature measurements to control the air and fuel flows into the reformer and maintain proper reactant ratios, is proposed. For the SOFC/GT system, a reference governor control scheme is developed to filter the application of the load in order to avoid GT shutdown.

For both systems, the designed control schemes utilize measurements from the ERDs, such as shaft speed or catalytic burner temperature and manage to mitigate the transient operating difficulties. Thus, the ERDs, besides increasing the steady state efficiency of the system by reducing the energy losses, also provide vital measurements for feedback control.

CHAPTER 1

Introduction

1.1 Overview of Integrated Fuel Cell Systems with Energy Recuperation Devices

Fuel cell (FC)-based power plants exhibit high efficiency and low emissions compared to conventional power production plants such as diesel or gasoline engines [7, 24, 27]. In addition, other features enabled by the fuel cell technology, such as efficient electric power distribution, reconfigurability, silent operation and low thermal acoustic signature make fuel cell power plants ideal candidates for military and commercial applications. Integrating fuel cell-based systems with energy recuperation devices (ERDs) can further improve the system's efficiency by reducing the exhaust energy losses. The process of recovering additional energy from the exhaust gases of a power plant, in our case a fuel cell, is commonly referred to as energy recuperation. A typical example of an integrated fuel cell system with energy recuperation devices is shown in Fig. 1.1. The significant amount of energy in the exhaust gases makes fuel cell systems suitable for energy recuperation. The energy recuperated can be utilized both internally in the fuel cell system, for example in the fuel reformer, or externally, for example in a generator, to provide additional power output. In general, the higher the dependency of the FC system and its auxiliaries to the recuperated energy, the higher the operational complexity and control requirements of the integrated system.

Energy recuperation is critical in achieving high system efficiency and in assuring minimal losses to the environment. Fuel cell systems are ideal candidates for incorporating energy recuperation devices for several reasons. In order to promote the fuel cell efficiency and avoid hydrogen starvation issues, fuel cell stacks do not operate at fuel utilization ratios close to 100% [76, 78, 86]. Thus, a portion of the fuel provided to the fuel cell will be wasted unless it is recuperated back to the fuel cell. Significant amounts of energy can be recuperated by harvesting the remaining hydrogen in the exhaust, given the high heating value of hydrogen. Furthermore, high temperature fuel cells, such as the solid oxide fuel cells, are rich in exhaust energy, given the high exhaust temperature, and thus ERDs can promote the SOFC system efficiency significantly. Finally, using the recuperated energy to

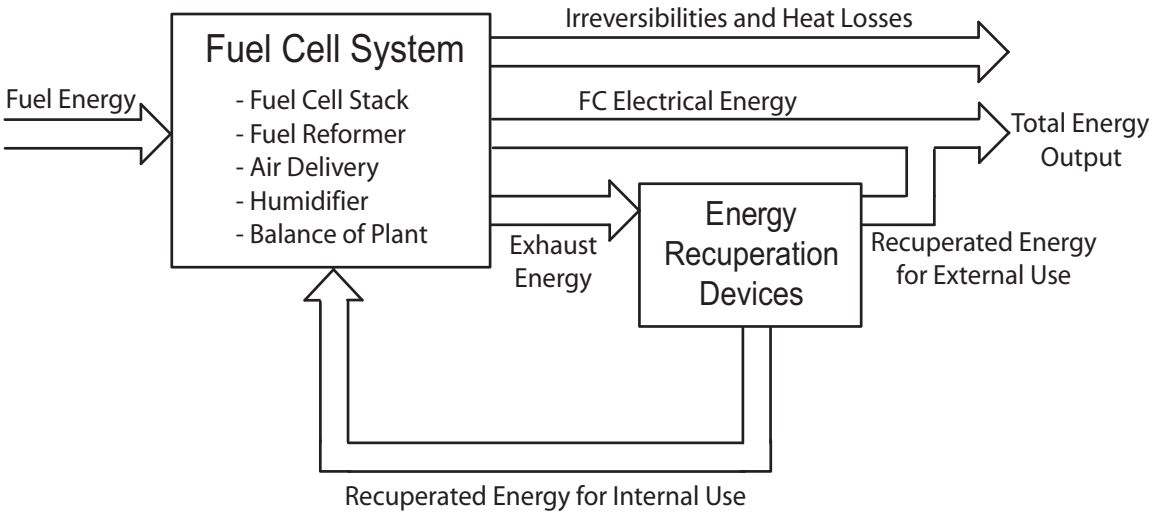

Figure 1.1: Energy flow of Integrated Fuel Cell System with Energy Recuperation Devices

preheat the inlet fuel and air flows to the reformer will increase the hydrogen production efficiency.

The main devices used to facilitate energy recuperation in integrated fuel cell systems include ejectors for flow recirculation, heat exchangers, catalytic burners and gas turbines. Combinations of those devices, such as a catalytic burner and a gas turbine, are also used. Most common combinations include a proton exchange membrane fuel cell (PEM-FC) with an ejector [5], a PEM-FC with a catalytic burner and a heat exchanger [83] or a solid oxide fuel cell with a catalytic burner and a gas turbine [79].

The coupling of fuel cells with energy recuperation devices has been studied extensively in the literature motivated by the substantial energy saving benefits of ERDs. Multiple studies show that the steady state efficiency increases when energy recuperation devices are integrated in a fuel cell system [33, 36, 63]. Also, due to the multiplicity of configurations and types of ERDs, a significant amount of publications deal with optimizing the configuration and the steady state parameters with respect to the system's efficiency and safe steady state operation [6, 14, 43]. Publications dealing with the transition dynamics of the system (i.e., the system's response under changes in the demanded power), though, are limited. The intricate power balance between the FC system and the ERDs during load transitions, especially in the case where the FC system auxiliaries depend heavily on the recuperated energy, has not been thoroughly analyzed in the literature. Dynamic analysis on similar systems, such as integrated gasoline engines with turbochargers, can be found in the literature where the limitation in transient performance are examined [31, 62]. Similar issues, such as the turbocharger lag encountered in the transient operation of engine-turbocharger systems, are shown to exist in the FC-ERD systems as well. The fundamental operational challenges of integrated FC and ERD systems are discussed in the next section, while more detailed overview of the literature dealing with the two systems examined in this dissertation is given

in Ch. 2 and Ch. 4.

1.2 Operational Challenges of Integrated Fuel Cell Systems and Energy Recuperation Devices

The operational challenges in fuel cell systems arise from two competing goals, namely, the optimization of the steady state efficiency versus the fast and safe load transitions. On one hand, in order to maximize fuel cell efficiency one has to minimize fuel consumption for a given load or to maximize power production for a given fuel supply. On the other hand, the system has to operate with a sufficient safety margin to allow for fast and safe load transitions. This margin can be provided if the fuel cell is operating at lower fuel utilization (less than 100%). With the incorporation of energy recuperation devices, one can operate at lower FC utilizations while maintaining high system efficiency by recovering most of the energy in the fuel cell exhaust gases. Therefore, energy recuperation devices facilitate the achievement of improved trade off between steady state and transient operations, compared to FC systems with no ERDs.

However, the integration of energy recuperation devices and fuel cell systems imposes a number of unique challenges in terms of system operation. The tight thermal and mechanical coupling between the FC and the ERDs affects the system dynamics and inflicts constraints that require intelligent control schemes. Extensive analysis and system optimization is required to balance the added system complexity and the increased capital cost that arise from the ERDs with the efficiency gains. Furthermore, the integration of multiple components poses challenging sizing optimization problems not only for the system's steady state operation, but for the load transitions as well.

In general, fuel cell systems with energy recuperation devices are limited by the speed and efficiency of the energy recuperating devices. The operational challenges are distinct depending on the type of energy recuperation and the corresponding dynamics of the dynamic couplings between the FC and the ERD. As mentioned earlier, a portion of the recuperated energy can be used internally in the FC system. The higher the percentage of the internally used recuperated energy, the higher the dependency of the FC system operation to the ERD. Due to the fast FC dynamics, the fuel in the FC is depleted almost instantaneously during load transitions, leaving a limited amount of fuel for the energy recuperation devices. Thus, if the FC system is highly dependent on the ERD, its performance can be compromised during load transitions. Both of the systems examined in this work utilize a large portion of the recuperated energy for internal use and are shown in Fig. 1.2a and b. On the other hand, the configurations shown in Fig. 1.2c and d, utilize the recuperated energy to provide additional power output, while the auxiliary devices in the FC system are powered directly by consuming fuel. In this case there is no feedback from the ERD to the FC system and the system efficiency is lower.

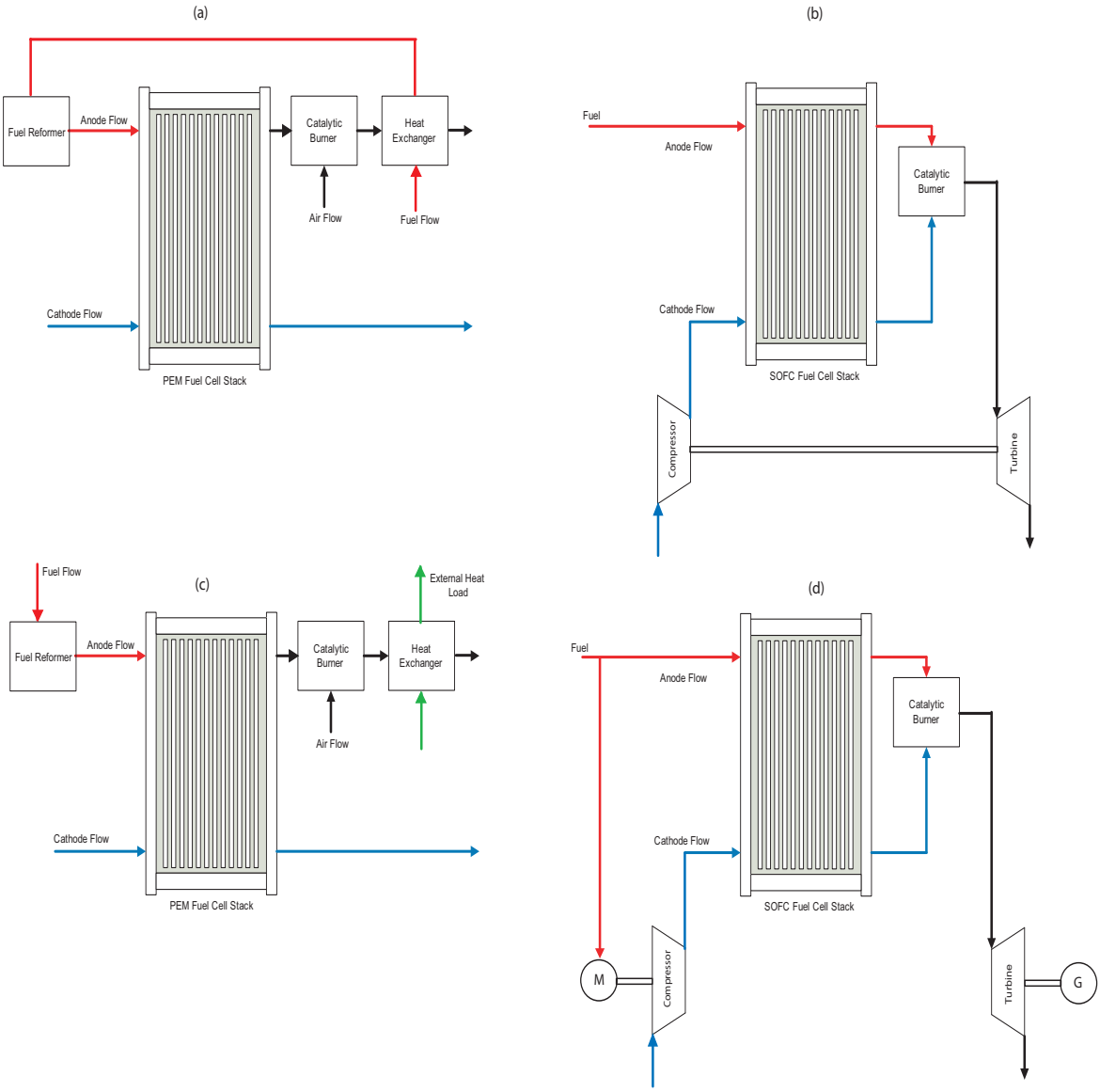

Figure 1.2: Examples of energy recuperation schemes with internally (a,b) and externally (c,d) utilized recuperated energy

The first system examined in this dissertation (Fig. 1.2a) incorporates a catalytic partial oxidizer (CPOX), which reforms methane fuel into a hydrogen rich flow to be utilized by a proton exchange membrane fuel cell (PEM-FC). It also includes a catalytic burner (CB) that burns any excess hydrogen that leaves the fuel cell to recuperate energy. The second system, shown in Fig. 1.2b, is a hybrid consisting of a Solid Oxide Fuel Cell (SOFC) coupled with a gas turbine (GT) for energy recuperation. The GT is the only actuator available to indirectly control the air into the fuel cell.

The coupling between the FC and the ERD can be dominated either by slow dynamics, such as temperature (Fig. 1.2a), or fast dynamics, such as pressure (Fig. 1.2b). For the first system examined (Fig. 1.2a), where the ERD recovers heat from the exhaust gases, the recuperation efficiency is lower compared to the second system (Fig. 1.2b) since in general a heat exchanger is less efficient than a turbine. At the same time though, the transient operation of the first system is safer due to the large thermal inertia which provides a desirable buffer that helps prevent a significant undershoot in recuperated energy during load transitions. For the second system (Fig. 1.2b), the fast pressure dynamics that dictate the energy recuperation and in turn the air supply to the FC are shown to compromise transient operation and even lead to shutdown of the system during large load steps. Thus, for the two systems examined it can be seen that transient operation issues are more prominent for those with high steady state efficiency.

The challenges of integrated fuel cell systems together with the technical issues associated with component protection, such as reactor overheating, and optimal operation are addressed in this work via model-based analysis. Following the open loop analysis, where the issues are identified and analyzed, feedback control schemes are designed and analyzed to mitigate the transient issues while allowing for optimal steady state operation. The next section outlines the fuel cell and fuel reforming technologies examined in this work.

1.3 Components of Fuel Cell Systems

Besides the energy recuperation devices, the fuel cell system incorporates the fuel cell stack, the fuel reformer, the air delivery system, the humidifier as well as other balance of plant components such as blowers or heat exchangers. In this dissertation the humidification process is not the focus and is thus assumed perfect (i.e., constant inlet humidification). A brief introduction on the other main subsystems incorporated in this work is given in this section.

1.3.1 Fuel Cell Stack

In this dissertation two types of fuel cells are considered; namely, a proton exchange membrane (PEM) fuel cell and a solid oxide fuel cell (SOFC). The main differences lie in the operating temperature and the fuel used as explained in the subsequent paragraphs.

As noted in [40], the PEM fuel cell capitalizes on the essential simplicity of a fuel cell. The electrolyte is a solid polymer in which the protons are mobile. These cells run at low temperatures and thus face issues with current limitations due to the slow reaction rates. The slow reaction rates are addressed by using sophisticated catalysts and electrodes. Platinum is the most common catalyst used in PEM fuel cells, but technology developments in recent years allow the use of very small quantities of platinum. Pure hydrogen must be used to fuel the PEM fuel cell and various methods for producing hydrogen exist. In this work we focus on catalytic partial oxidation of methane.

The solid oxide fuel cell addresses the issue of slow reaction rates by operating at temperatures in the region of 600 ^{o}C to 1000 ^{o}C. The high operating temperature brings new issues to the manufacturing and safe operation of the system but ensures high reaction rates without expensive catalysts. Furthermore, gases such as natural gas can be used directly as fuels without the need for a separate reformer unit. This is enabled by the internal reforming process where the fuel can be reformed internally in the SOFC. Nevertheless, due to the high temperatures, the ceramic materials that these cells are made from are difficult to handle and expensive to manufacture. Finally, other components such as the preheating and the cooling systems add to the complexity of SOFC-based plants.

More details on the operation and the modeling of the the PEM-FC and the SOFC are give in Ch.2 and Ch.4, respectively.

1.3.2 Fuel Reformer

A common way of fueling FC-based power plants, besides pressurized hydrogen tanks, is onboard fuel reforming. This option is utilized for large scale power production such as marine or stationary power plants. For automotive applications, onboard fuel processing has been ruled out by most automotive companies due to space and system complexity constraints.

The three most common techniques for reforming hydrocarbon fuels for fuel cell applications include: Catalytic Partial Oxidation (CPOX), Steam reforming (SR) and Autothermal reforming (ATR). CPOX reformers exhibit lower conversion efficiency but reduced capital cost (25-30% less) and fast transient response compared to the other types of reformers [92]. The catalytic partial oxidation process is described in detail in Ch. 2 while a schematic indicating the main oxidation reactions is shown in Fig. 1.3.

In the CPOX-based reformer examined in this work, besides the oxidation reactor, other equally important reactors are included in a fuel reforming system to remove impurities and other species that will poison the oxidation reactor or the fuel cell stack[1].These include:

- Desulphurizer (DS) Reactor: The desulphurization of the fuel flow, i.e., removing the sulphur content present in the flow, is vital for fuel cell-based systems. Sulphur is

[1]Note that the CPOX system considered here is for hydrogen production to be utilized in a low temperature proton exchange fuel cell system

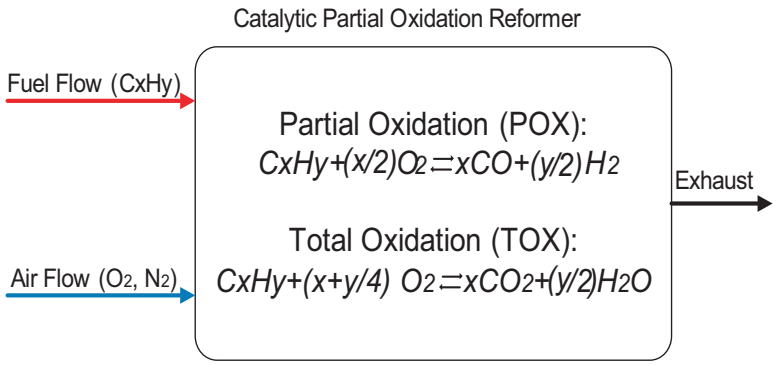

Figure 1.3: CPOX reformer schematic with corresponding main oxidation reactions

known to poison the fuel cell membrane as well as catalyst bed of the reformer reactors. The sulphur tolerance of different reactors varies, but all reactors are relatively sensitive to sulphur.

- Water Gas Shift (WGS) Reactor: Water gas shift removes the carbon monoxide (CO), a by-product of the hydrogen producing reactions. The WGS reaction is given below:

$$CO + H_2O \rightleftharpoons CO_2 + H_2 \tag{1.1}$$

where water reacts with the CO in the flow producing CO_2 and hydrogen. Note that the water gas shift reaction produces additional amount of hydrogen which increases the efficiency of the reformer.

- Preferential Oxidizer (PROX) Reactor: Similar to WGS reaction, preferential oxidation is used to remove any CO remaining in the flow. The PROX reaction is given as:

$$CO + \frac{1}{2}O_2 \rightleftharpoons CO_2 \tag{1.2}$$

where the CO is oxidized to CO_2.

- Hydrogen Separator Membrane: To fortify the fuel cell stack against any impurities, including CO, sulphur etc., it is beneficial to filter the reformer flow through a separator membrane. The separator membrane extracts hydrogen from the reformate flow, resulting in pure hydrogen flow (up to 99.9%) [56]. The rest of the reformate, after the hydrogen has been extracted, can be utilized in energy recuperation devices such as a combination of a catalytic burner and a gas turbine where the remaining species can be utilized. The main type of hydrogen separators are palladium based which extract the hydrogen via diffusion.

1.3.3 Air Delivery Subsystem

The air is an equally important reactant as the fuel in a fuel cell system. Air is required both in the fuel cell stack for the electrochemical reaction that produces the electricity and for the reformer in order to oxidize the fuel and produce the hydrogen. The air delivery is commonly done via a blower for low pressure FC systems or a compressor for high pressure (and usually high temperature) FC systems. For the reformer system examined, the air supply to the reformer is the main focus while the air supply to the FC is assumed perfect. In the case of the high temperature FC system examined in this work, the air flow to the SOFC is the main focus, which also provides a means for temperature regulation and heat removal from the SOFC.

1.4 Dissertation Overview

In this dissertation, two fuel cell-based power plants are analyzed to gain fundamental understanding on the efficiency, transient operation and control requirements of such integrated FC systems. The first system, shown in Fig. 1.2c includes a fuel processor system (FPS) used to reform methane fuel into a hydrogen rich flow to be utilized in a proton exchange membrane fuel cell. The exhaust from the fuel cell is then fed to a catalytic burner to recuperate heat for preheating the inlet air and fuel flows. The second system is a hybrid solid oxide fuel cell and gas turbine (Fig. 1.2b). The gas turbine recuperates energy to provide the air flow through a compressor and yields additional electrical load through a generator. Both systems incorporate energy recuperation devices in order to optimize the overall efficiency efficiency. These energy recuperation devices, besides increasing the system's overall steady state efficiency, are also shown to be important in the control design by providing vital measurements for feedback.

The fuel processor system is analyzed in Chapters 2 and 3. In Ch. 2 the modeling and steady state optimization results are presented. It is shown that in open loop operation the system exhibits reactor overheating and hydrogen starvation in the fuel cell. The causes are identified and mitigation strategies are presented in Ch. 3, where a feedback controller is designed and shown to be robust under various scenarios such as large pressure uncertainty during reactor clogging.

The hybrid SOFC/GT system is analyzed in Chapters 4 through 6. In Ch. 4, the modeling principles and governing equations for the main components are presented. In Ch. 5, the open loop analysis is used to explain shutdown phenomena during large load transitions. It is shown that the shutdown is initiated by the nonlinear shaft dynamics while the characteristics of the shutdown phenomena are examined. Chapter 6 presents the feedback control design which includes a reference governor controller combined with a proportional controller that guarantees stability and improves performance.

Finally, in Ch. 7 a summary of the dissertation is given and the important conclusions

are listed.

1.5 Contributions

The contributions of this dissertation on modeling and control of integrated fuel cell systems are summarized as follows:

1. Control-oriented dynamic models of two integrated fuel cell based power systems are developed. Namely, models of an integrated catalytic partial oxidation reformer with a proton exchange fuel cell (CPOX-PEM FC) and a hybrid solid oxide fuel cell with a gas turbine (SOFC-GT) are developed within the scope of this work. Component models are integrated to represent the overall system dynamics.

2. Overall system efficiency is optimized by determining the operating setpoints for each actuator, such as air, fuel etc. For the reformer-based system and the hybrid SOFC/GT an average efficiency of 30% and 60% are achieved, respectively. The steady state trends of various system variables, such as the reactor temperature and the cell voltage, are analyzed with respect to the load applied to the system. It is shown that optimization along with energy recuperation pushes the system to its limits and affects transient response. Finally, the values of the operating variables using the optimal setpoint are determined and utilized in the control design as regulation points.

3. Open loop analysis is performed to identify the load following limitations and their underlying issues. Load transition issues such as reactor temperature overshoot and hydrogen starvation are identified for the reformer-based system while shutdown is identified for the hybrid SOFC/GT system. Further insights are gained by determining the root causes of these transient issues. Reactant ratio discrepancies and shaft dynamics nonlinearities are shown to be the causes for the open loop issues identified in the reformer and the hybrid SOFC/GT system, respectively. The identification of the causes facilitates the control design and analysis.

4. Feedback control schemes are designed to mitigate the issues identified in the open loop analysis. For the CPOX-based reformer, a linear control scheme is proposed that utilizes temperature measurements, namely the CPOX reactor temperature and the CB reactor temperature. It is worth noting that the CB temperature measurement is utilized as a virtual hydrogen sensor in order to estimate the amount of hydrogen produced by the reformer. The feedback control results in a fourfold improvement in transient response compared to the open loop case and in addition, it mitigates the reactor overheating and the hydrogen starvation. For the SOFC/GT hybrid system a reference governor controller is designed to throttle the application of the generator

load and meet certain constraints (in our case the constraint is maintaining stability). In order to improve the transient response, the load governor is combined with a proportional controller that regulates the amount of fuel fed to the system in order to support the increasing generator load. Overall the settling time is reduced twofold compared to the response of the open loop system that incorporates a rate limiter.

5. A reference governor controller is proposed to filter the load applied to the generator on the hybrid SOFC/GT system. The conventional reference governor approach requires online optimization via repeated simulations in order to define the reference command. In this dissertation, a novel reference governor controller is proposed, referred to as Incremental Step-Reference Governor (IS-RG), which utilizes the offline calculated region of attraction to determine the feasibility of a desired input. Significant computational efficiency improvement is achieved that makes real time implementation of the IS-RG is possible.

6. Finally, robustness evaluation is performed for the closed loop reformer system in order to verify the controller operation under different uncertainty scenarios. The scenarios examined include, CPOX reactor and HDS reactor clogging in which the transient closed loop response is examined when carbon deposition or catalyst deformation causes clogging of the CPOX or HDS reactors and results into increased pressure drop. Also, the effects of multiple methane compositions are considered with respect to the transient reactor temperatures and hydrogen production. Finally the effects of discrepancies between the actual CB and the CB model used in the state observer, were analyzed. The controller was shown to perform satisfactory under these scenarios and the transient system response did not deteriorate significantly.

CHAPTER 2

Modeling and Open Loop Analysis of a Fuel Processor with Exhaust Heat Recirculation

2.1 Introduction

In this chapter we consider the fuel cell-based system with exhaust heat recirculation, referred to as internally heated power system (IHPS) (Fig. 2.1a). The IHPS results from the integration of an FC stack that generates electric power, an FPS that produces a hydrogen rich mixture to be fed to the fuel cell, and a CB that utilizes any excess hydrogen leaving the FC to provide preheating energy. The closely coupled dynamics of the three subsystems, together with the large thermal inertia and therefore slow transients associated with the fuel processor, impose a very challenging control problem. For cross reference the externally heated power system (EHPS) is also shown in Fig. 2.1b, where the energy needed for preheating is provided by burning fuel directly from the fuel tank. Optimization is performed for the IHPS to generate the air and fuel flow intake setpoints to the FPS for various load levels. The optimal flow setpoints are used in a static feedforward map that ensures maximum efficiency at steady-state.

The natural gas fuel processor considered here, is based on a catalytic partial oxidation (CPOX) reactor [57]. The fuel processor is responsible for supplying hydrogen to the FC stack to support the current drawn. Typically excess hydrogen is necessary to (i) avoid lack of hydrogen, also known as hydrogen starvation in the FC stack, (ii) allow the FC to operate at higher hydrogen concentration, and thus higher stack efficiency. Operating with excess hydrogen provides also a buffer during fast load changes. While excess hydrogen supply is beneficial for the FC, it however decreases the overall system (FPS+FC) efficiency and requires safe discharge measures, such as adequate ventilation or burning of anode exhaust gas.

One way to eliminate the excess hydrogen that does not participate in the electrochemical reactions and, at the same time, increase the system efficiency is to use it in a reactor after it exits the FC anode exhaust. Specifically, a catalytic burner (CB) can harvest energy from the excess hydrogen via oxidation with air. This energy can be then used to preheat

the FPS inlet flows. For steady state operation, as much as 16% efficiency improvement can be achieved when the excess hydrogen in the FC exhaust is burnt in a CB instead of burning a dedicated and separate stream of natural gas in a CB (as shown in the two schematics in Fig. 2.1) to provide energy for preheating the inlet fuel and air streams to the FPS [77].

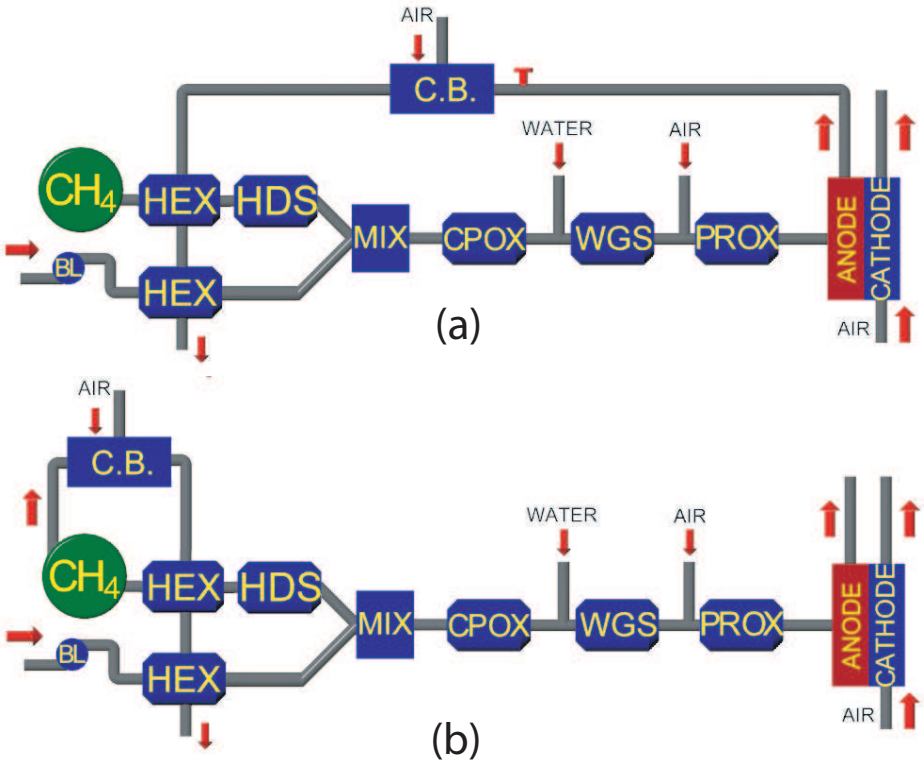

Figure 2.1: (a) Internally Heated Power System (IHPS) and (b) Externally Heated Power System (EHPS)

In order to achieve maximum overall efficiency, the integrated IHPS has to work very close to its operating boundary. This optimal set-point selection, however, puts the system in a very vulnerable position during load[1] transitions. When the load is suddenly increased, the IHPS may not be able to provide sufficient H_2 and heat to sustain the operation under the new load condition. This can lead to temporary H_2 starvation, thereby causing irreversible damage to the FC. To avoid the H_2 starvation, we require that the H_2 produced from the FPS is higher than the hydrogen required for the electrochemical reactions in the FC. Transient issues associated with temporary hydrogen starvation can be avoided by slowing down the change of current drawn from the fuel cell through a rate limiter or a load governor [73]. The power deficit in this case can be provided through hybridization [81], with an additional electrical power source which will increase cost and system complexity. However, in our work we consider the operation at maximum efficiency (optimal H_2 production).

[1]In this work, the term "load" is synonymous to the current drawn from the fuel cell.

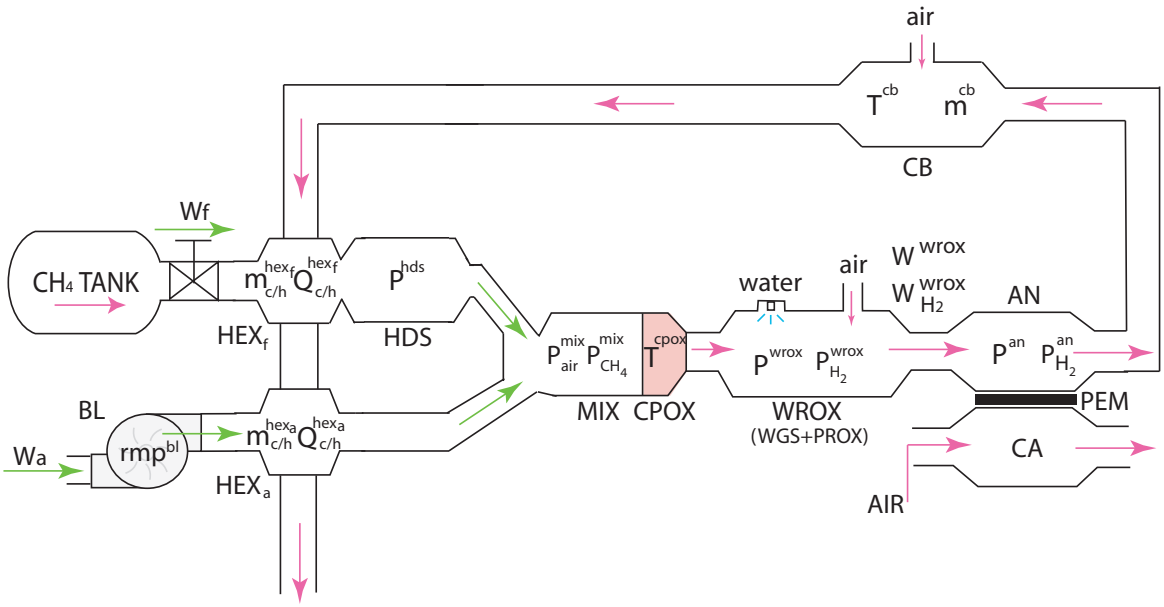

Figure 2.2: IHPS Model State Variables

Operating at optimal steady state and thus capitalizing the benefits of the IHPS will be made possible only if the controlled system responds adequately fast to FC load changes. Otherwise, one has to resort to sub-optimal setpoints, i.e., to trade efficiency for improved safety margin. In this work we design a controller that is aimed at speeding up the natural IHPS dynamics while maintaining optimum reactor temperatures and overall system efficiency. The feedback controller is based on measuring reactor temperatures and estimating the spatially averaged composition of reactant flow through the series of IHPS components.

2.2 Overview of the IHPS Operation and its Dynamic Model

The IHPS investigated in this work, shown in Fig. 2.1a, is composed of five main reactors, namely, the hydro-desulfurizer (HDS), the catalytic partial oxidizer (CPOX), the water gas shift (WGS), the preferential oxidizer (PROX) and the catalytic burner (CB). The first four reactors comprise the FPS. The intended application for the IHPS is the generation of power in a commercial building so natural gas is the targeted fuel. Natural gas contains on average 95% of methane (CH_4), we thus assume that pure methane is supplied to the FPS to be reformed into a rich H_2 flow. A 200kW proton exchange membrane FC (PEM-FC) uses the H_2 in the reformed flow to generate electric power. All FPS and FC components operate at low pressures of up to 130 kPa.

A 19-state nonlinear, control-oriented, dynamic model of the IHPS is developed in order to analyze its behavior [77]. The dynamic states of the model are indicated inside the volumes in Fig. 2.2 while other important variables are also shown such as the mass flow rates W_f, W_a, W^{wrox} and $W^{wrox}_{H_2}$ (see nomenclature definitions). In [60], the initial model

of the fuel processor was developed. The model in [60] assumed constant inlet temperature and did not include the heat exchangers and the catalytic burner.

Some important assumptions about the developed model are that all gases obey the ideal gas law and that each reactor is modeled as a lumped parameter volume with homogenous pressure and temperature. The model is not suitable for start up or shut down simulations because chemical kinetics for the ignition/extinction dynamics have not been modeled. Finally, the model is valid for the range of FC loads between 20 to 80% (i.e., 50-160kW or 70-250A). Within this range of loads the FC stack voltage varies between 0.71V and 0.64V per cell with a total of 1000 cells of 0.04m^2 active area [59].

A brief description of the system operation is given in the following paragraphs with the governing dynamic equations summarized. The calculations for the chemical reactions in the CPOX and more details on the modeling can be found in [77, 59].

The fuel (i.e., methane) flow into the system is defined based on the valve command u_f as

$$W_f = \frac{u_f}{100} W_{nom} \sqrt{\frac{P_{tank} - P^f_{hex_c}}{\Delta P_{nom}}}. \tag{2.1}$$

The main air flow is supplied to the system by a blower (BL) which draws humidified air. The blower speed in revolutions per minute (rpm) is calculated via

$$\frac{drpm^{bl}}{dt} = \frac{1}{\tau_b}\left(\frac{u_a}{100} rpm^{bl}_{ref} - rpm^{bl}\right) \tag{2.2}$$

as a function of the air command u_a. Using the calculated blower speed and the blower map, the air flow is determined. The air and the fuel are pre-heated in separate heat exchangers (HEX). The HDS is used to remove the sulfur from the fuel flow [15, 19]. In this work, only pressure dynamics are considered in the HDS as

$$\frac{dP^{hds}}{dt} = \frac{RT^{hds}}{M_{CH_4} V^{hds}} \left(W^{hex_f} - W^{hds}\right). \tag{2.3}$$

The dynamic states in the HEX include mass and heat:

$$\frac{dm^{hex_{h/c}}}{dt} = \Sigma W^{hex_{h/c}}_{in} - \Sigma W^{hex_{h/c}}_{out}, \tag{2.4}$$

$$\begin{aligned} \frac{dQ^{hex}_{h/c}}{dt} = {} & \Sigma\left(W^{hex_{h/c}}_{in} c_{P_{in}} (T_{in} - T_{ref})\right) - \\ & -\Sigma\left(W^{hex_{h/c}}_{out} c_{P_{out}} (T^{hex_{h/c}}_{out} - T_{ref})\right) \pm UA \cdot (LMTD). \end{aligned} \tag{2.5}$$

Then, the two flows are mixed in the mixer (MIX) where the partial pressure dynamics of

the CH_4 and air:

$$\frac{dP^{mix}_{CH_4}}{dt} = \frac{RT^{mix}}{M_{CH_4}V^{mix}}(W^{hds} - x^{mix}_{CH_4}W^{cpox}), \tag{2.6}$$

$$\frac{dP^{mix}_{air}}{dt} = \frac{RT^{mix}}{M_{air}V^{mix}}(W^{hex_a}_c - x^{mix}_{air}W^{cpox}), \tag{2.7}$$

are taken into account. A static mixing relationship of the two flows is used to calculate the temperature of the MIX flow:

$$T^{mix} = \frac{c_{P_{CH_4}}W^{hds}T^{hds} + c_{P_{air}}W^{hex_a}_c T^{hex_a}_c}{c_{P_{CH_4}}W^{hds} + c_{P_{air}}W^{hex_a}_c}. \tag{2.8}$$

The mixture is then passed through the catalytic partial oxidizer (CPOX) where CH_4 reacts with oxygen to produce H_2. There are two main exothermal chemical reactions taking place in the CPOX: partial oxidation (POX) and total oxidation (TOX) given in [39, 92] with their corresponding energy release per mole of reactant (ΔH^0).

$$(POX) \qquad CH_4 + \tfrac{1}{2}O_2 \rightarrow CO + 2H_2,$$
$$\Delta H^0_{pox} = -0.036\times10^6 \text{ J/mol}, \tag{2.9}$$

$$(TOX) \qquad CH_4 + 2O_2 \rightarrow CO_2 + 2H_2O,$$
$$\Delta H^0_{tox} = -0.8026\times10^6 \text{ J/mol}. \tag{2.10}$$

Hydrogen is produced only by the POX reaction while heat is mostly generated by the TOX reaction. As shown in Fig. 2.3, the distribution between the two is dictated by the reactor temperature T^{cpox}:

$$\begin{aligned}\frac{dT^{cpox}}{dt} = \frac{1}{m^{cpox}c^{cpox}_P}(&W^{cpox}(c^{mix}_P(T^{mix} - T_{ref}) - c^{cpox}_P(T^{cpox} - T_{ref})) + \\ &+N_{CH_4r}\left(S\cdot(-\Delta H^0_{pox}) + (1-S)\cdot(-\Delta H^0_{tox})\right) + \\ &+N_{O_2rH_2CO}\left(\beta\cdot(-\Delta H^0_{hox}) + (1-\beta)\cdot(-\Delta H^0_{cox})\right)),\end{aligned} \tag{2.11}$$

where β is the ratio of the oxygen that reacts with H_2 over the oxygen that reacts with H_2 and CO. The molar flow ratio of oxygen (O_2) in the air to CH_4 in the MIX is defined as:

$$\lambda_{O2C} = \dot{n}_{O_2}/\dot{n}_{CH_4}. \tag{2.12}$$

Moreover, since the CPOX products are also highly dependent on the CPOX reactor temperature T^{cpox}, the optimum balance between the two reactions has to be determined.

Carbon monoxide (CO) is created along with H_2 in the POX reaction, as can be seen in (2.9). Since CO poisons the PEM fuel cell catalyst, it has to be eliminated using water in the water gas shift reactor (WGS) and air in the preferential oxidizer (PROX). The latter

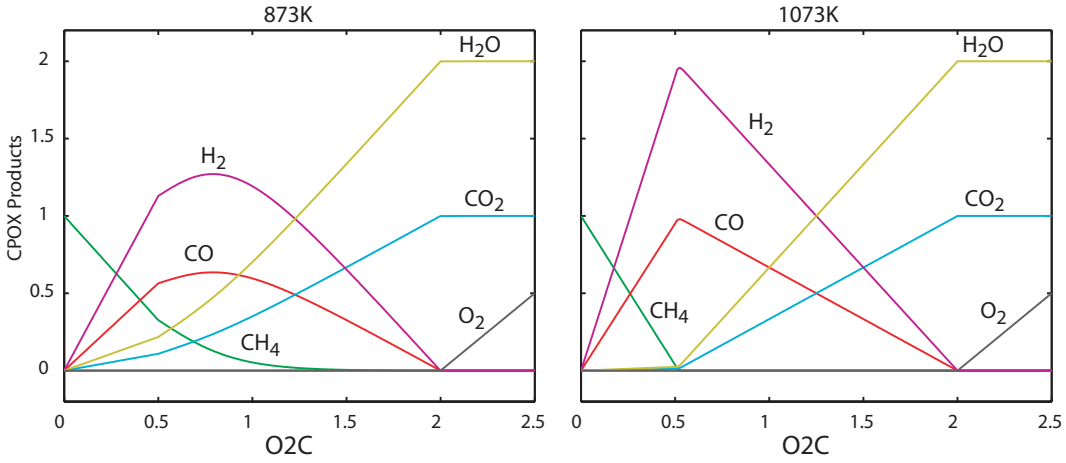

Figure 2.3: CPOX products as a function of λ_{O2C} and reactor temperature

are assumed to operate perfectly thus eliminating all the CO in the stream. In the model the PROX and WGS reactors are merged in one volume called the WROX where the total pressure dynamics and the H_2 partial pressure dynamics are expressed as:

$$\frac{dP^{wrox}}{dt} = \frac{RT^{wrox}}{M^{wrox}V^{wrox}}\left(W^{cpox} - W^{wrox} + W^{wgs}_{H_2O} + W^{prox}_{air}\right), \tag{2.13}$$

$$\frac{dP^{wrox}_{H_2}}{dt} = \frac{RT^{wrox}}{M_{H_2}V^{wrox}}\left((1+\eta^{wrox})W^{cpox}_{H_2} - x^{wrox}_{H_2}W^{wrox}\right). \tag{2.14}$$

Note that it might be necessary to include additional heat exchangers among the WGS, PROX reactors and the FC to achieve the optimum inlet temperature for each reactor. These heat exchangers are neglected here by assuming, for example, that the water sprayed in the WGS offers the appropriate cooling of the flow streams [82].

The H_2-rich mixture leaving the WROX enters the anode of the fuel cell stack where the electro-chemical reaction takes place to convert H_2 to electrical power. The anode model includes the total pressure and the H_2 partial pressure dynamics:

$$\frac{dP^{an}}{dt} = \frac{RT^{an}}{M^{an}V^{an}}\left(W^{wrox} - W^{an} - W^{react}_{H_2}\right), \tag{2.15}$$

$$\frac{dP^{an}_{H_2}}{dt} = \frac{RT^{an}}{M_{H_2}V^{an}}\left(x^{wrox}_{H_2}W^{wrox} - x^{an}_{H_2}W^{an} - W^{react}_{H_2}\right). \tag{2.16}$$

The reacting H_2 is given as a function of the demanded load:

$$W^{react}_{H_2} = M_{H_2}\frac{nI_{st}}{2F} \tag{2.17}$$

and the resulting voltage as a function of H_2 pressure and the demanded load:

$$V = N_{cell}\left(a_1 - a_2\frac{I_{st}}{A_{cell}} - a_3\left(\frac{I_{st}}{A_{cell}P_{H_2}}\right)^2\right). \tag{2.18}$$

The flow from the anode is then supplied to the CB where the excess H_2 is burnt using the air supplied through a blower. The temperature dynamics in the CB are given as:

$$\begin{aligned}\frac{dT^{cb}}{dt} = \frac{1}{m_{bed}^{cb}c_{Pbed}^{cb}} \quad (\quad & W^{an}c_P^{an}(T^{an} - T_{ref}) + \\ + \quad & W^{aircb}c_P^{air}(T^{aircb} - T_{ref}) - W^{cb}c_P^{cb}(T^{cb} - T_{ref}) + Q_r^{cb}),\end{aligned} \tag{2.19}$$

where the heat released from burning the H_2 is a function of the air-to-H_2 stoichiometry in the CB as:

$$Q_r^{cb} = \frac{Q_{LHV}^{H_2}}{M_{H_2}} \cdot min\left\{W_{H_2}^{an}, \frac{W^{aircb}}{34.2}\right\}. \tag{2.20}$$

Finally, the flow from the CB is fed to two separate heat exchangers (HEX - hot side), one to preheat the air and one to preheat the fuel flows before they enter the FPS. The utilization of this heat results in increased overall efficiency of the system. The model without the CB has been verified with a higher-order detailed model [78, 59] while the CB model trends and qualitative response have also been verified [1].

2.3 Literature Review

Publications focusing on the dynamic behavior and load transitions of PEM fuel cell-based CHP systems are fewer than the ones focusing on steady state performance in today's literature. Most work done on CHP systems includes theoretical analysis and prediction of the performance using either thermodynamic or chemistry-kinetic based models, while experimental results are few, especially for integrated systems. In general, CHP systems with solid oxide fuel cells (SOFC) are more common in the current literature. The increased power density and abundance of heat sources make the high temperature SOFC systems more attractive for heat and power coupling for large applications.

Because the FPS and FC technology is mostly experimental based, each publication deals with a slightly different configuration and system set-up. The fuel source used for each configuration varies and is application specific. Given the fuel variations, each configuration has different reactors to allow the reforming of the corresponding fuel. The type of fuel cell used can also vary and the HEX heat sources (CHP combinations) are different. Thus, the main types of FPS-FC systems can be categorizes according to the fuel, reformer type, FC type and CHP configuration used. A list of those types are given in Table 2.1. Note, that not all systems examined in the mentioned articles are CHP, but all include analysis

Types of FPS-FC systems
Based on Reforming Method
Catalytic Partial Oxidation
Steam
Autothermal
Based on Fuel Used
Methane
Methanol
Gasoline
Ethanol
Diesel
Based on FC Used
Proton Exchange Membrane (PEM)
Solid Oxide Fuel Cell (SOFC)
Molten Carbonate Fuel Cell (MCFC)
Alkaline Fuel Cell (AFC)

Table 2.1: Types of FPS Systems

of critical components that are present in a CHP system.

The work done in this dissertation is based on [59], where the initial model of the fuel processor was developed. The model in [59] assumed constant inlet temperature and did not include the heat exchangers and the catalytic burner. A similar dynamics and control study was performed which yields satisfying H_2 production during load transitions by utilizing the CPOX temperature (T^{cpox}) and H_2 partial pressure (y_{h_2}) as feedback variables for the designed control scheme. The CPOX reactor model in [59], is based on [92], where kinetic model simulations are employed along with experimental data to define the products of the CPOX reactor as a function of its temperature and the inlet gas composition.

Before we move on into the system level FPS publications, some important publications on the HDS reactor are given here. Lampert, in [38], gives the description of a desulphurizer that utilizes air and heat to convert sulphur to sulphur oxides which are then adsorbed by a special catalyst. The requirement for a large sized reactor and possible multiple desulphurizers is noted. For gasoline desulphurization, [91] focused on a specific sorbent that is ideal for sulphur removal from gasoline. Sulphur compound removal by partial oxidation is proven significantly powerful but required precise control of the reactor pressure and temperature as shown in [20].

As far as integrated systems and specifically reformer types are concerned, the main categories include catalytic partial oxidation (CPOX), steam reforming (SR) and autothermal reforming (AT). The publications listed here are mainly state state studies of FPS

systems. The articles in [92] and [49] deal with the chemistry involved, composition of the products and reactor temperatures through CPOX reforming. Namely, [49] covers the ideal conditions for minimum catalyst contact time required to oxidize the fuel. A model of a CPOX reactor is developed in [13] based on simplified reactor models and the optimum inlet conditions are examined including optimal inlet temperature, composition and velocity. Experimental results of a SR are given in [41], focusing on the effects of copper catalysts in the process. In [72] different catalysts are considered for SR using experimental procedures and the results are presented focusing on the characteristics of each catalyst. The catalyst performance, the ageing behavior and starting up a SR system is discussed in [85]. For AT reformers, a simulation study focusing in the effects of various parameters, at steady state operation, namely of the reformer operating temperature and the steam to carbon ratio are analyzed in [17]. A thermodynamic model of an AT reformer is presented in [12] focusing on the thermal coupling and load transitions, where the model is also validated using experimental results with respect to the reformer products. The causes of the discrepancies between theoretically calculated and experimentally measured product composition are analyzed as well.

Different kinds of fuels can be utilized in a reformer by using the appropriate reactors. The main fuels used are given in Table. 2.1. Specifically, [54] deals with internal reforming of methane which is feasible in SOFC systems focusing on partial prereforming and anode gas recycling. In [42] an experimental analysis of low temperature methane reforming and the corresponding advantages are presented. J.M. Ogden in [50] focuses on comparing a methanol reformer with a gasoline one in light of cost and efficiency. Ethanol reformers are examined in [11, 29], where the effects of pressure and temperature in H_2 production are examined. For multi fuel reformers, [47] presents an experimental study on a 3 fuel reformer and gives detailed measurements on stand alone or coupled components. On diesel reformers, [53] lists the optimal operating conditions for complete fuel conversion and minimal organic compounds in the exhaust based on an experimental study.

Important publications are given here, in the field of dynamic system analysis of CHP systems, related to the work done in this dissertation. In [26], a similar dynamic model of a CPOX reformer was developed and used as a basis for a reduced-order estimator design in order to predict the flow composition out of the FPS. A similar FPS configuration is studied in [30], where a dynamic model of the system suitable for observer design and start up analysis is presented. Sommer in [64] develops a dynamic model of an AT reformer. Consistent with our conclusions, Sommer points out the effects of volume sizes for the system's transient performance, as well as the benefit of the heat capacity of each volume that acts as a buffer during transients. The need for precise inlet flow control can also be inferred. An explicit dynamic model for direct reforming carbonate fuel cell stack is developed in [44]. Using mainly thermodynamic principles and mass/energy conservation the authors of [44] develop a 10-state model suitable for transient analysis and validate it with a higher-

order model and experimental results. During transient operation temperature overshoot problems are observed.

Continuing on dynamic FPS-FC studies, the authors of [22] develop a model to study the performance on a steam reformer and a PEM FC-based system. Using a simple rate limiter control of the input flows they also note the possibility of overheating the catalyst bed. In [28], a molten carbonate dynamic model is developed and the authors note the coupling between the load following capabilities and the input flow scheduling during a transient as well as the temperature and H_2 production fluctuations. The article given in [88] uses a dynamic model to examine the transient system behavior of a 1 MW FC power plant and reaches the conclusion that feedback control is required to enhance the load following capabilities of the system. Finally, similar studies using dynamic FPS-FC models can also be found in [68, 8, 55, 16, 74]

All dynamic studies of FPS-FC CHP systems mentioned in this literature review concur, explicitly or implicity, to the need of feedback control of the inlet air and fuel flows to the system. Several authors mention also that feedforward scheduling of those flows is inadequate in order for the system to meet the load following requirements.

2.4 Steady State Efficiency Optimization

For the system to work efficiently in an integrated fashion, each component has to be conditioned properly in terms of its operating temperature, humidity, and pressure. This is achieved by controlling the air and fuel intakes of the FPS. The strong physical coupling of the IHPS components will dictate the optimal set-points for the system.

To determine the optimal steady state operating points with respect to the overall system efficiency, the following optimization problem is formulated

$$\max_{(u_f,u_a)} \left(\eta_{IHPS} = \frac{V \cdot I_{st}}{W_f \cdot Q_{LHV}^{CH_4}} \right). \tag{2.21}$$

The objective is to maximize the overall efficiency, η_{IHPS}, which is defined as the ratio of the FC electric power output $V \cdot I_{st}$ over the energy used $W_f \cdot Q_{LHV}^{CH_4}$, where W_f is the amount of fuel used and $Q_{LHV}^{CH_4}$ its lower heating value. The optimization variables are the fuel valve command, u_f, and the air blower command, u_a, both ranging from 0 to 100%, corresponding to fully closed or fully open actuators respectively.

The steepest ascent gradient method is employed to solve the optimization problem [52]. The corresponding iterative algorithm is given as

$$u_{k+1} = a_k \cdot \nabla \eta_{IHPS}^{\mathrm{T}} + u_k \tag{2.22}$$

where a_k is the iteration step, $\nabla\eta_{IHPS}^{\mathrm{T}}(u_k)$ is the gradient vector which corresponds to the η_{IHPS} increasing direction and $u = [u_f \ u_a]^{\mathrm{T}}$. The iteration step size, a_k, is kept constant until no new direction can be found for η_{IHPS} to increase, and a_k is then reduced by the bisection method up to the desired accuracy.

Convergence of the gradient algorithm to a global maximum can be verified given the convex form of the efficiency map for the whole range of FC loads. An example of the efficiency map is given in Fig. 2.4 for the FC load of 100A. The maximum efficiency for this load is 33.6% while the optimal setpoint is $[u_f^* \ u_a^*] = [20.75 \ 29.00]$.

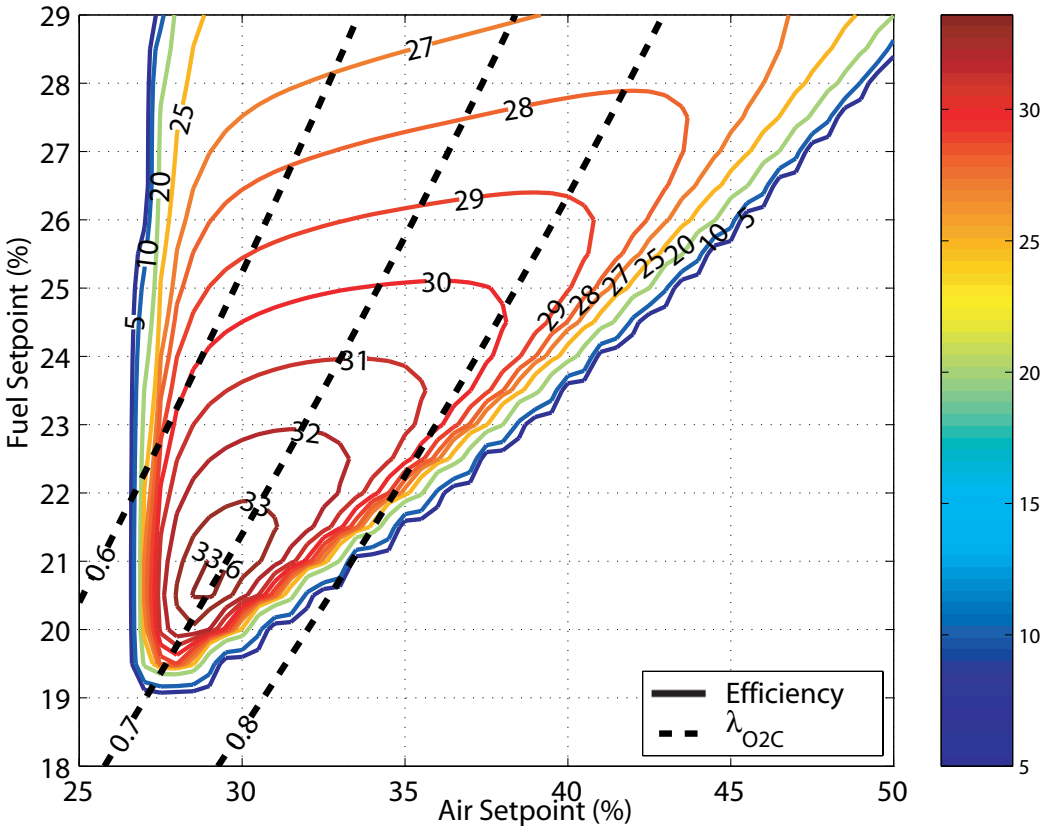

Figure 2.4: Efficiency map of the IHPS at load I_{st}=100A (numbers on the contours indicate corresponding efficiency)

Using the same procedure for each operating load, the optimal steady state setpoint map can be determined for the actuator inputs $u_{I_{st}}^* = [u_f^* \ u_a^*]^{\mathrm{T}}$ and other critical operating variables (ex. $T_{I_{st}}^{cpox*}$) that can serve later as controller setpoints. The optimization results

are shown in Fig. 2.5 and can be approximated by the regression expressions :

$$u_f^* = 7 \cdot 10^{-7} I_{st}^4 - 0.0003 I_{st}^3 + 0.0637 I_{st}^2 - 4.9581 I_{st} + 149.12 \quad (2.23)$$

$$u_a^* = 0.3135 I_{st} - 2.3897 \quad (2.24)$$

$$W_f^* = 5 \cdot 10^{-5} I_{st} - 0.0005 \quad (2.25)$$

$$W_a^* = 0.0003 \cdot I_{st} - 0.0023 \quad (2.26)$$

where W_f and W_a are the corresponding optimal flows in (kg/s) of air and fuel when using u_f^* and u_a^*. Those four curve fits for the optimal setpoints are valid for the range of FC loads between 20% and 80%.

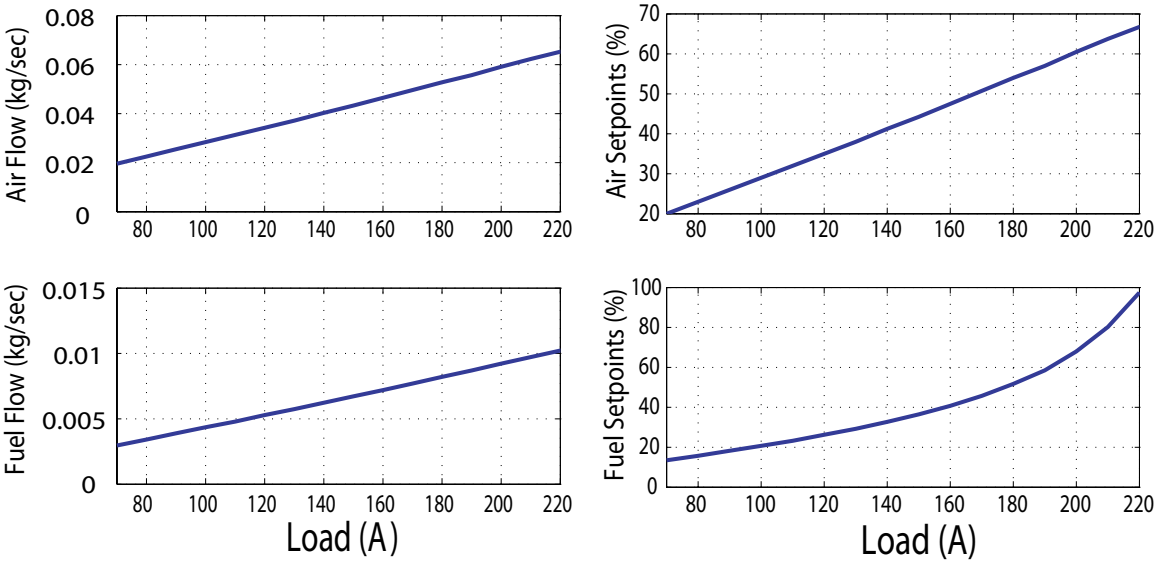

Figure 2.5: Optimal Air and Fuel Flows and Setpoints vs. FC Load

As illustrated in Fig. 2.4, the optimal operating setpoint lies close to the operating boundary of the system, where the operating boundary is defined as the locus of points where $\eta_{IHPS} = 0\%$. Outside this boundary the produced H_2 is less than that required by the FC. This trend is observed for the whole range of operating loads of the system. As a result, the system is susceptible to steady state H_2 starvation when there are uncompensated loads during steady state and transient operation. To avoid modeling errors and to react fast to load variations, a combination of feedforward and feedback control is designed.

It is important to point out that according to the optimization results, all the optimal operating points, independent of the load applied to the FC, occur at $\lambda_{O2C}^* = 0.69$ and $T^{cpox*} = 980$K. Note that the optimization of the overall IHPS efficiency (5.3) leads to a CPOX oxygen to carbon ratio (λ_{O2C}^*) that is greater than the value corresponding to the maximum H_2 production for the CPOX reactor ($\lambda_{O2C} = 0.5$ as indicated in Fig. 2.3).

In order to explain this result, one has to notice that while both POX and TOX reactions

in (2.9)-(2.10) are exothermal, the TOX releases 20 times more heat than the POX reaction. The CPOX temperature, which is highly coupled to the H_2 production in the case of the integrated IHPS, is a function of both the heat released by the reactions inside the CPOX and the temperature of the incoming air and fuel flows. Moving λ_{O2C} towards 0.5 will promote H_2 production but suppress the TOX reaction which only occurs for $\lambda_{O2C} > 0.5$. Thus the contribution of the TOX reaction to the CPOX temperature will be reduced and, as a result, the CPOX reactor has to rely on preheating the inlet flows by the CB. Since both variables (the H_2 and heat) are essential for the system to function properly, the optimal point ($\lambda^*_{O2C} = 0.69$) reflects a balance between the H_2 production in the FPS and heat generation in the CB and the CPOX reactors for steady state operation. Thus, the overall IHPS optimum cannot be defined through optimization of individual components.

Another interesting optimization result is the H_2 utilization (U_{H_2}) in the FC seen in Fig. 2.6 and defined as

$$U_{H_2} = \frac{\text{H}_2 \text{ reacted}}{\text{H}_2 \text{ supplied}} = \frac{W_{H_2}^{react}}{W_{H_2}^{wrox}}, \tag{2.27}$$

where $W_{H_2}^{wrox}$ is the amount of hydrogen supplied to the FC (i.e., exiting the WROX) and $W_{H_2}^{react}$ is the amount of H_2 consumed in the FC at a given load. The need for decreasing the H_2 utilization as load increases is dictated not only by the need for excess H_2 for preheating as load increases, but also by the fuel cell efficiency. At higher loads, excess H_2 promotes the fuel cell efficiency and in turn the overall system efficiency of the IHPS. Indeed, the H_2 utilization in both the IHPS (Fig. 2.1a) and the EHPS (Fig. 2.1b) are found to be equal after dedicated EHPS optimization was performed. Thus, the need for decreasing the utilization at high loads is mostly due to the requirement for high FC efficiency (37% at max load). This is the case for both IHPS and EHPS, independent of the H_2 recirculation loop.

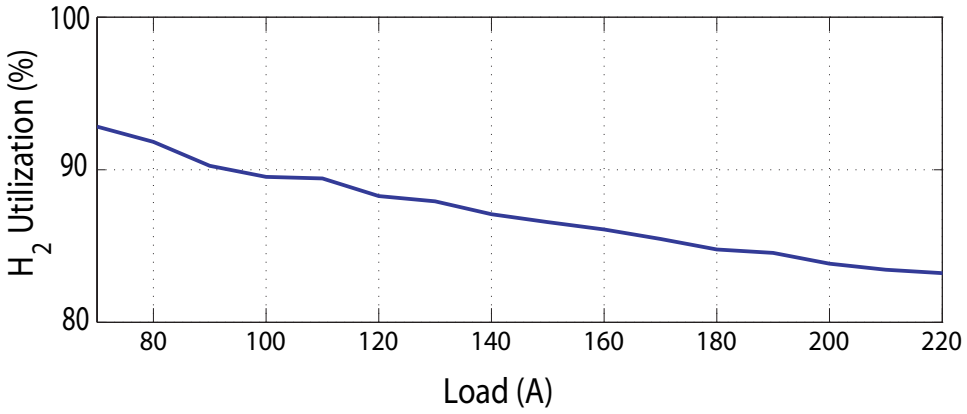

Figure 2.6: H_2 Utilization vs. FC Load

The IHPS will exhibit higher efficiency and lower fuel consumption when compared

against the EHPS as shown in Fig. 2.7. Note that the efficiency shown in Fig. 2.7 is the FPS efficiency defined as

$$\eta_{FPS} = \frac{W_{H_2}^{wrox} \cdot Q_{LHV}^{H_2}}{W_f \cdot Q_{LHV}^{CH_4}}. \tag{2.28}$$

At high loads efficiency increase of up to 12% and fuel consumption decrease of up to 16% can be achieved. Thus the addition of a hydrogen recirculation CB is quite beneficial for such a fuel processing unit.

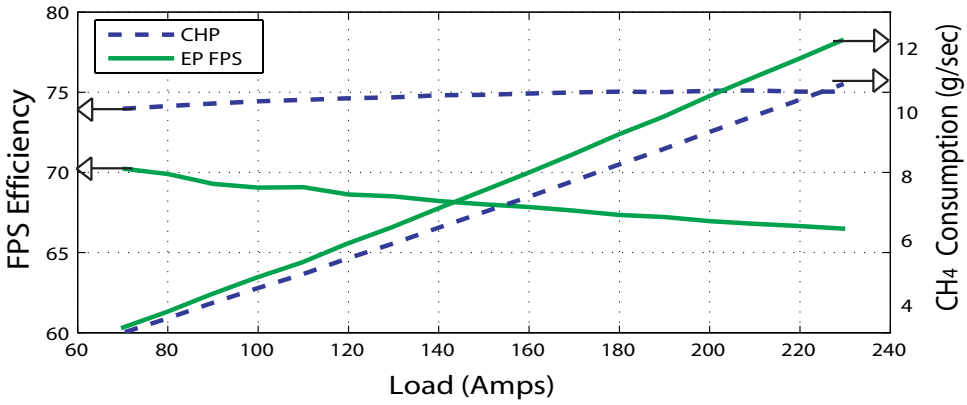

Figure 2.7: Efficiency and fuel consumption of IHPS and EHPS

2.5 Open Loop Dynamic Analysis

Examining the transient performance of the system using static feedforward control enables us to gain insight on the system dynamics. The open loop system dynamics are examined by utilizing the optimal steady state setpoint maps derived from the optimization results, where for a given load, the fuel and air operating setpoint are defined by the feedforward maps (2.23),(2.24).

The open loop response of the system for two consecutive load steps is shown in Fig. 2.8. For the initial small step of 90-100A, the fuel processor provides the fuel cell with the required amount of H_2 in order to meet the load demand. For the second larger step of 100-150A though, the H_2 generation is below the demanded H_2 level for a considerable period of 7 seconds. Starving the fuel cell for 7 seconds can cause power loss and membrane damage while it jeopardizes the life span of the stack [66]. Moreover, a 65 degrees overshoot in the CPOX temperature within 15 sec is observed, which can have damaging consequences for the CPOX reactor. Both issues are highlighted on Fig. 2.8. Since the feedforward maps correspond to maximum efficiency steady state operation, it is not surprising that the open loop control is inadequate in preventing H_2 starvation when a large load step is applied.

In order to identify the root cause of the H_2 starvation and temperature overshoot of the IHPS, we consider three critical processes that affect the generation of H_2 during

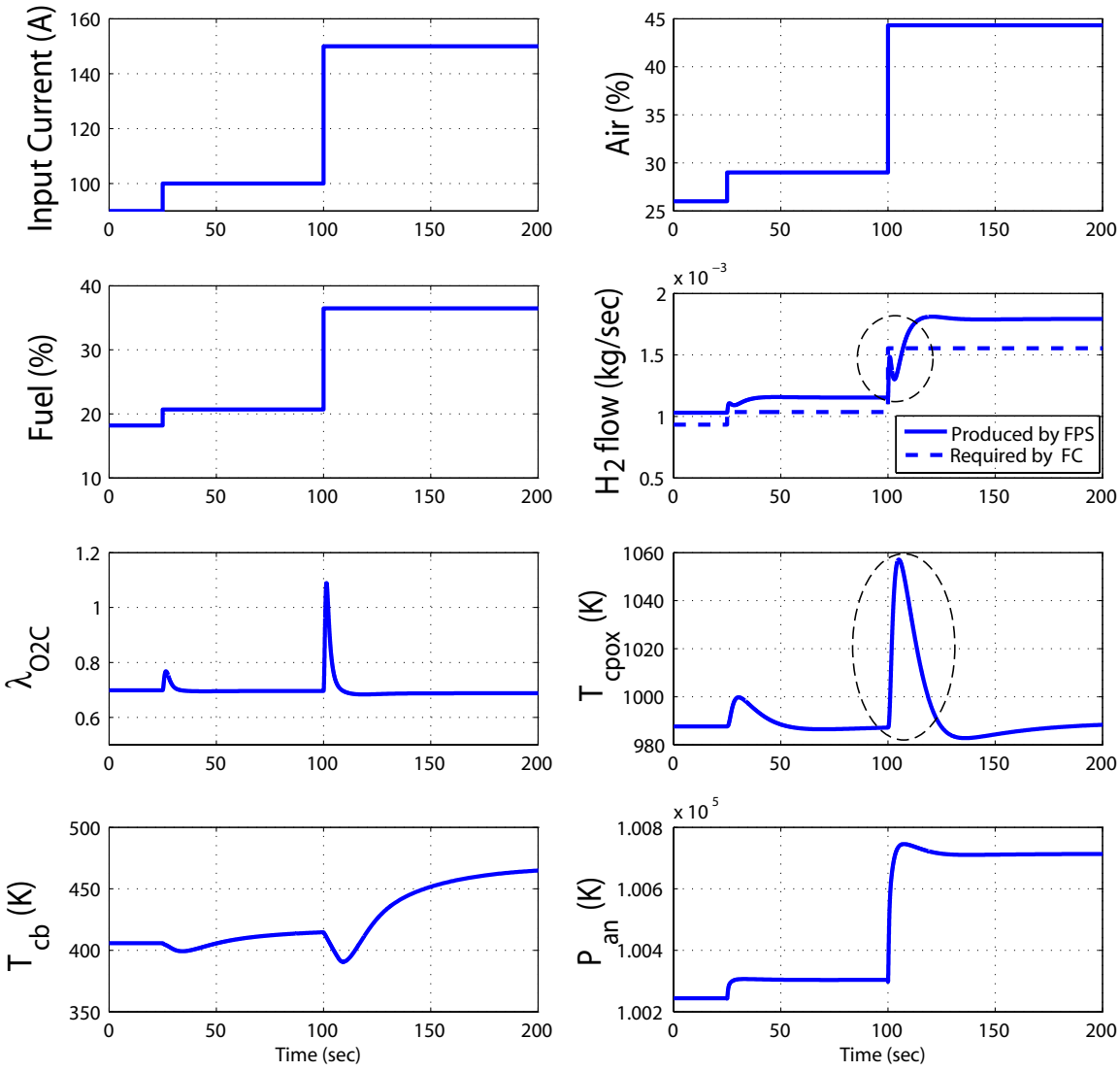

Figure 2.8: Open Loop Performance during 90-100A and 100-150A steps

load changes. Analyzing those processes will provide insight into the control problem and the system design. The first critical process is found to be the CB temperature variation during a step change in load. When a step load is applied, the H_2 flow is depleted at a rate faster than it is produced, due to the slow time constant of the FPS. This results in reduction or even elimination of the H_2 flow to the catalytic burner, which in turn results in a temperature reduction in the CB and eventually a temperature reduction of the inlet air and fuel flows. However, the thermal inertia and relatively large time constant of the CB prevents the temperature from dropping quickly and therefore helps maintain the temperature at a level that does not affect the H_2 production. A comparison of the IHPS, where the CB temperature is a function of the H_2 present in the anode exhaust, with an imaginary system where the CB temperature is maintained constant at a nominal value, is given in Fig. 2.9a and b. The two responses are almost identical, with the constant CB temperature response (Fig. 2.9b) exhibiting slightly less H_2 starvation. Consequently, the CB temperature variation during load increase is not the main cause of the H_2 starvation problem.

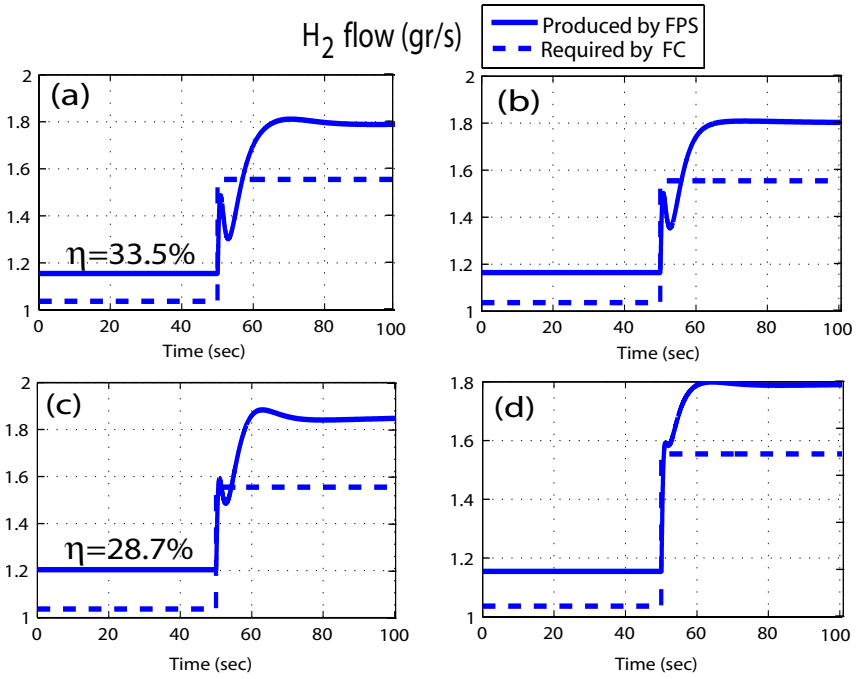

Figure 2.9: Transient performance comparison of (a) original IHPS (b) system with constant preheating temperature (c) system with suboptimal efficiency maps (d) system with HDS volume reduced to 0.1m^3

Furthermore, the feedforward controller, which is based on steady state optimization, places the system close to its operating boundaries and therefore makes it susceptible to H_2 starvation. A suboptimal efficiency map corresponds to the increased excess fuel usage which implies increased H_2 production in steady state. As a result the difference between the required H_2 and the produced is increased leading to increased safety margins at the

price of reduced efficiency. In the case of a suboptimal efficiency setpoint, shown in Fig. 2.9c, there is an efficiency reduction from 33.5% to 28.7% and the severity of the H_2 starvation is reduced substantially.

The third and most important cause of the H_2 starvation can be attributed to reactor sizing issues. The large residence time of the HDS, due to the slow kinetics of the fuel desulphurization [75], imposes the requirement of a relatively large volume compared to the adjacent volumes of the MIX and the HEX. The combination of the large volume in the fuel path, the small volume of the air path and the large flow of air compared to the fuel flow causes the MIX pressure to build up at a rate faster than the HDS pressure during transients. In turn the pressure difference between these volumes initially exhibits an undershoot until the HDS pressure manages to build up again as illustrated in Fig. 2.10. Since flow is a function of the pressure difference ($P_{hds} - P_{mix}$), the same undershoot is observed for the fuel flow (W_f) which causes the oxygen-to-carbon ratio, λ_{O2C}, to overshoot.

Based on the CPOX reaction map, given in Fig. 2.3, an overshoot in λ_{O2C} from its nominal steady state operating point of 0.69 to 1.15, implies a steep decrease in H_2 production. One way to avoid this is by decreasing the HDS volume in the model. The responses of the original system, with $V^{hds} = 0.3$ m^3 [58], and of an imaginary system that has a considerably smaller HDS volume of 0.1 m^3 are given in Figures 2.9a and 2.9d respectively. For the latter case, the H_2 starvation problem is significantly mitigated. If future advances in the desulphurization process produce more compact HDS reactors, then the transient performance of the system would improve. Note that recent advances in desulphurization technology allow the use of multiple smaller HDS reactors [9, 65] which would require precise switching control.

A straight forward solution to the transient problems is to apply an air rate limiter since the air flow chokes the fuel flow during transients. Such a configuration is seen in Fig. 2.11. A rate limiter to restrict the current drawn from the fuel cell is also required since the air rate limiter alone does not eliminate the H_2 starvation problem due to the system dynamics. For a load step of 100 to 150A a 2 %/sec rate limiter and a 10A/sec rate limiter for the air command and the current demand, respectively, are required.

Given the nonlinear dynamics of the plant, a constant rate limiter is not suitable for all load transitions. If this solution is pursed, a more elaborate load governor would be required as presented in [73] or a scheduled filter rate as in [69]. However, limiting the rate of load change would slow down the system response and lead to deteriorated load following performance. Rate limiters or load governors are add-on mechanisms that are applied to systems whose control capabilities have otherwise been fully explored.

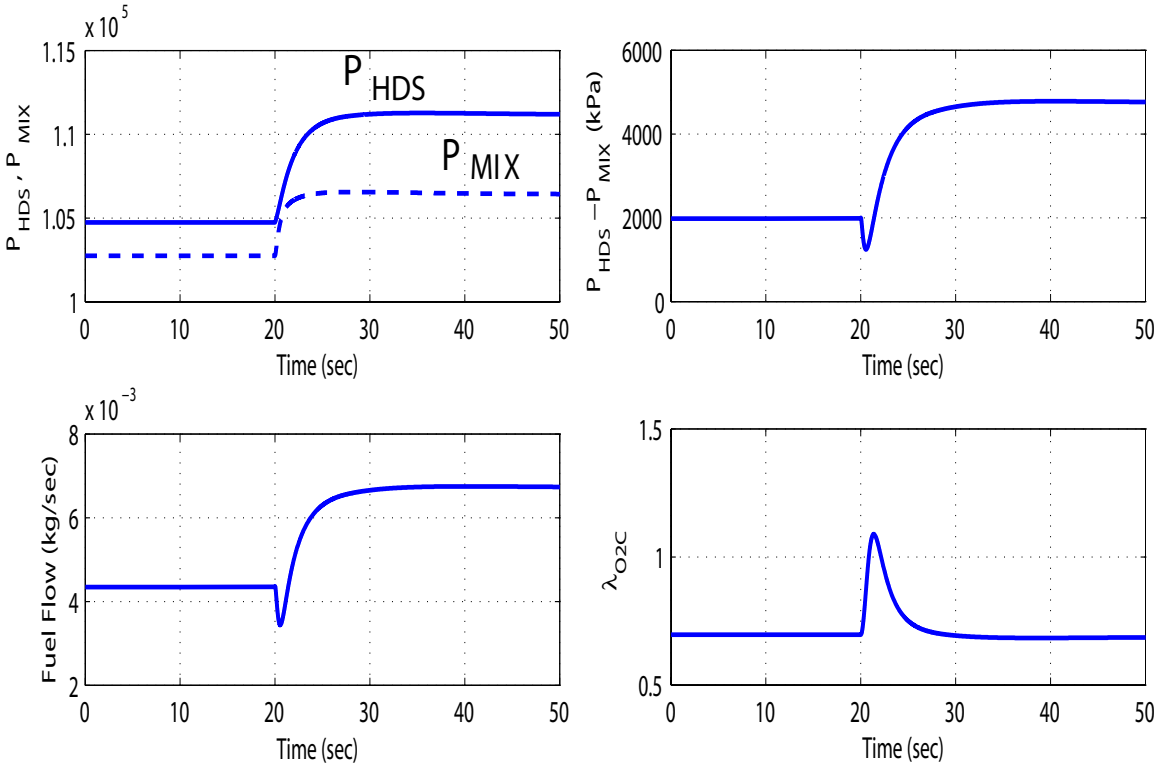

Figure 2.10: λ_{O2C} overshoot during open loop operation

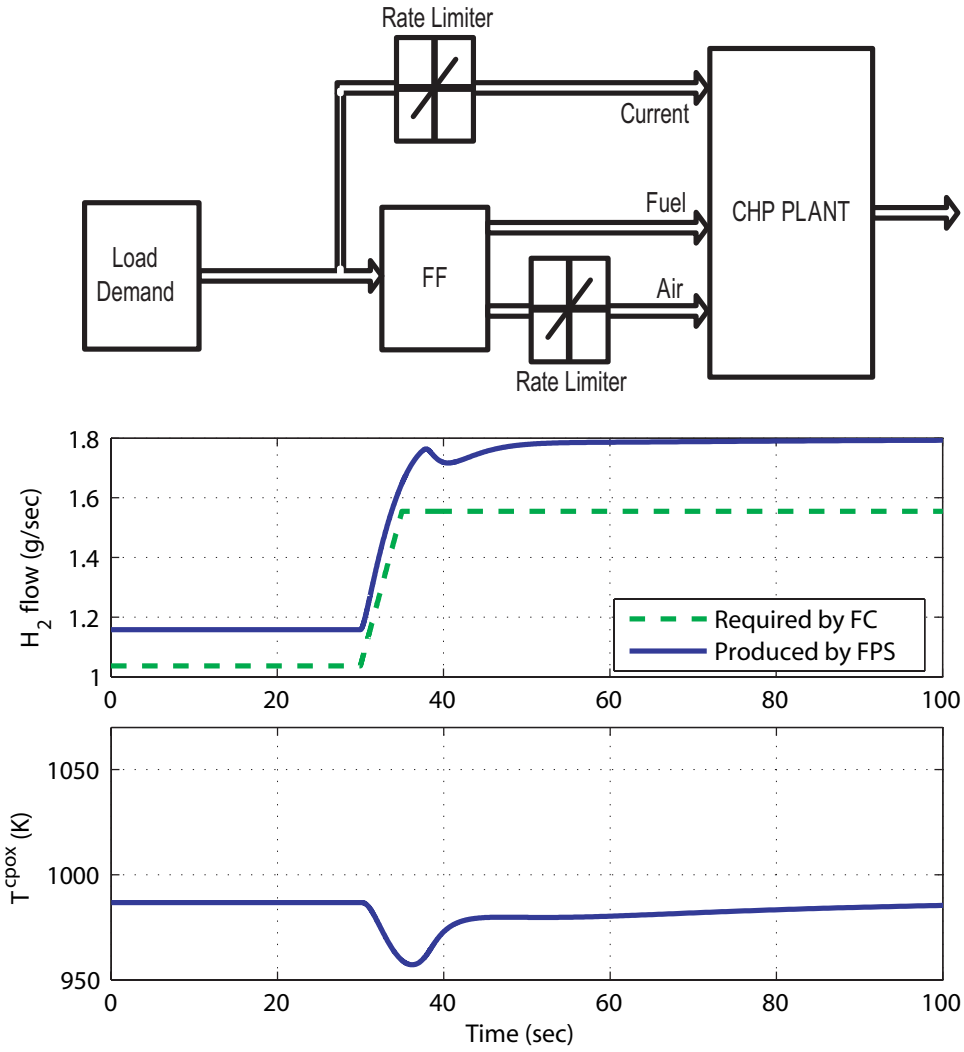

Figure 2.11: System configuration and response with air rate limiter

CHAPTER 3

Model-Based Control and Closed Loop Robustness of a Fuel Processor with Exhaust Heat Recirculation

3.1 Introduction

In this chapter we investigate the effectiveness of using observer-based feedback control to improve the transient performance of the IHPS. In particular, our objective is to reduce the H_2 starvation problem and to control the CPOX temperature overshoot while maintaining efficient steady state operation by utilizing the optimized feedforward maps. Furthermore, the robustness of the designed controller is evaluated under various uncertainty scenarios. It is shown, via model-based analysis, that the closed loop performance does not deteriorate significantly under the examined scenarios.

The control architecture presented here is based on setpoint error regulation, using the optimal setpoint maps defined in Sec. 2.4 through the plant optimization. The controller is implemented by augmenting integrators to the estimator-based feedback controller. In deciding which signals need to be regulated and are best suited as feedback variables in the controller, one has to consider the control requirements (namely, anode H_2 partial pressure and T^{cpox} regulation), the sensitivity of measured signals to the fuel and air actuators, as well as the ease of measuring those signals. Ideally we would choose the CPOX temperature T^{cpox} and the partial pressure of H_2 leaving the anode as the feedback variables, as they are linked directly to the control objectives [59]. Unfortunately, hydrogen partial pressure P_{H_2} is difficult to measure, while estimating it requires elaborate modeling of the fuel cell polarization characteristics [59, 25]. We thus choose the CB temperature T^{cb} instead. The CB temperature T^{cb} is closely coupled to the H_2 starvation problem. During transient operation, reduction of T^{cb} from its optimal steady state value T^{cb*} implies reduction of the H_2 leaving the anode exhaust and in turn, H_2 starvation. The only drawback of using T^{cb} instead of P_{H_2} is the slow dynamics due to the associated thermal inertia. As we show later, this drawback can be eliminated by a model-based closed loop estimator that compensates

for the slow T^{cb} dynamics.

3.2 Feedback Control Design and Analysis

The IHPS model developed can be expressed as a function of the states x, the inputs u and the disturbance w as

$$\dot{x} = f(x, u, w). \tag{3.1}$$

with the linear approximation of the IHPS plant being

$$\delta\dot{x} = A_p \cdot \delta x + B_p \cdot \delta u + B_w \cdot \delta w \tag{3.2}$$

$$\delta z = C_z \cdot \delta x \tag{3.3}$$

where $\delta(\cdot) = (\cdot) - (\cdot)_o$ and $(\cdot)_o$ refers to the linearization setpoint. The model has 19 states (Fig. 2.2) and two inputs, namely the fuel and air command. The current is treated as a measured disturbance to the system. The performance variables considered are the CPOX and CB temperatures.

$$u = [u_f \ u_a]^{\mathrm{T}} \ , \ w = I_{st} \ , \ z = [T^{cpox} \ T^{cb}]^{\mathrm{T}}. \tag{3.4}$$

The medium load of 100A is chosen as the linearization point. At that load, the optimization yielded steady state fuel and air input commands of 20.75% and 29%, respectively.

By looking at the eigenvalues of the linearized IHPS plant, there is a large difference between the smallest (-0.024786) and the largest one (-7062.4), indicating a very stiff system ($cond(A_p) = 8.4313 \cdot 10^{15}$) with potential difficulties in tuning and assuring performance robustness. In addition the normalized condition number of the observability gramian is very large:

$$o_N = \frac{cond[Q_{obs,\{C=Cz\}}]}{cond[Q_{obs,\{C=I_{19\times 19}\}}]} = 2.5 \cdot 10^{11}, \tag{3.5}$$

where $cond$, Q_{obs} indicate the condition number and the observability gramian, respectively.

A balanced realization [18] (pp.372-376) shows that only 5 states are needed to describe the dynamics of the chosen performance variables. This plant will be referred to as the

bt-plant and can be expressed as:

$$\delta \dot{x}_{bt} = A_{bt} \cdot \delta x_{bt} + B_{bt} \cdot \delta u + B_{wbt} \cdot \delta w \tag{3.6}$$

$$\delta z = C_{bt} \delta x_{bt} \tag{3.7}$$

where $\delta x_{bt} = T\delta x$. Analyzing the balanced transformation matrix T we conclude that the important original states are P^{hds}, T^{cb}, T^{cpox}, $P^{wrox}_{H_2}$ and $m_c^{hex_f}$. This is inferred by examining the rows that correspond to relatively large Hankel singular values in the five row transformation matrix T. As expected, since we want to monitor the static and dynamic behavior of T^{cpox} and T^{cb}, the balanced states in turn depend on T^{cpox} and T^{cb} as well. Moreover, the transient behavior of H_2 production and thus T^{cpox} and T^{cb} is highly coupled with P^{hds} due to the transient effects analyzed earlier in Sec 2.5. Finally, the fact that $P^{wrox}_{H_2}$ is important can be attributed to its correlation to the H_2 production from the FPS and in turn to the T^{cpox}.

Checking the condition number of the observability gramian of the bt-plant we have

$$cond[Q^{bt}_{obs,\{C=C_{bt}\}}] = 34.3. \tag{3.8}$$

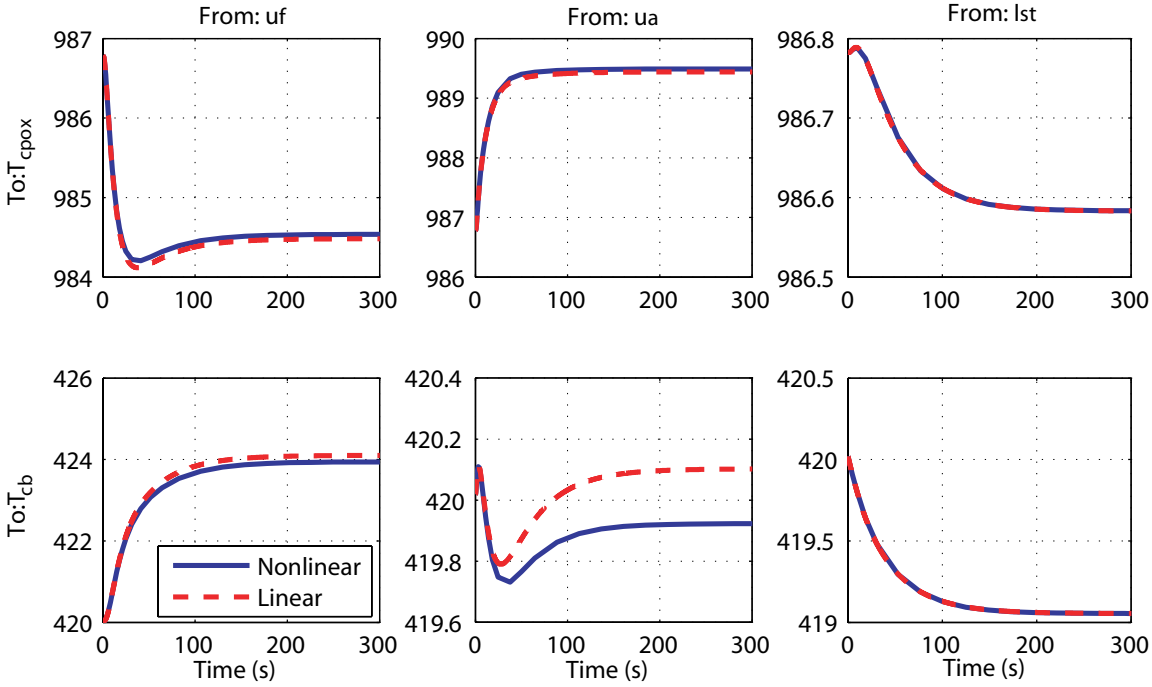

Figure 3.1: Nonlinear and bt-plant response to individual 0.1% steps in (u_a, u_f, I_{st}) from (29, 20.75, 100) to (29.29, 20.96, 101)

The step responses of the linear bt-plant and the nonlinear full order plant are shown in Fig. 3.1. It is interesting to note that even though the DC-gain of the u_a-to-T^{cb} linear trans-

fer function is zero, the transient dynamics are captured while for the rest, the responses of the bt and nonlinear plants are similar. Thus, as far as T^{cpox} and T^{cb} are concerned we can conclude that no dynamic (transient) or static (DC-gain) information is lost by the truncation of the original plant.

3.2.1 Controller Design

A first approach to the controller design is the derivation of full state feedback control which is designed using the LQR technique. The estimator design follows next. The estimator is based on the bt-plant (3.6, 3.7) and is expressed as

$$\delta\dot{\hat{x}}_{bt} = (A_{bt} - L \cdot C_{bt}) \cdot \delta\hat{x}_{bt} + [L \; B_{bt} \; B_{wbt}] \cdot \begin{bmatrix} \delta z \\ \delta u \\ \delta w \end{bmatrix} \tag{3.9}$$

where the estimator gain is defined as

$$L = SC_{bt}^{\mathrm{T}} R_L^{-1} \tag{3.10}$$

and S is the solution to

$$A_{bt}S + SA_{bt}^{\mathrm{T}} - SC_{bt}^{\mathrm{T}} R_L^{-1} C_{bt} S + Q_L = 0. \tag{3.11}$$

with process noise covariance Q_L and the measurement noise covariance R_L:

$$Q_L = I_{(m\times m)} + 100 \cdot B_{bt} B_{bt}^{\mathrm{T}} \;,\; R_L = 100 \cdot I_{(2\times 2)}. \tag{3.12}$$

The estimator-based linear control law is

$$u - u_w = -K_p \cdot (\hat{x}_{bt} - x_{bt_w}) - K_I \cdot q \tag{3.13}$$

where $\hat{x}_{bt} = \delta\hat{x}_{bt} - x_{bt_o}$. So (3.13) becomes

$$u = u_w - K_p \cdot (\delta\hat{x}_{bt} + T(x_o - x_w)) - K_I \cdot q \tag{3.14}$$

where T is the 5×19 transformation matrix and $x_w,\; u_w$ satisfy the steady state condition of (3.1) as

$$f(x_w, u_w, w) = 0 \tag{3.15}$$

with u_w being the optimal steady state operating setpoint as defined by the optimization. Note that when implementing the linear control law to the nonlinear IHPS plant, the $(\cdot)_w$ terms are given by a feedforward map as a function of the load. At the linearization load of 100A, $x_o = x_{w_{|w=100}}$ and $x_{bto} = Tx_o$. Using (3.14) has several advantages over using constant setpoints. Since at steady state both $u - u_w$ and $x - x_w$ go to zero, q has to go to zero as well. Thus, even if the feedforward u_w and x_w maps are not perfect, it will take a longer time for the integrators to become saturated. Compared to $u - u_o$ and $x - x_o$, another advantage is the initial step at the time of the load step that comes through the feedforward maps, which helps speed up the transient performance of the system.

Furthermore, in (3.14), q are the integrator states of T^{cpox} and T^{cb} defined as

$$\delta\dot{q} = z - z^* = \left[(T^{cpox} - T^{cpox^*})\ (T^{cb} - T^{cb^*})\right]^{\mathrm{T}} \tag{3.16}$$

where T^{cpox^*} and T^{cb^*} are the desired steady state points as obtained in Sec. 2.4. The control gain for the augmented bt-plant (i.e., the bt-plant augmented with the two integrators) is

$$[K_p\ K_I] = R_K^{-1} B_{aug}^{\mathrm{T}} P \tag{3.17}$$

and P is the solution to the Riccati equation

$$PA_{aug} + A_{aug}^{\mathrm{T}} P - PB_{aug} R_K^{-1} B_{aug}^{\mathrm{T}} P + C_{aug}^{\mathrm{T}} Q_K C_{aug} = 0. \tag{3.18}$$

The weighting matrices Q_K and R_K used for the controller inputs and the outputs, respectively, are

$$Q_K = diag([1\ 0.5\ 1\ 0.1])\ ,\ R_K = diag([10\ 10]). \tag{3.19}$$

The tuning matrices for the design of K_p and K_I are chosen in order to achieve the desirable overshoot of the fuel and slowdown of the air command. Given the fuel actuator saturation constraints (if applicable) the gains can be tuned accordingly. The tuning gains for the design of L are chosen in order to achieve the desired matching between the full state feedback and the estimator-based controllers responses.

Finally, a schematic of the application of the estimator-based controller to the nonlinear model is given in Fig.3.2.

3.2.2 Performance Evaluation of the closed loop system

The feedback controller manages to improve the transient performance of the IHPS as shown in Fig. 3.3. It overshoots the fuel and slows down the air command initially, in order

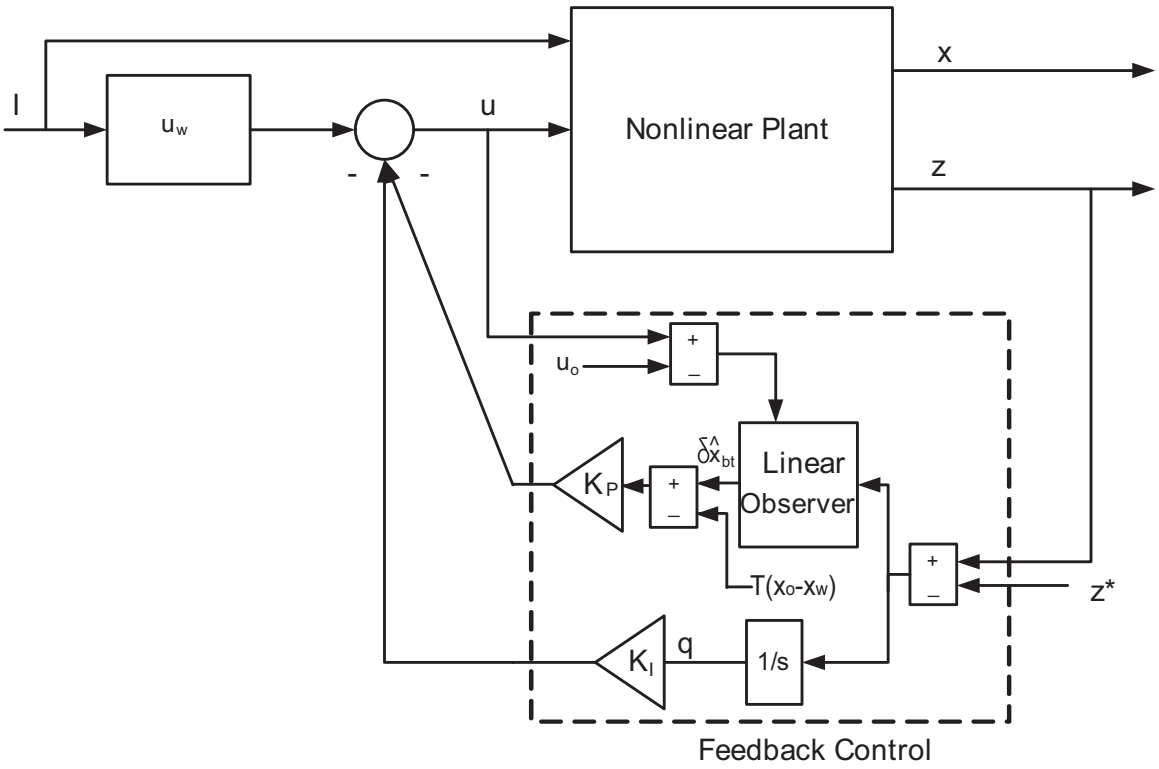

Figure 3.2: Estimator-based controller applied to nonlinear plant

to regulate λ_{O2C} around its optimal value and reduce the undershoot of fuel flow that is observed during open loop operation. As a result, the H_2 production increases smoothly and the H_2 starvation problem is reduced.

Furthermore, the CPOX reactor temperature overshoot is substantially reduced. Application of the observer-based feedback controller yields a small overshoot which is negligible compared to the open loop performance where T^{cpox} overshoots to 1060 K within 15 sec.

It is important to note that the performance achieved with the proposed controller, that utilizes only temperature measurements, is comparable to the performance of the controller developed in [57] for the FPS-FC system, that utilizes T^{cpox} and $y_{H_2} = P^{an}_{H_2}/P^{an}$ (i.e., H_2 partial pressure sensor). The latter measurement is significantly faster than T^{cb}, since it involves pressure dynamics instead of temperature but is only available for experimental investigations. Thus, implementing a CB into an FPS, besides increasing significantly the steady state efficiency, also provides an indirect measurement of the H_2 starvation that is easy to measure and can be utilized to control the transient response.

Finally, as shown in Fig. 3.3, even though the H_2 starvation problem is substantially alleviated compared to the open loop case, there is still a short period of hydrogen starvation of about 0.9 sec. Obviously, the H_2 production, due to the system dynamics (mainly due to the volumes involved), cannot follow the desired step response. Thus, a load rate limiter is still required to eliminate H_2 starvation.

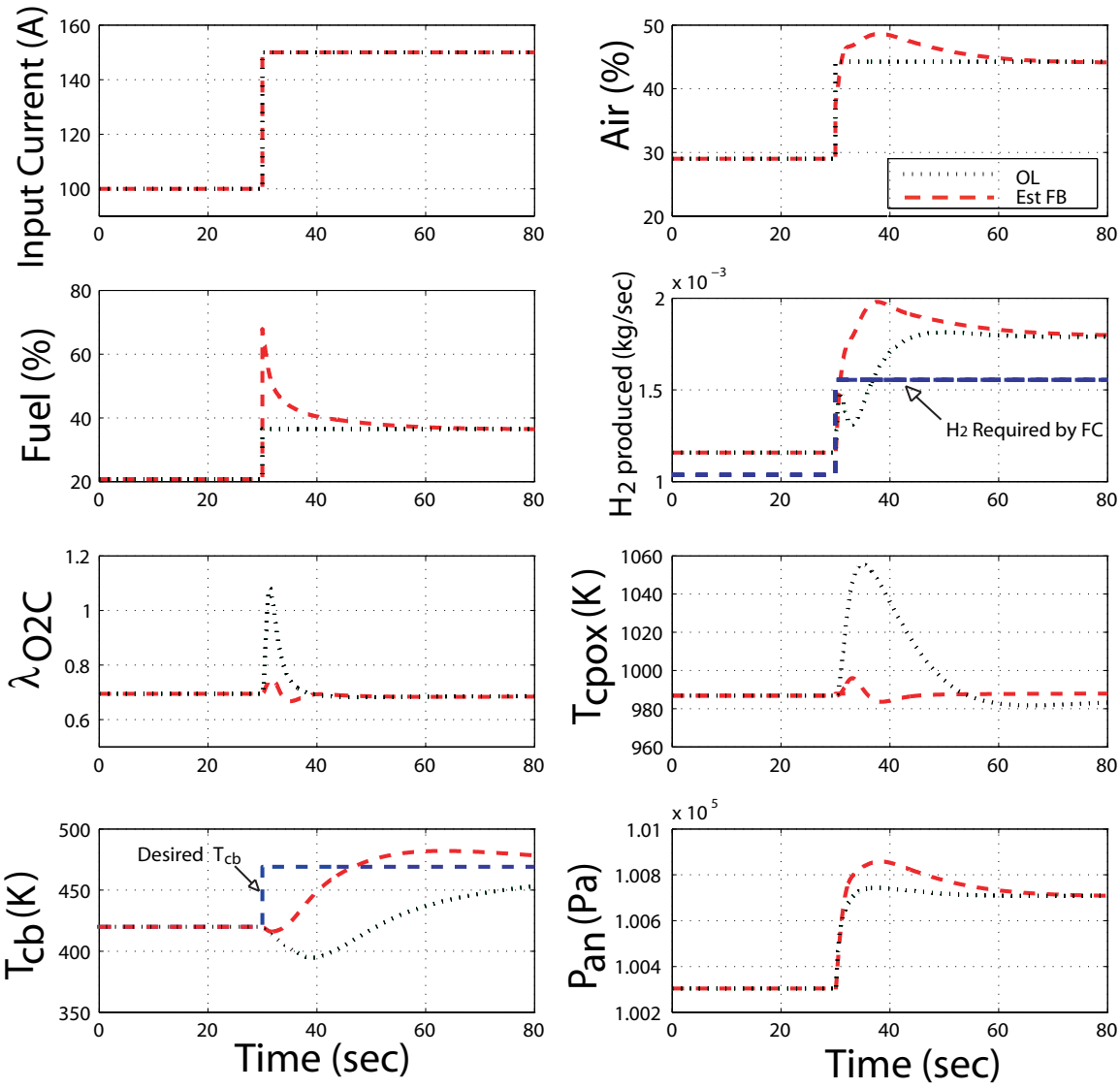

Figure 3.3: Comparison of Estimator FB, Open Loop (OL) and State FB Performance

In combination with the designed estimator feedback controller, a very fast rate limiter of 40 A/sec is adequate to mitigate the H_2 starvation problem completely compared a 10 A/sec limiter required for the open loop case. Thus, with feedback control, the maximum allowable speed for load application is increased by a factor of 4.

3.3 Closed Loop Robustness Evaluation

3.3.1 Robustness Against CPOX Clogging

A well-known problem for CPOX systems is clogging due to carbon build up and deformation caused by the aging process and occasional excess temperature. Risk of CPOX clogging due to carbon formation is increased when reforming diesel or gasoline fuels, because of their heavy carbon concentration, but is still an issue when reforming natural gas. Deformation of the CPOX catalyst can easily occur if the CPOX temperature exceeds the meltdown temperature of the catalyst or backbone material (1000-1100 K), which can be caused by large λ_{O2C} values [2]. Note that catalyst deactivation effects due to carbon formation are not considered in this work, which may compound to the adverse effects of CPOX clogging.

Clogging of the CPOX reactor leads to increased CPOX pressure drop that can be emulated in our numerical simulation model by a reduction in the CPOX outlet effective orifice area. Given the low operating pressure of the system examined in this work, even small increase in the CPOX reactor pressure drop can affect the reactant flows and hence the hydrogen produced by the FR. Figure 3.4 shows the effect of CPOX clogging to the FF controlled FCFR system. Even at 10% CPOX clogging the amount of hydrogen produced by the reformer is less than the amount required by the fuel cell, leading to prolonged hydrogen starvation. Furthermore, there is a significant increase in the CPOX temperature overshoot caused by the increased λ_{O2C} overshoot. CPOX temperature overshoot increases from 68 K (0% CPOX clogging) to 87K (20% CPOX clogging). Even though both fuel and air flows are clogged equally with the CPOX clogging, the fuel choking problem due to the HDS observed in the nominal plant (0% CPOX clogging) is amplified. This can be attributed to the increase in the CPOX and MIX pressure from 104.73 kPa to 105.81 kPa, which in turn causes increased resistance in the incoming fuel flow. Finally, the CB temperature is reduced dramatically due to the prolonged anode hydrogen starvation (i.e., no hydrogen entering the CB).

Figure 3.5 shows the response of the FCFR system when combined FF and FB control are applied. Mainly due to the integral action of the control scheme, the steady state values of CPOX temperature and hydrogen production are regulated to the desired value (the same value as for 0% CPOX clogging) for all levels of CPOX clogging. The transient response of CPOX temperature deteriorates significantly, when compared to the nominal FB response,

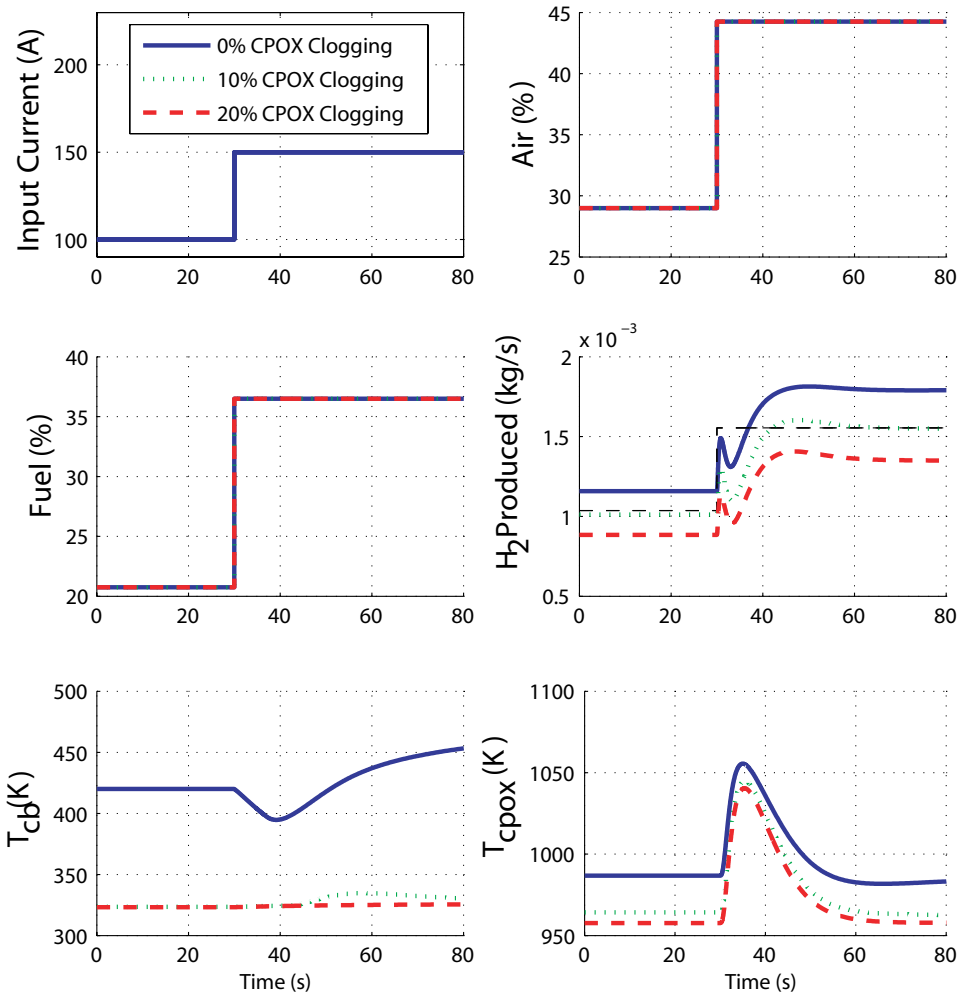

Figure 3.4: System Response with FF control for various CPOX Clogging

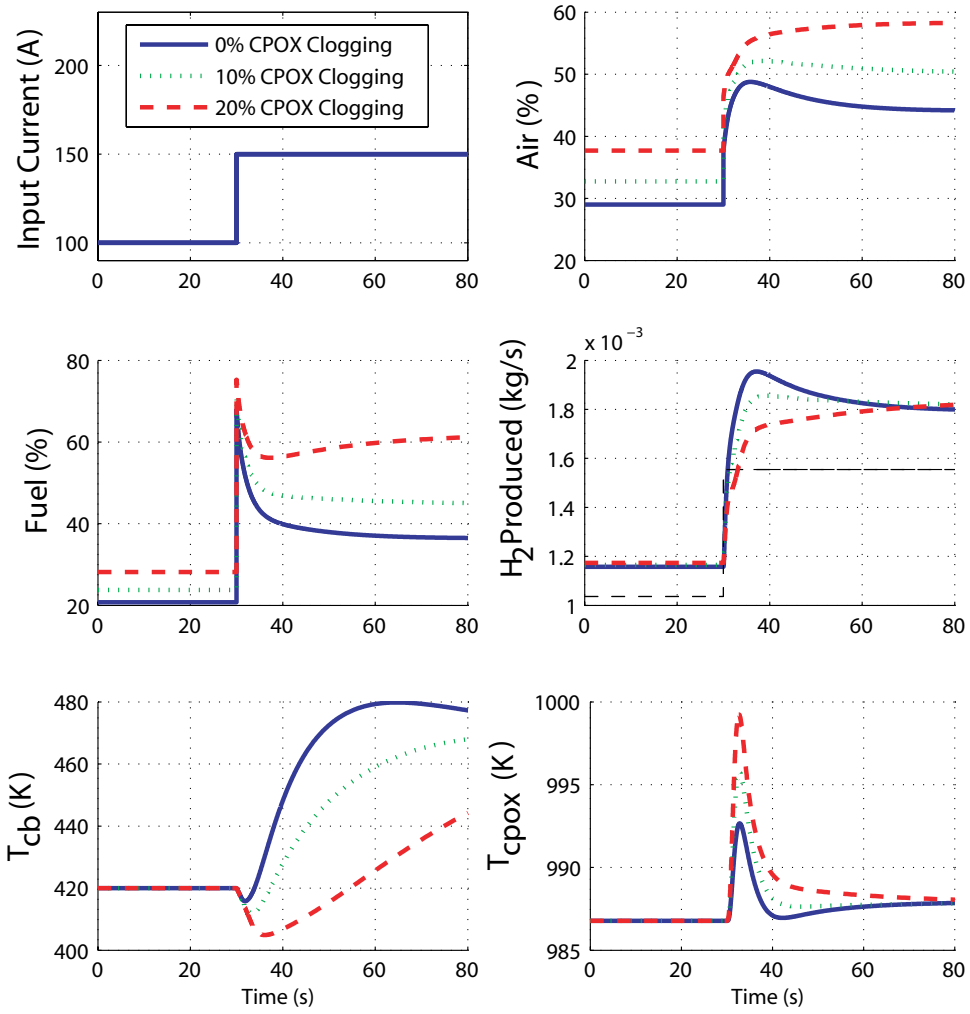

Figure 3.5: System Response with FF-FB control for various CPOX Clogging

Orifice Reduction	Closed Loop		Open Loop	
(%)	SP (sec)	T_{max}^{cpox} (K)	SP	T_{max}^{cpox} (K)
0	0.9325	995.99	6.8749	1055.6
6	1.1095	998.38	9.5279	1047.5
12	1.5359	1001.2	Inf	1044
18	3.4581	1004.5	Inf	1041.4
24	4.4326	1008.4	Inf	1038.5
30	6.1035	1013.2	Inf	1035.3

Table 3.1: H_2 Starvation Period (SP) and ST_{max}^{cpox} for different CPOX outlet orfice reduction during a 100-150A step

but is kept under 1000 K. The starvation period (SP)[1] is also kept within satisfactory limits and degrades from 0.9sec (0% CPOX clogging), to 3.6sec (20% CPOX clogging).

The FF-FB control scheme mitigates the effects of CPOX clogging during steady state by shifting the air and fuel operating setpoints in order to achieve the desired CPOX temperature and hydrogen production. During transient operation, the controller increases the overshoot of fuel and slows down air in order to mitigate the increase in CPOX temperature overshoot.

3.3.2 Robustness Against HDS Clogging

In the open loop analysis of the system, the HDS volume in the fuel flow path upstream of the mixer was identified as the main cause of the poor load following performance of the system [77]. Due to the relatively large volume of the HDS and smaller fuel flow rate (kg/s) compared to that of air, the fuel was restricted from entering the MIX during load transitions, therefore causing hydrogen production delay. In this section the system performance is evaluated under different levels of HDS clogging.

Utilizing only the feedforward map, the open loop system response is shown in Figure 3.6 for 0%, 10% and 20% HDS clogging. It can be seen that the system cannot operate open loop with 10% or more HDS clogging, since the steady state hydrogen production is less than the demanded amount by the fuel cell. Furthermore, the high CPOX temperature caused by the HDS clogging would cause melt down of the CPOX reactor.

Contrary to the CPOX clogging case where both air and fuel flows are affected, only the fuel flow is restricted with the HDS clogging. The resulting response though is similar due to the increase in the MIX pressure from 104.73 kPa to 104.97 kPa. Note that in the CPOX clogging case the pressure increase is larger given that the flow out of the CPOX is the sum of the air and fuel flows entering. That explains why at 20% CPOX clogging, the FF-

[1]SP is defined as the period during a load transition where the demanded amount of hydrogen is higher than the amount of hydrogen produced.

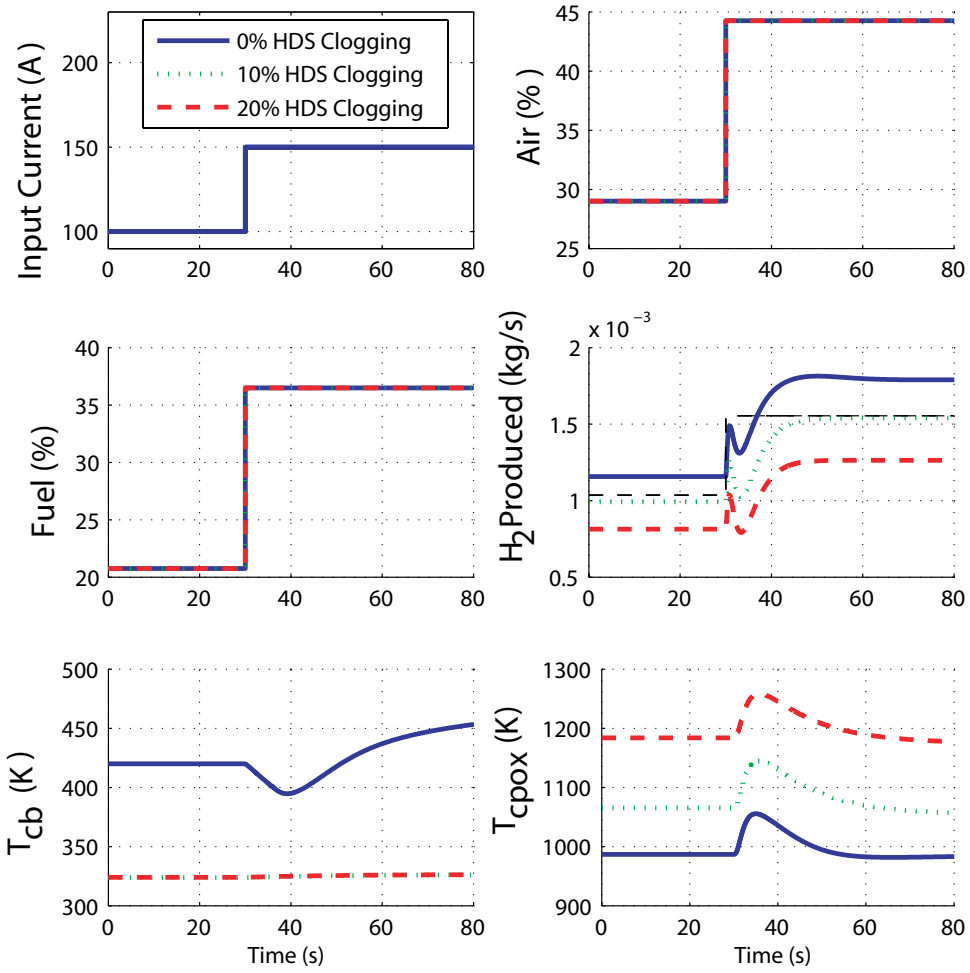

Figure 3.6: System Response with FF control for various HDS Clogging

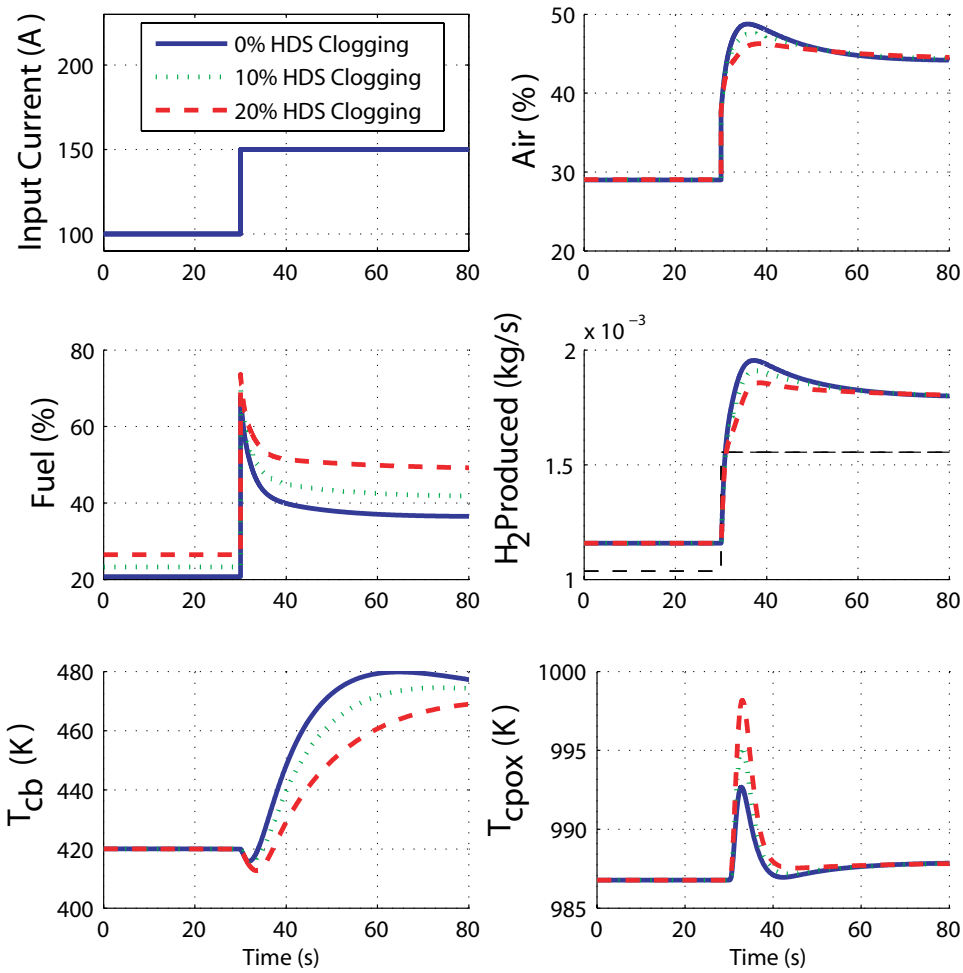

Figure 3.7: System Response with FF-FB control for various HDS Clogging

FB system performance exhibits increased deterioration compared to 20% HDS clogging. Again, there is a significant increase in the FF CPOX temperature overshoot, which is a result of the increased λ_{O2C} overshoot (i.e., increased fuel choking). At 20% HDS clogging the CPOX temperature overshoot is 78 K while for the nominal plant it is 68 K.

When the FF-FB controller is applied, the system exhibits satisfactory performance both in steady state operation and during the transient. The steady state performance is achieved by increasing the fuel command as the HDS clogging gets worse, while the air command at steady state remains unchanged. The transient performance is restored by increasing the overshoot in the fuel and slowing down the air command, thus overcoming the increased fuel choking. The CPOX temperature is maintained below 1000 K during the transient.

3.3.3 Robustness Against CB Parameter Uncertainty

Since the CB temperature is a critical measurement in the designed feedback controller, it is important to ensure the robustness of the system against uncertainty of the CB model parameters. The dynamic response of the CB temperature is mainly a function of its mass and heat capacity constants, namely the parameter $\phi_{cb} = m_{bed}^{cb} c_{Pbed}^{cb}$. The nominal value of ϕ_{cb} used in the model and in the observer design is based on approximate data (m_{bed}^{cb}=10 kg, c_{Pbed}^{cb}=500 J/kgK, ϕ_{cb}=5000 J/K [1]). Estimation of the heat capacity or the mass of a reactor can vary significantly based on whether the catalyst, the pipes or the shell of the reactor are taken into account.

In this section we examine whether the system performance is affected when varying ϕ_{cb}. Figures 3.8 and 3.9 show the response of the plant with $0.8\phi_{cb}$, ϕ_{cb} and $1.2\phi_{cb}$ during a 100-150A load step change with FF and FF-FB. The hydrogen starvation period and the maximum CPOX temperatures remain practically unchanged in all three cases for both control schemes. Even though with FF control the response time of T_{cb} varies when ϕ_{cb} changes, the FF-FB performance is not affected.

3.3.4 Robustness Against Fuel Composition Uncertainty

The initial analysis of the system was done using a 100% pure methane natural gas fuel. Natural gas consists of 87% to 96% (molar ratio) of methane and normally includes small amounts of ethane, propane and nitrogen. Traces of butane, pentane, hexanes, carbon dioxide and hydrogen can also be found in natural gas [21]. The exact fuel composition varies depending on the place of fueling and after-treatment methods applied to the extracted natural gas. The effects of variable natural gas composition have been studied extensively in direct injection engines and have been found to have a big effect in ignition delay and peak temperature [48]. The performance of the fuel cell based system under investigation is also greatly affected in terms of the hydrogen production and CPOX temperature as shown

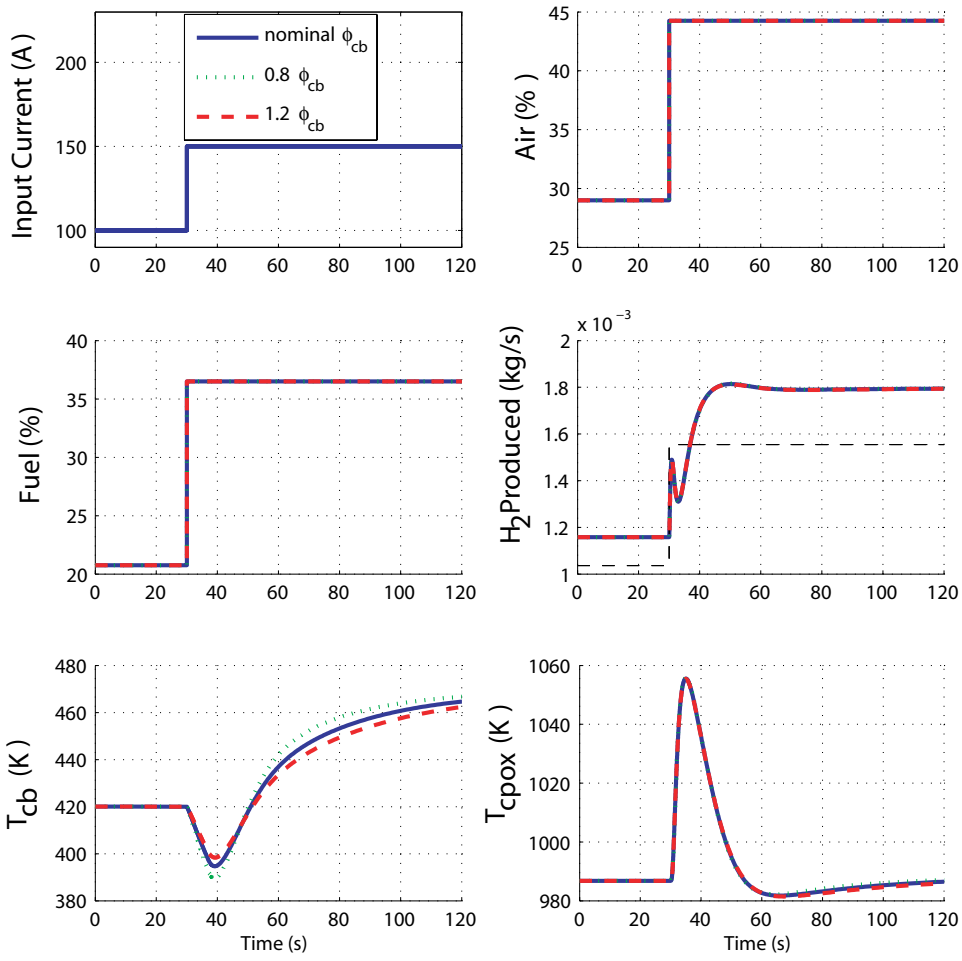

Figure 3.8: System Response with FF control for various ϕ_{cb}

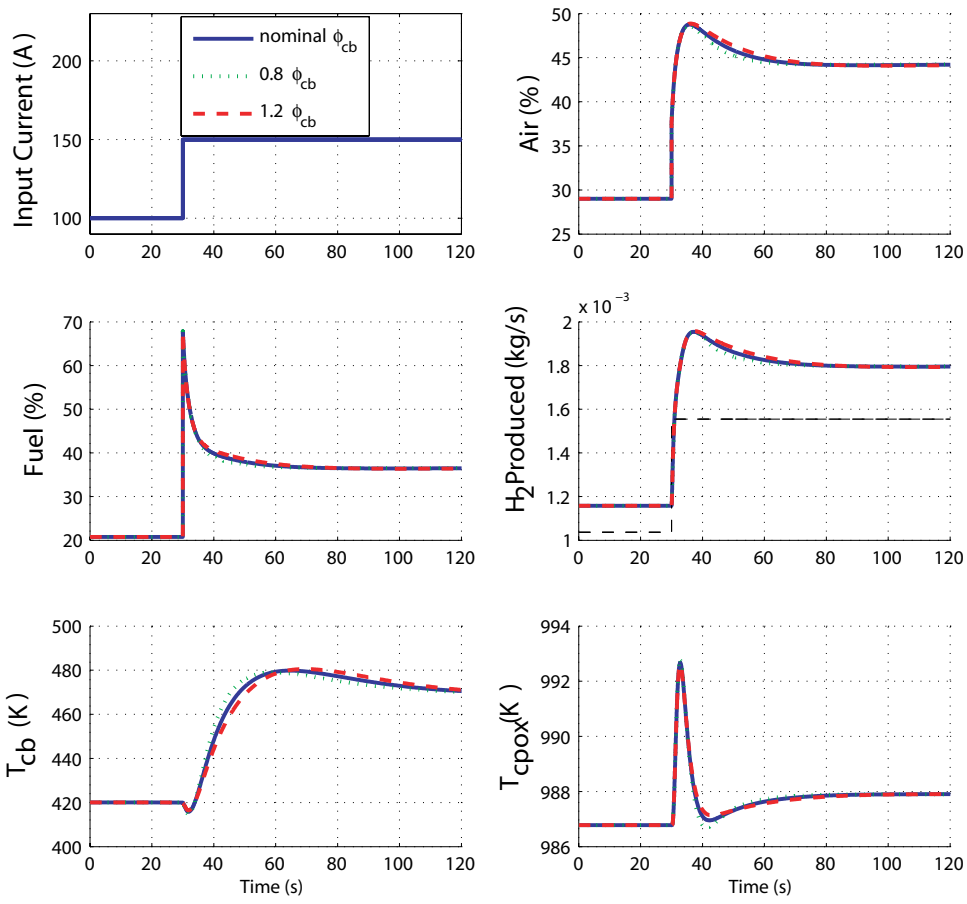

Figure 3.9: System Response with FF-FB control for various ϕ_{cb}

Table 3.2: Fuel Compositions Examined

(Mole %)	Fuel 1	Fuel 2	Fuel 3
CH_4	100	87.0	94.9
C_2H_6	0	5.2	2.5
C_3H_8	0	1.9	0.7
N_2	0	5.6	1.6
Other	0	0.3	0.3

here.

Using an equilibrium Gibbs minimization reactor, as in the initial model, it is verified that the CPOX reaction products as a function of the O_2/C ratio defined for the new fuel do not change for the same temperature conditions. Thus, the same maps can be employed (as in Figure 2.3). The fact that no fuel component other than methane is found in the output products, even at low λ_{O2C} ratios, can be explained by the relatively large methane content in the fuel (>87%) and increased selectivity of ethene and propane against methane in the oxidation reaction (i.e., ethane and propane are oxidized first) [3]. The fact that the maps are the same, though, does not guarantee the same hydrogen production due to the potential different equilibrium temperature when using the predetermined feedforward maps for air and fuel commands (i.e., same air and fuel flows for variable fuel compositions).

In order to account for variable composition in the reformer mixture, the CPOX temperature dynamics are now expressed as

$$\frac{dT^{cpox}}{dt} = \frac{1}{m^{cpox}c_P^{cpox}}[W^{cpox}(c_P^{mix}(T^{mix} - T_{ref}) - \\ -c_P^{cpox}(T^{cpox} - T_{ref})) + \Delta H^0] \tag{3.20}$$

where the heat capacity of the incoming flow from the mixer, c_P^{mix}, is now a weighted sum of all the species in the fuel and air composition while the enthalpy of formation of the inlets minus the products, ΔH^0, also takes into account the ethane, propane and other species in the fuel. The fuels examined in this work are given in Table 3.2, where "*Other*" indicates traces of butane, pentane and oxygen. The corresponding steady state and transient FF response of the system using these three fuels is given in Figure 3.10 while the closed loop in Figure 3.11.

In Figure 3.10, the FF controlled scheme exhibits prolonged hydrogen starvation when *Fuel 2* and *Fuel 3* are used, while the CPOX temperature is also significantly increased for these fuels. Note, that the CPOX temperature overshoot remains constant, contrary to the previous scenarios examined and it is the steady state values that are mainly affected. This was also verified by examining the eigenvalue (pole) of equation 3.20 which remains

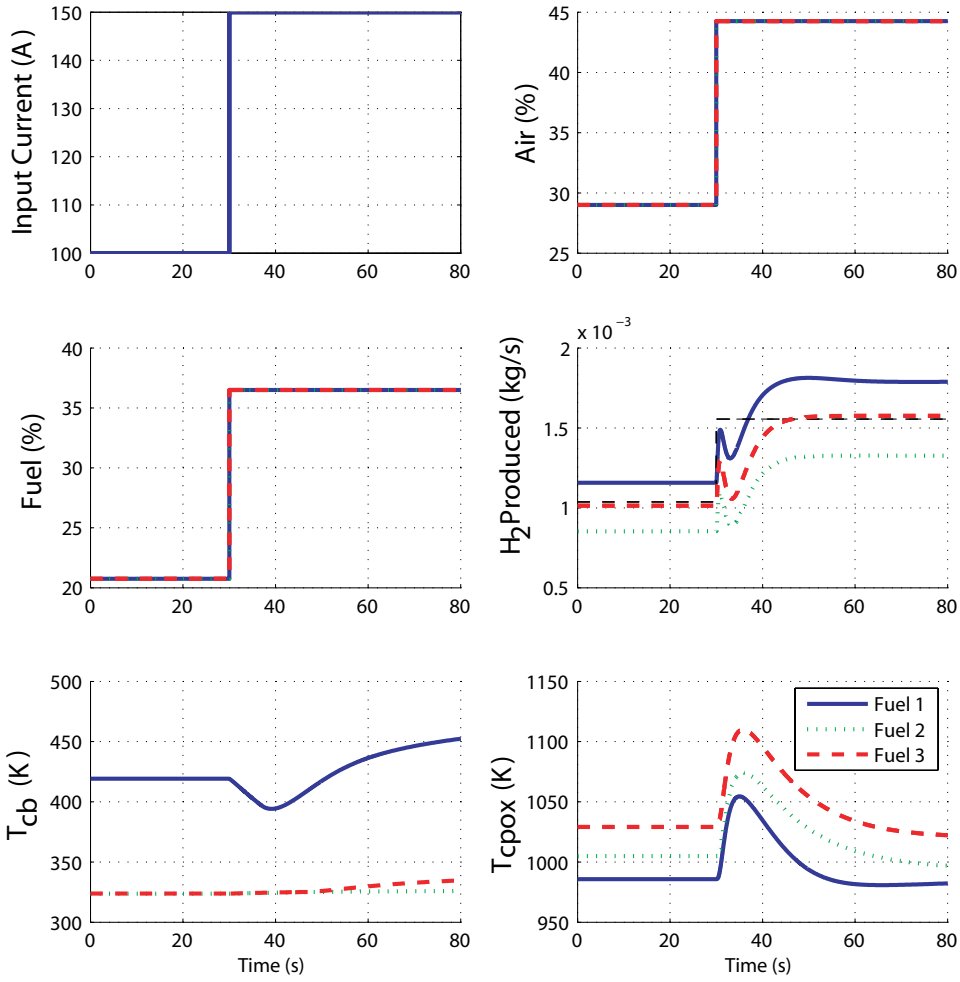

Figure 3.10: System Response with FF control for various fuels

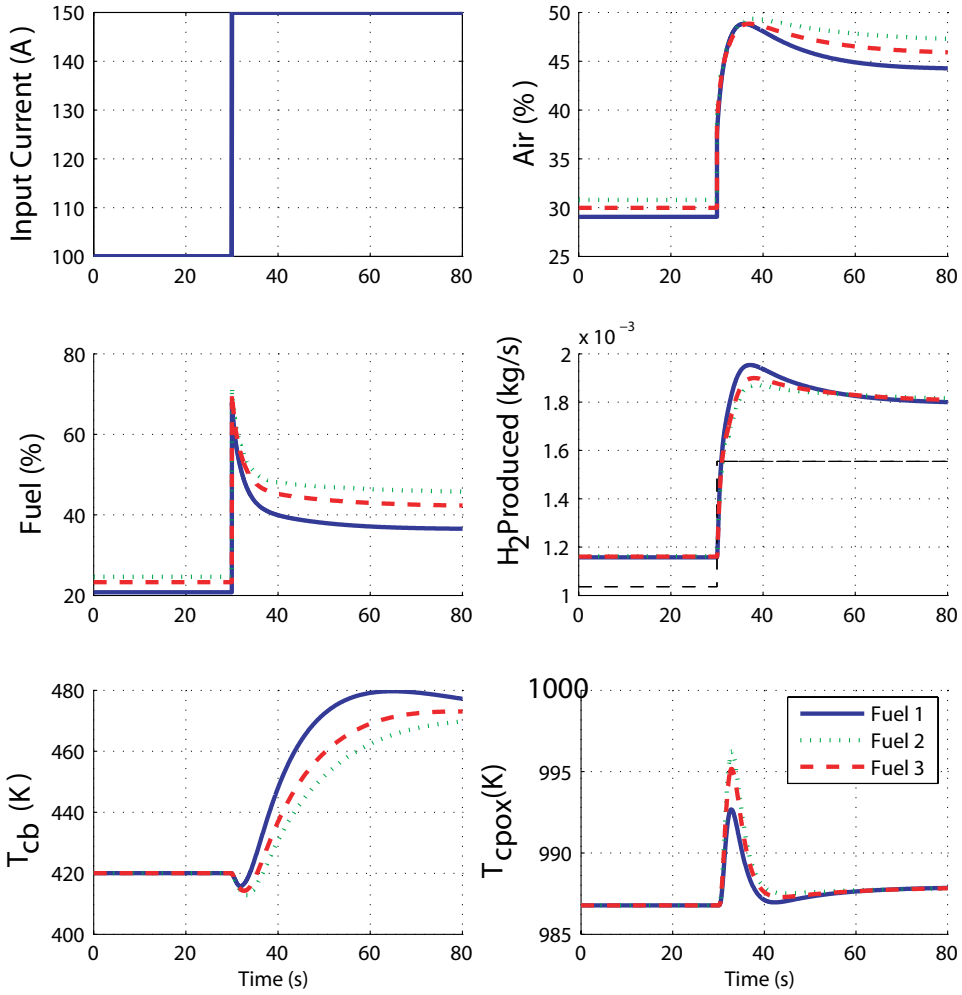

Figure 3.11: System Response with FF-FB control for various fuels

constant, for all three fuels, i.e., the thermal capacity of the mixture is practically constant since methane content is large in all fuels.

The FF-FB performance with all three fuels is acceptable as far as hydrogen and CPOX temperature responses are concerned. The degradation of the SP is negligible while the deterioration in CPOX temperature overshoot is small and can be attributed to the slight increase in reformer pressure due to the shifted air and fuel commands. Thus, the ability of the controller to provide an acceptable performance can be attributed mainly to the integral action.

CHAPTER 4

Model of a Hybrid Solid Oxide Fuel Cell and Gas Turbine System

4.1 Introduction

Hybrid solid oxide fuel cell (SOFC) and gas turbine (GT) systems provide a means of clean, efficient and high density power production. In addition, the fueling flexibility of SOFC systems makes hybrid SOFC/GT systems particularly appealing for marine and military applications. The integration of SOFC and GT, however, imposes a number of challenges because of the highly complex and tightly coupled subsystem dynamics. The goal of this work is to investigate the feasibility of utilizing the hybrid Solid Oxide Fuel Cell (SOFC) and Gas Turbine (GT) power system, shown in Fig. 4.1, for shipboard applications. A system consisting of a gas turbine, a burner and an SOFC is examined to gain fundamental understanding of the system dynamics. A control-oriented dynamic model is developed to provide the critically needed tool for system feasibility analysis and control strategy design. System optimization and transient analysis are performed based on the system model to determine the desired operating conditions and load following limitations. It is shown that the open loop system will shutdown in the case of a large load step. Based on the insights from the open loop analysis and from the development of a reduced-order model, a feedback control scheme is proposed in the next chapter. The feedback scheme is composed of a reference governor, that guarantees stability during transitions and a proportional controller that improves the transient performance by adding extra fuel in the catalytic burner during the transient.

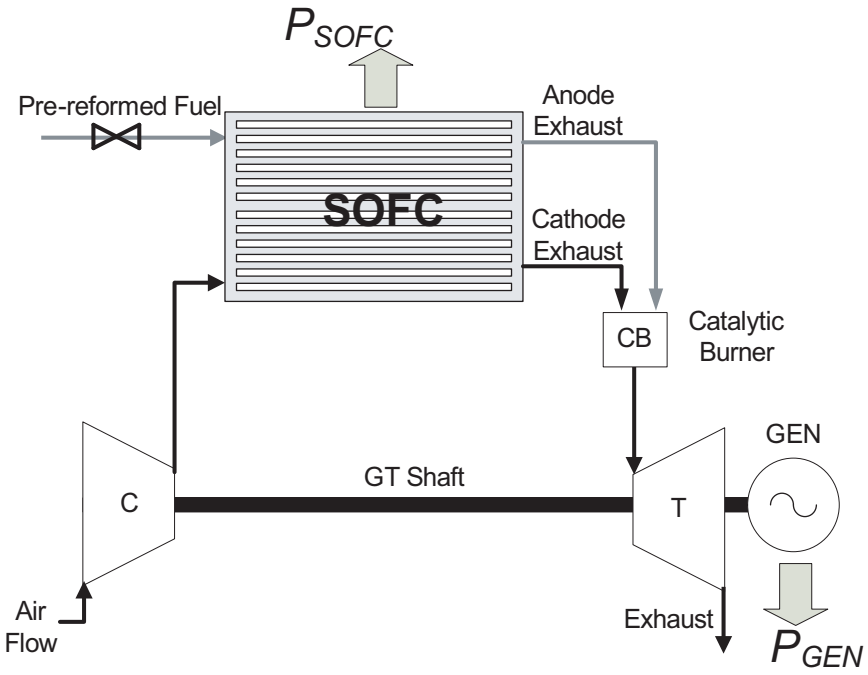

Figure 4.1: Hybrid SOFC/GT Configuration

4.2 System Overview and Operating Principles

The system investigated is shown in Fig. 4.1 and is composed of a compressor (C), an SOFC stack rated at 30kW, a catalytic burner (CB), and a turbine (T) which drives a generator (GEN). The 30 kW hybrid SOFC/GT system analyzed in this work is intended as an auxiliary power unit (APU) for military and commercial applications. Other components, such as the reformer and the heat exchangers, are not included in this work in order to focus on the coupling dynamics between the SOFC and the GT. The coupling dynamics are governed by the flow exchange between the SOFC and the GT, thus only these core components are included in our analysis. In order to further analyze the overall SOFC/GT system, including all the balance of plant (BOP) equipment, additional modeling and component integration should be performed in the future.

For the hybrid SOFC/GT system shown in Fig. 4.1, air is supplied to the cathode side of the SOFC by the compressor, while pre-reformed fuel is fed to the anode side. The exhaust from the SOFC outlet passes through the CB where the un-used fuel is burned to increase the temperature and pressure of the flow. The high temperature and high pressure flow from the CB then powers the turbine, thereby providing a mechanism to recuperate the exhaust energy. The turbine drives both the compressor and the generator; the former delivers the air needed for the SOFC stack operation and the latter provides additional electrical power for the system. The net power output is calculated as the sum of the electric power from the SOFC and the generator power. The overall model was developed in Matlab/Simulink

and can capture both the steady state and dynamic behavior of the system, while the SOFC spacial distributions of temperature and pressure are also captured. The high complexity of the SOFC model yields a 55 state model, of which 52 are from the SOFC, 2 are from the CB and 1 is from the GT shaft dynamics. For control analysis, model reduction is pursued later in this dissertation in order to gain insights on the states that are important in implementing the load following control strategies for the system.

4.3 Literature Review

Publications focusing on the dynamic behavior and load transitions of hybrid solid oxide fuel cell and gas turbine systems are fewer than the ones focusing on steady state performance in today's literature. Most work done on SOFC/GT systems includes cost and efficiency studies for optimal design and material selection. In this section, the main results and tools for prediction of the performance of SOFC/GT systems found in the literature are presented.

A cost versus efficiency analysis in [45] indicates the increase in system efficiency and reduction in cost can be achieved when a GT cycle is integrated with an SOFC. Increase in SOFC efficiency is shown by Yi in [90] when the SOFC operating pressure increases at the expense of capital cost. An efficient and low cost solution for pressurizing the SOFC system is the addition of a GT. Further increase in efficiency is observed by Yang *et. al.* when internal reforming is used [89]. Yang compares SOFC internal and external reforming and states that the advantage of the internal reforming, in terms of efficiency, is more evident in the hybrid systems than in the stand-alone SOFC system due to the higher exhaust temperature (i.e., higher exhaust energy content) and the capability of the system to harvest the exhaust energy. Steady state modeling, optimization and parametric studies in [37, 46, 51, 67, 80] determine the theoretical maximum electrical efficiency of a combined SOFC and GT cycle to be around 60%, while exergy analysis in [10] reveals that the SOFC stack, amongst the other components in the SOFC/GT cycle, has the highest energy losses (i.e., the SOFC is the least efficient out of the SOFC/GT components). Furthermore, several SOFC/GT static analysis publications, especially [80], state that energy recuperation, while it increases the steady state efficiency, imposes more stringent constraints on the thermal and load management of the system due to the higher system complexity that arises from the pressure coupling of the SOFC with the GT.

A dynamic model of an SOFC/GT system is developed in [61]. The model is validated using start up operation experimental data provided by Siemens Westinghouse and the authors note that the model, built from first principles, can reasonably predict the dynamic performance of a complex hybrid FC/GT system. The authors of [84] develop a dynamic model of an SOFC/GT system and evaluate the matching between that model and a linearized version of the same model. They note that the linear and nonlinear model responses

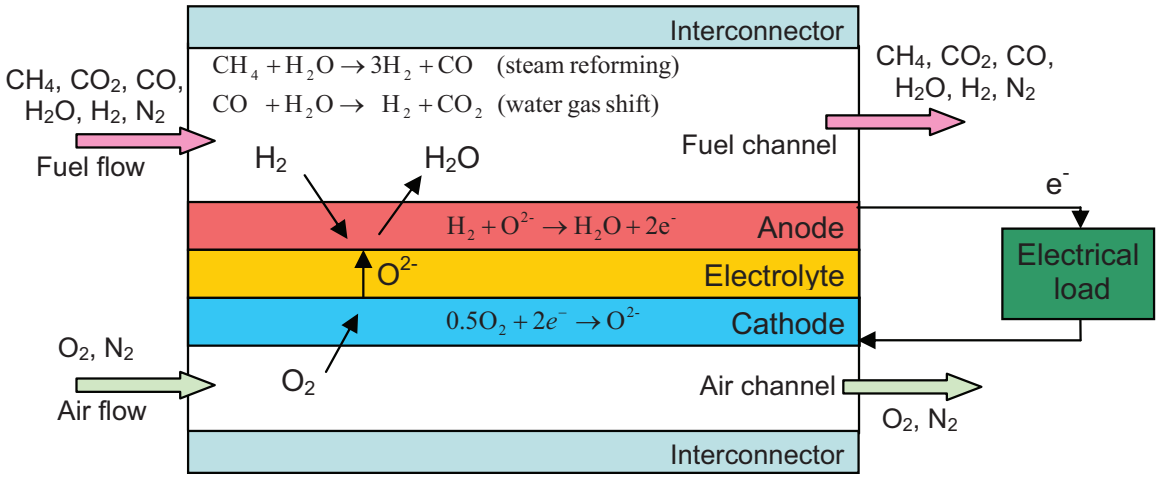

Figure 4.2: Operating principle of co-flow planar SOFCs [86].

match only for small variations (less that 10%) in the inputs. Thus, the nonlinearities cannot be ignored in the system model and performance analysis. In [70], using dynamic analysis, it is identified that regulating the shaft speed in a SOFC/GT system can be achieved by direct injection of fuel flow in the catalytic burner. Finally, the authors of [71] pointed out that: "*With a given constant generator power, the system is at an unstable equilibrium. Departing from steady-state, for example, a step increase of the generator power will lead to deceleration of the shaft speed. No new equilibrium will be found within the valid bounds of shaft speed*". The authors note that proper shaft speed regulation can be achieved via "*trial-and-error tuning of a PID controller*", using as feedback the error between the actual air flow and the air flow setpoint. The system stability, though, is not guaranteed for a load step different than the one the PID controller was tuned for. In our work a more elaborate feedback control scheme is designed to enhance stability.

4.4 Solid Oxide Fuel Cell Model

The SOFC model utilized in this work was developed by Xi in [86], where a thorough model-based control analysis was performed and the issues associated with an SOFC system coupled with a fuel reformer were addressed. It is shown that thermal management and reactant ratio control are required to ensure the transition capabilities. The model is included here for a self-contained system model presentation. In this work a co-flow (i.e., parallel-flow) SOFC arrangement is utilized as shown in Fig. 4.2. The SOFC model is composed of three separate sub-models, namely the electrochemical sub-model, the mass balance submodel and the energy balance sub-model. The full model is then developed by integrating those submodels as presented in the following sections.

Note that in this work the fuel entering the SOFC is assumed to be partially reformed,

containing $CH_4,\ CO_2,\ CO,\ H_2O,\ H_2$ and N_2, and has the following fixed molar fraction composition:

$$x_f = (x_{CH_4}, x_{CO_2}, x_{CO}, x_{H_2O}, x_{H_2}, x_{N_2}) = (0.016,\ 0.018,\ 0.163,\ 0.037,\ 0.324,\ 0.442), \tag{4.1}$$

while in the air channel, we assume:

$$x_a = (x_{O_2}, x_{N_2}) = (0.21,\ 0.79). \tag{4.2}$$

In order to capture the spatial distribution of important variables in the SOFC, such as current density and temperature, the model presented in [86] utilizes discretization via the finite-volume method. Using this approach, the cell is virtually divided into a user-defined number of units along the gas flow direction, where the electrode and electrolyte layers are considered as one assembly structure, called the PEN (Positive electrode-Electrolyte-Negative electrode). In one discretization unit, variables such as the current density, temperatures and pressures are assumed to be homogeneous. Dynamic governing equations for each unit in the SOFC model are derived by applying the electrochemical, thermal dynamic and fluid flow principles. These discretization units are then integrated to form the SOFC model by imposing the gas flow, heat exchange and current distribution relations. The following assumptions are used in [86] for developing the SOFC model:

1. The cell is considered equipotential because of the high electrical conductivities of the interconnectors (i.e., all the SOFC discretization units have the same voltage).
2. The current is produced only by the oxidation of H_2, and CO reacts only through the WGS reaction (i.e., the CO does not contribute directly to the electrochemical reaction to produce current).
3. All gases obey the ideal gas law.
4. The Nusselt number is constant and does not depend on the flow.
5. Adiabatic boundaries are assumed for the cell (i.e., no heat losses from the SOFC walls to the environment).

4.4.1 Electrochemical Sub-model

The operating voltage of one discretization unit of the cell can be calculated by:

$$U^j = U^j_{OCV} - (\eta^j_{ohm} + \eta^j_{act} + \eta^j_{con}), \quad j = 1, 2, ...J, \tag{4.3}$$

where j is the index of discretization units. U^j_{OCV} is the open circuit voltage and the last three terms in Eqn. (4.3) represent various potential losses in the jth unit. For notation simplicity, the superscript j will be omitted in the following equations. The open circuit voltage can be determined by the Nernst Equation as follows

$$U_{OCV} = E_0 - \frac{\tilde{R}T_{PEN}}{2F} ln \frac{p_{H_2O}}{p_{H_2}\, p_{O_2}^{0.5}}, \tag{4.4}$$

where T_{PEN} is the temperature in the PEN structure, p_{H_2O}, p_{H_2} and p_{O_2} are partial pressures of H_2O, H_2 and O_2, respectively, and η_{ohm} is the ohmic loss due to the internal resistance in the SOFC. The activation loss, η_{act}, is due to the energy barrier to be overcome in order for the electrochemical reaction to occur, and can be characterized by the Butler-Volmer equation. The concentration loss, η_{con}, reflects the overpotential due to the species diffusions between the reaction site and the bulk flow in the gas channels. The approach used in [4] is adopted in [86] as well to calculate the concentration overpotentials.

Finally, the polarization relation in each discretization unit, as denoted by the following nonlinear algebraic function, can be determined in the electrochemical submodel based on the local conditions, including the PEN temperature and species pressures:

$$U = f(i, p_{H_2}, p_{O_2}, p_{H_2O}, p_a, T_{PEN}), \tag{4.5}$$

where the details on the expression for the function f are given in [86]. It is noted that there is no state in the electrochemical submodel.

4.4.2 Mass Balance Sub-model

The mass accumulated in the fuel and air channels are calculated in the mass balance sub-model. Each discretization unit of the cell has eight states, representing the molar concentrations of different gas species, i.e., CH_4, CO_2, CO, H_2O, H_2 and N_2 in the fuel channel, and O_2 and N_2 in the air channel.

The mass balance dynamics in the fuel channel for one discretization unit are described as follows:

$$\dot{m}_{x_f} = W_{x_f,in} + W_{x_f,produced} - W_{x_f,out}, \tag{4.6}$$

where m_{x_f} is the mass in the fuel channel of species x_f and $W_{x_f,in}$, $W_{x_f,produced}$, $W_{x_f,out}$ are the inlet, produced and outlet flow of species x_f in the fuel channel. Note that the produced flow of species x_f is a function of the reaction rates, as presented in [86].

Similarly, the mass balance dynamics in the air channel are expressed as:

$$\dot{m}_{x_a} = W_{x_a,in} + W_{x_a,produced} - W_{x_a,out}, \tag{4.7}$$

where m_{x_a} is the mass in the air channel of species x_a and $W_{x_a,in}$, $W_{x_a,produced}$, $W_{x_a,out}$ are the inlet, produced and outlet flow of species x_a in the air channel, respectively. Similarly, the produced flow of species x_a is a function of the reaction rate.

4.4.3 Energy Balance Sub-model

The temperature dynamics in the SOFC are calculated in this submodel. In the planar SOFC model, the cell is usually divided into several temperature layers to represent the temperature distribution along the axis perpendicular to the cell plate. In the model presented in [86], there are five layers, namely the fuel bulk flow, the air bulk flow, the PEN, the fuel-side interconnector and the air-side interconnect in each discretization unit of the SOFC. For the cells at the boundaries of the stack, the fuel/air-side interconnectors have to be considered as separate temperature layers in the model.

The temperatures of these layers are calculated by solving the dynamic equations of energy balance in each layer. The heat transfer considered in the model includes the convection between the bulk flows and their surrounding solid structures, the conduction in solid layers as well as radiation between PEN and interconnectors.

The energy balance dynamics in the fuel flow can be expressed as follows:

$$\dot{T}_f = \frac{1}{\sum_{x_f} c_{v,x_f} m_{x_f}} \left(H^{abs}_{in,f} - H^{abs}_{out,f} + Q^{conv}_{PEN/f} + Q^{conv}_{I/f} + Q_{r,f} \right), \tag{4.8}$$

where $H^{abs}_{in,f} - H^{abs}_{out,f}$ accounts for the inlet and outlet absolute enthalpy difference in the fuel channel, $Q^{conv}_{PEN/f}$ and $Q^{conv}_{I/f}$ account for the convective heat exchange between the fuel flow and its surrounding solid layers, namely the PEN and I layers, and $Q_{r,f}$ is the energy released from the oxidation reaction in the anode. Details on each of those terms can be found in [86].

Similarly, for the air flow, we have

$$\dot{T}_a = \frac{1}{\sum_{x_a} c_{v,x_a} m_{x_a}} \left(H^{abs}_{in,a} - H^{abs}_{out,a} + Q^{conv}_{PEN/a} + Q^{conv}_{I/a} - Q_{r,a} \right), \tag{4.9}$$

and for the PEN structure:

$$\dot{T}_{PEN} = \frac{1}{m_{PEN} c_{p,PEN}} \left(Q^{cond}_{PEN} - Q^{conv}_{PEN/f} - Q^{conv}_{PEN/a} + Q_{r,PEN} + Q^{rad}_{PEN} - iU_{cell} \right), \tag{4.10}$$

where m_{PEN}, $c_{p,PEN}$ are mass and heat capacity of the PEN structure, respectively. The Q^{cond}_{PEN} term in (4.10) accounts for the conductive heat transfer in the PEN structure, the $Q^{conv}_{PEN/f}$, $Q^{conv}_{PEN/a}$ terms account for the convective heat exchange between the PEN and its surrounding gas flows, the $Q_{r,PEN}$ term accounts for the energy released by the electrochemical reaction, Q^{rad}_{PEN} accounts for the radiation from interconnectors to PEN and iU for the electrical work done by the cell.

Similarly, for the interconnector, we have

$$\dot{T}_I = \frac{1}{m_I c_{p,I}} \left(Q^{cond}_I - Q^{conv}_{I/f} - Q^{conv}_{I/a} - Q^{rad}_I \right). \tag{4.11}$$

Finally, given the total mass in each channel and the temperature, the corresponding pressure is calculated using the ideal gas law.

4.4.4 SOFC Cell Model

The model of the SOFC is then obtained by integrating the dynamic equations of all the discretization units and following the flow continuity, boundary conditions and current distribution relations.

Based on the equipotential assumption, the following relations are imposed among the discretization units:

$$U^j = U_{cell}, \quad j = 1, 2, ..., J, \tag{4.12}$$

$$\sum_{j=1}^{J} I^j = I_{tot}, \tag{4.13}$$

where J is the total number of discretization units, U_{cell} the operating voltage of the cell, I^j and I_{tot} are the currents drawn from the jth unit and the whole cell, respectively.

By the continuity of the gas flows in a co-flow SOFC, we assume that the flow exiting the $j-1$ unit of the fuel or air channel is equal to the flow entering unit j:

$$W^j_{in,f} = W^{j-1}_{out,f}, \tag{4.14}$$

$$W^j_{in,a} = W^{j-1}_{out,a}. \tag{4.15}$$

$$\tag{4.16}$$

Given the small pressure drop across the fuel cell, it is assumed that the flow exiting

the fuel and air channels is governed by the linear orifice equation:

$$W^j_{out,f} = k_f(p^j_f - p^{j+1}_f), \tag{4.17}$$
$$W^j_{out,a} = k_a(p^j_a - p^{j+1}_a), \tag{4.18}$$

where k_f, k_a are the orifice coefficients and p^j_a, p^j_f are the pressures of the air or fuel channels at the j^{th} unit.

Finally, assuming adiabatic boundaries, we have

$$T^0_{PEN} = T^1_{PEN} \quad , \quad T^{J+1}_{PEN} = T^J_{PEN}, \tag{4.19}$$
$$T^0_I = T^1_I \quad , \quad T^{J+1}_I = T^J_I. \tag{4.20}$$

4.4.5 Selection of Number of Units

The selection of discretization units is an important modeling parameter, which has significant impact on the model accuracy and computation load. Figure 4.3 shows the simulation results of steady-state current density profiles for different numbers of units under the same operating condition [86]. Refined discretization grids can provide more accurate spatial profiles of the variables, such as the temperature and current density distributions, and therefore lead to improved representation of the fuel cell behaviors. However, the computation time increases drastically as the number of the discretization units increases.

In this work, since the interaction of the SOFC with the CB and the GT, and not the SOFC itself, is the main focus, we use the SOFC model with a minimum of 4 discretization units that are shown to capture adequately the average temperature and current distribution profile [86].

4.5 Turbine and Compressor Model

The GT model incorporates the shaft rotational speed dynamics, the compressor and the turbine sub-model. Only the shaft dynamics are considered, while the turbine and compressor are modeled using static algebraic equations. The main variables used in those models include pressure p, flow W, temperature T and power P. Note that the subscripts denote the component (c for compressor and t for turbine) and the inlet or outlet (*1* or *2*, respectively). For example, T_{c2} denotes the outlet temperature of the compressor. A schematic, with all the main variables denoted at their corresponding position, is shown in Fig. 4.4.

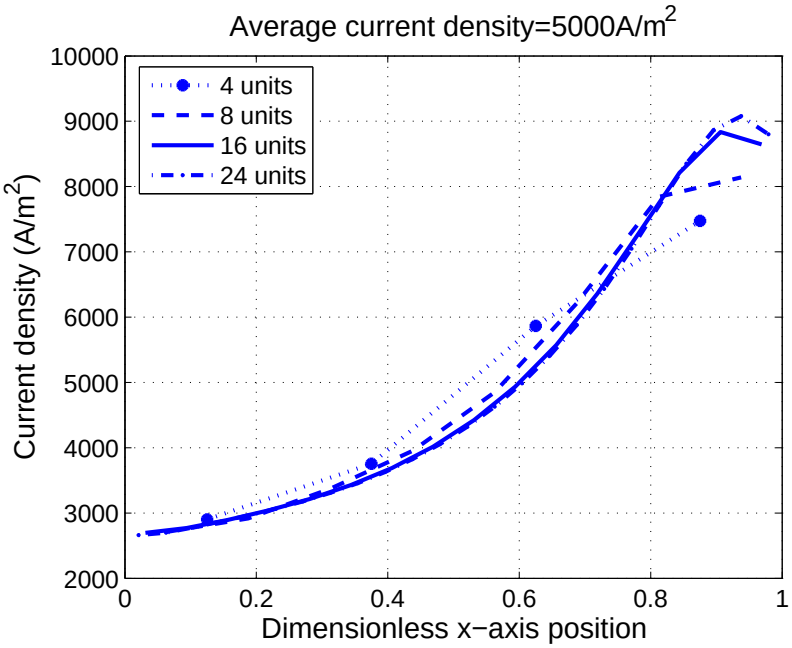

Figure 4.3: Current density profiles for different number of discretization units [86].

4.5.1 Shaft Rotational Speed Dynamics

The turbocharger rotational dynamics are determined by the power generated by the turbine, P_t (W), the power required to drive the compressor P_c (W) and the power drawn by the generator P_{gen} as:

$$\frac{dN}{dt} = \frac{P_t \eta_m - P_c - P_{gen}}{\alpha \cdot N \cdot J}, \tag{4.21}$$

where N is the turbocharger speed in rpm and η_m is the turbine mechanical efficiency that accounts for energy losses due to friction. The turbine efficiency is considered constant and equal to a typical value of 0.95. The turbocharger inertia $J = 1.27 \cdot 10^{-3}$ $(kg \cdot m^2)$ is the sum of rotor inertia, compressor inertia and turbine wheel inertia about the axis of rotation. The factor $\alpha = (2\pi/60)^2$ is a result of converting the speed from rad/s to revolutions per minute (rpm).

4.5.2 Compressor Model

Neglecting heat losses, the power P_c required to drive the compressor can be related to the mass flow rate through the compressor, W_c, and the total enthalpy change across the compressor from the first law of thermodynamics as

$$P_c = W_c(h_{c2} - h_{c1}), \tag{4.22}$$

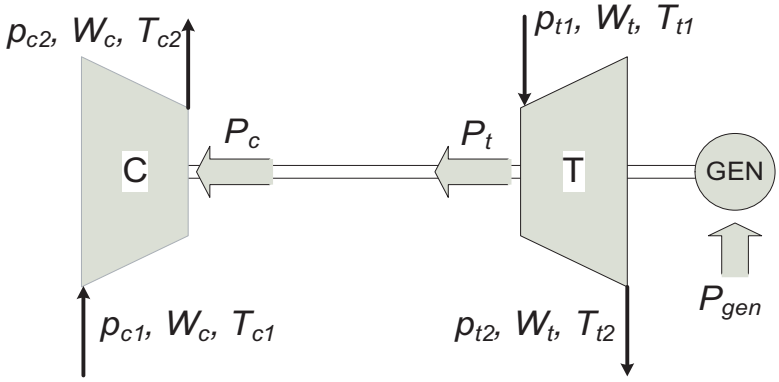

Figure 4.4: Compressor, Turbine, Shaft and Generator Schematic

where h_{c1} and h_{c2} are the enthalpy of the inlet and the outlet flow, respectively. Assuming that the specific heat coefficients of air do not change, we have:

$$P_c = W_c c_p^{air}(T_{c2} - T_{c1}), \tag{4.23}$$

where T_{c1} and T_{c2} are the absolute temperature at the inlet and the outlet of the compressor, respectively, and c_p^{air} is the specific heat coefficient of the air. If c_p^{air} is specified in J/gK, W_c in g/s and $T_{c1},\ T_{c2}$ are in K, then the units of P_c are (W). For an isentropic process, the temperature ratio can be related to the pressure ratio (i.e., compressor outlet pressure, p_{c2}, over inlet pressure, p_{c1}) using the relation:

$$\left(\frac{T_{c2,is}}{T_{c1}}\right) = \left(\frac{p_{c2}}{p_{c1}}\right)^{\frac{\gamma-1}{\gamma}}, \tag{4.24}$$

where γ is defined as the ratio of the constant pressure specific heat over the constant volume specific heat as

$$\gamma = c_p/c_v. \tag{4.25}$$

To account for the fact that the compression process is not isentropic, the compressor isentropic efficiency, η_c, is introduced:

$$\eta_c = \frac{T_{c2,is} - T_{c1}}{T_{c2} - T_{c1}}. \tag{4.26}$$

Then, the compressor outlet temperature, T_{c2}, and consumed power, P_c, are expressed as:

$$T_{c2} = T_{c1} \cdot \left(1 + \frac{1}{\eta_c}\left(\left(\frac{p_{c2}}{p_{c1}}\right)^{\frac{\gamma-1}{\gamma}} - 1\right)\right), \tag{4.27}$$

$$P_c = W_c c_p^{air} T_{c1} \frac{1}{\eta_c}\left(\left(\frac{p_{c2}}{p_{c1}}\right)^{\frac{\gamma-1}{\gamma}} - 1\right). \tag{4.28}$$

It is conventional to specify the compressor map (Fig. 4.5) in terms of non-dimensional mass flow rate parameter, ϕ_c, and compressor rotational speed parameter, $\bar{N}_c$, that are defined as:

$$\phi_c = \frac{W_c\sqrt{T_{c1}}}{p_{c1}}, \tag{4.29}$$

$$\bar{N}_c = \frac{N}{\sqrt{T_{c1}}}. \tag{4.30}$$

Figure 4.5 depicts the compressor map utilized in this work for $\bar{N}_c$ ranging from 5500 to 10500 with a 500 step, with p_{c2}/p_{c1} as a function of ϕ_c. For each speedline, there are two limits to the flow range. The upper limit is due to choking, when the flow reaches the velocity of sound at some cross-section. In this regime no further flow increase can be obtained by reducing the compressor outlet pressure and the speedline slope becomes infinite. The lower limit is due to a dangerous instability known as surge. During surging a noisy and often violent flow process can occur causing periods of backflow through the compressor. The specific value of ϕ_c at which surge occurs depends not only on the compressor characteristics but also on the properties of the installation downstream of the compressor. Typically, this value is where the slope of the speedline is zero or slightly positive. The left-hand extremities of the speedlines may be joined up to form what is known as the surge line.

Instead of utilizing the maps as lookup tables, it is preferred to express them in a functional form with coefficients determined from the experimental data. This guarantees a smooth interpolation between data points and allows extension of the maps beyond the region for which experimental data are available. For the maps utilized in this work, the fitting expressions and the methodology used to derive them are discussed next.

For each speedline, the maximum efficiency value is denoted by $\eta_{c,max}(\bar{N}_c)$ and the value of ϕ_c where $\eta_{c,max}(\bar{N}_c)$ is achieved is denoted as $\phi_{c,max}(\bar{N}_c)$. The functions $\eta_{c,max}(\bar{N}_c)$ and $\phi_{c,max}(\bar{N}_c)$ can be approximated by the following polynomials as:

$$\eta_{c,max}(\bar{N}_c) = (14.76 + 0.0146\bar{N}_c - 8.562 \cdot 10^{-7}\bar{N}_c^2)/100, \tag{4.31}$$

$$\phi_{c,max}(\bar{N}_c) = -0.002616 + 2.5851 \cdot 10^{-6}\bar{N}_c. \tag{4.32}$$

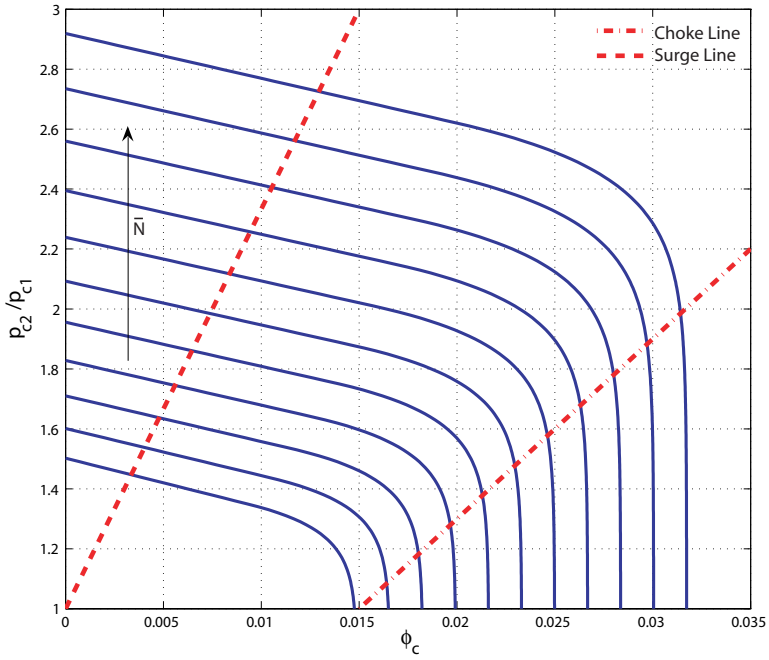

Figure 4.5: Compressor map as a function of ϕ_c and p_{c2}/p_{c1} for $\bar{N}_c$ ranging from 5500 to 10500 with 500 units increments

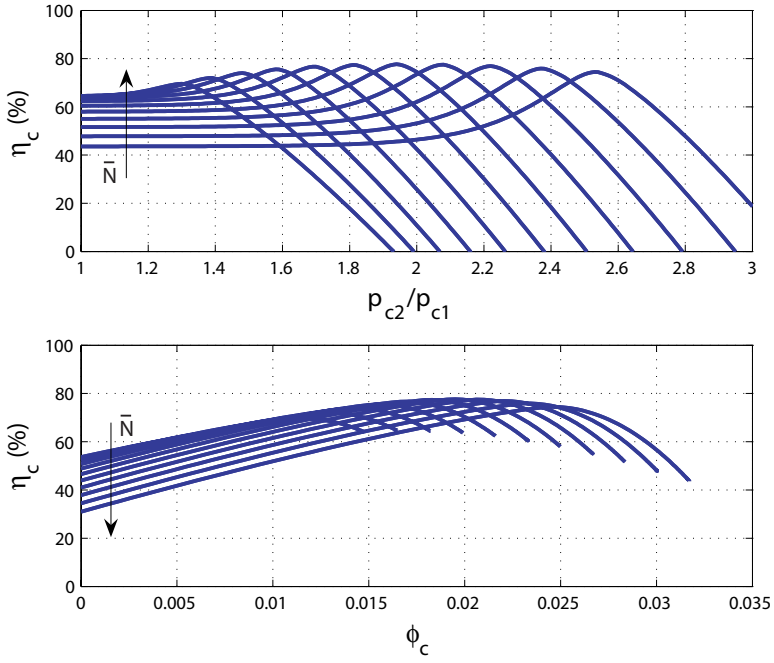

Figure 4.6: Compressor Efficiency vs. ϕ_c and p_{c2}/p_{c1} for $\bar{N}_c$ ranging from 5500 to 10500 with 500 units increments

Then,

$$\frac{\eta_c}{\eta_{c,max}(\bar{N}_c)} = \begin{cases} 1 - 60(\phi_{c,max}(\bar{N}_c) - \phi_c)^{5/4}, & \phi_c \leq \phi_{c,max}(\bar{N}_c) \\ 1 - 8000(\phi_c - \phi_{c,max}(\bar{N}_c))^2, & \phi_c > \phi_{c,max}(\bar{N}_c) \end{cases} . \tag{4.33}$$

Furthermore, to develop a representation of ϕ_c, we express the values of ϕ_c on the choke line, $\phi_c^{ch}(\bar{N}_c)$, and the pressure ratio values on the choke line, $PR_c^{ch}(\bar{N}_c)$ as:

$$\phi_c^{ch}(\bar{N}_c) = -0.00232 + 2.131 \cdot 10^{-6}\bar{N}_c, \tag{4.34}$$

$$PR_c^{ch}(\bar{N}_c) = 0.926 - 1.651 \cdot 10^{-5}\bar{N}_c + 1.692 \cdot 10^{-8}\bar{N}_c^2. \tag{4.35}$$

Then

$$\frac{\phi_c}{\phi_c^{ch}(\bar{N}_c)} = \begin{cases} 1 + 0.5819(1 - exp(15(p_{c2}/p_{c1}/PR_c^{ch}(\bar{N}_c) - 1))) & , \frac{p_{c2}}{p_{c1}} \leq PR_c^{ch}(\bar{N}_c) \\ 1 - 8.728((p_{c2}/p_{c1}/PR_c^{ch}(\bar{N}_c) - 1) & , \frac{p_{c2}}{p_{c1}} > PR_c^{ch}(\bar{N}_c) \end{cases} . \tag{4.36}$$

The curves resulting from this fitting are shown in Fig. 4.6.

4.5.3 Turbine Model

The turbine is powered by the energy of the exhaust gas. The power output of the turbine, P_t, can be obtained from the first law of thermodynamics, neglecting the heat transfer, as:

$$P_t = W_t(h_{t1} - h_{t2}), \tag{4.37}$$

where h_{t1} and h_{t2} are the enthalpy of the inlet and the outlet turbine flow, respectively. Treating the exhaust gas as an ideal gas (constant specific heat), we obtain:

$$P_t = W_t c_p(T_{t1} - T_{t2}), \tag{4.38}$$

where the units are the same as in (4.23). For a given pressure ratio across the turbine, the outlet temperature can be computed assuming isentropic expansion,

$$\left(\frac{T_{t1}}{T_{t2,is}}\right) = \left(\frac{p_{t1}}{p_{t2}}\right)^{\frac{\gamma-1}{\gamma}}, \tag{4.39}$$

where $T_{t2,is}$ is the temperature of the exhaust gas leaving the turbine if the expansion were isentropic. In turn, the turbine isentropic efficiency defined as

$$\eta_t = \frac{T_{t1} - T_{t2}}{T_{t1} - T_{t2,is}}, \tag{4.40}$$

is used to get the following expressions for the turbine outlet temperature and power:

$$T_{t2} = T_{t1} \cdot \left(1 - \eta_t \left(1 - \left(\frac{p_{t2}}{p_{t1}}\right)^{\frac{\gamma-1}{\gamma}}\right)\right), \tag{4.41}$$

$$P_t = W_t c_p T_{t1} \eta_t \left(1 - \left(\frac{p_{t2}}{p_{t1}}\right)^{\frac{\gamma-1}{\gamma}}\right). \tag{4.42}$$

As in the compressor maps, it is conventional to use the non-dimensional mass flow rate parameter, ϕ_t, and compressor rotational speed parameter, $\bar{N}_t$, that are defined as:

$$\phi_t = \frac{W_t\sqrt{T_{t1}}}{p_{t1}}, \tag{4.43}$$

$$\bar{N}_t = \frac{N}{\sqrt{T_{t1}}}. \tag{4.44}$$

For the turbine maps used in this work, the mass flow parameter is not a function of the shaft speed. The actual equation for the flow through the turbine is given as:

$$W_t = \frac{A_{eff} p_{t2}}{T_{t2}} \sqrt{\left(\frac{p_{t1}}{p_{t2}} - g + 1\right)^{2/\gamma} - \left(\frac{p_{t1}}{p_{t2}} - g + 1\right)^{(\gamma+1)/\gamma}}, \tag{4.45}$$

where $A_{eff} = 0.07\text{m}^2$ is the effective flow area and $g = 0.9$ is pressure ratio where the flow becomes zero. The result of this fitting is shown in Fig. 4.7. Finally, the isentropic efficiency is given as a function of the the blade-speed ratio U/C, defined as:

$$U/C = \frac{\pi D N}{\sqrt{2c_p T_{t1}\left(1 - \left(\frac{p_{t2}}{p_{t1}}\right)^{\frac{\gamma-1}{\gamma}}\right)}}, \tag{4.46}$$

where D denotes the turbine blade diameter. Note that, similar to the flow calculations, the efficiency was not considered as a function of the shaft rotational speed. Figure 4.8, shows the relationship between the blade-speed ratio, U/C, and the isentropic efficiency η_t.

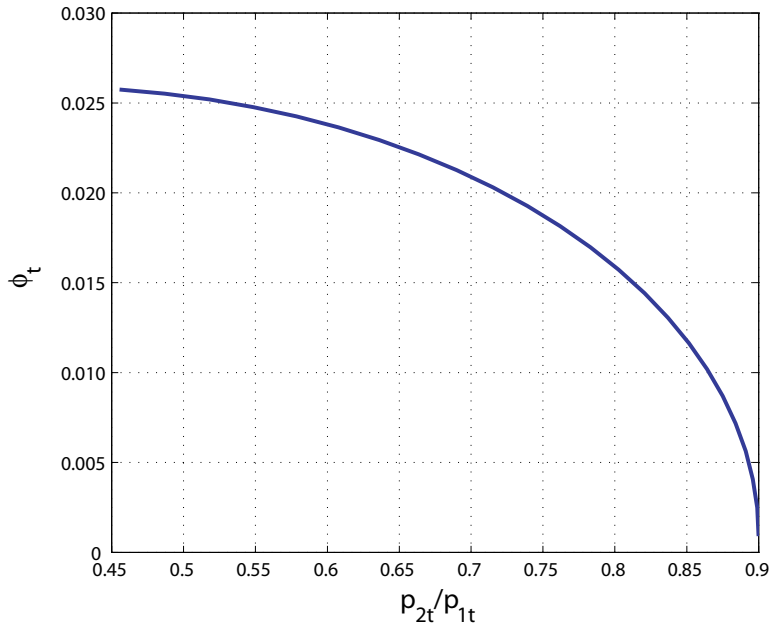

Figure 4.7: Turbine map as a function of ϕ_t and p_{t2}/p_{t1}

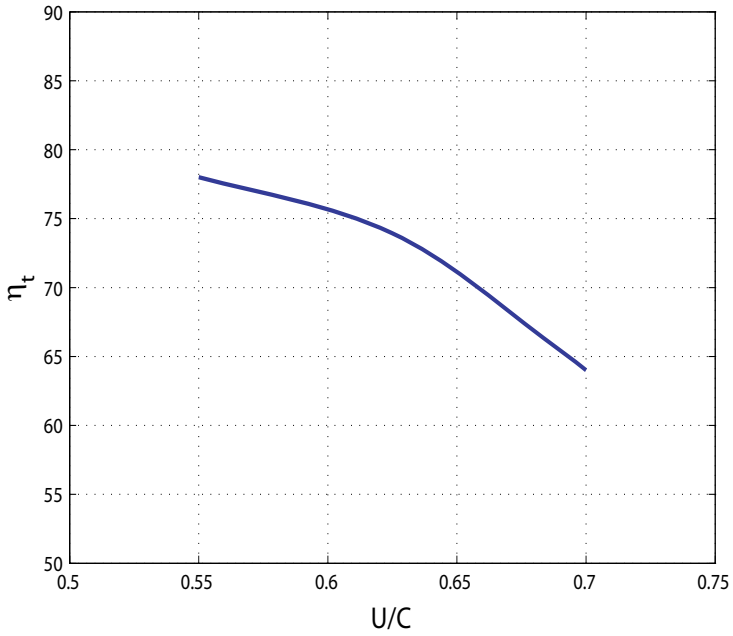

Figure 4.8: Turbine Efficiency vs. blade-speed ratio

4.6 Catalytic Burner Model

The catalytic burner (CB) is the device where the remaining fuel from the SOFC anode is burnt with the remaining air from the SOFC cathode in order to increase the flow temperature before it enters the turbine. In modeling the CB, the dynamics taken into account are the mass dynamics via the mass balance as

$$\frac{dm_{cb}}{dt} = W_{ca} + W_{an} - W_t, \tag{4.47}$$

where W_{an}, W_{ca} are the anode and cathode outlet mass flows, respectively, and W_t is the flow through the turbine.

The temperature dynamics are expressed using the energy conservation:

$$m_{bed}^{cb} c_{p,bed}^{cb} \frac{dT_{cb}}{dt} = \left(H_{T_{cb}}^{in} - H_{T_{ref}}^{in} - H_o^{in}\right) - \left(H_{T_{cb}}^{out} - H_{T_{ref}}^{out} - H_o^{out}\right), \tag{4.48}$$

where $H_{T_{cb}}$, $H_{T_{ref}}$ are the enthalpies of the inlet or the outlet flow at temperatures T_{cb} and T_{ref}, respectively, while H_o is the enthalpy of formation of the inlet or outlet flow. Note that m_{bed}^{cb} and $c_{p,bed}^{cb}$ are properties of the CB bed reactor and thus are considered constant.

Furthermore, the enthalpies at a given temperature T are calculated as:

$$H_T = \sum_{i=1}^{n} n_i c_p^i(T) T, \tag{4.49}$$

where n_i is the molar flow of species i, c_p^i is the specific heat of species i as a function of temperature and T is the temperature at which the enthalpy is calculated. In order to calculate the outlet flow composition, and in turn the outlet enthalpy $H_{T_{cb}}^{out}$, we assume that the remaining H_2 and CO are oxidized instantaneously (i.e., equilibrium reactor).

The ideal gas law is used to calculate the pressure in the CB as

$$P_{cb} = \frac{m_{cb} R T_{cb}}{V_{cb} M_{cb}}. \tag{4.50}$$

Note that the pressure of the CB is considered as the inlet pressure of the compressor. Finally, the difference of this model and the CB model used in the reformer system presented in Ch. 2, is that temperature dependent quadratic polynomials were used for the specific heat capacity of each species entering or leaving the CB and also the CO oxidation, besides H_2, is taken into account in this model.

4.7 System Model

The overall model of the hybrid SOFC/GT system is obtained by integrating the component models. A corresponding schematic denoting all the states, inputs, controls and main variables is shown in Fig. 4.9. In order to integrate the submodels the following conditions and assumptions were used:

1. The compressor outlet pressure is equal to the pressure of the first SOFC discretization unit.
2. The turbine inlet pressure is equal to the pressure of the catalytic burner.
3. The air and fuel flow from the SOFC to the CB is dictated by the pressure difference between the last SOFC discretization unit and the CB.
4. The flow out of the CB is dictated by the turbine maps, i.e. given the pressure and temperature conditions at the CB outlet, the turbine maps yield the flow out of the CB and through the turbine.
5. The fuel flow in the SOFC does not have any dynamics and is thus always equal to the commanded fuel flow.
6. The generator load is an input to the system and is utilized in determining the shaft rotational speed through the shaft dynamics.

The first two assumptions are commonly used in turbocharger modeling and the calculation error is negligible. The fifth assumption could potentially affect the system performance, though, most systems incorporate fuel buffer that allows for fast fuel changes. Finally, note that the actuators used to control the system are the fuel flow, W_f, the current drawn from the SOFC stack, I_{st}, and the generator load, P_{gen} as highlighted in Fig. 4.9. Open loop simulations of the integrated model are shown in the next chapter, after the optimal setpoints for the three actuators are derived by maximizing the system's efficiency.

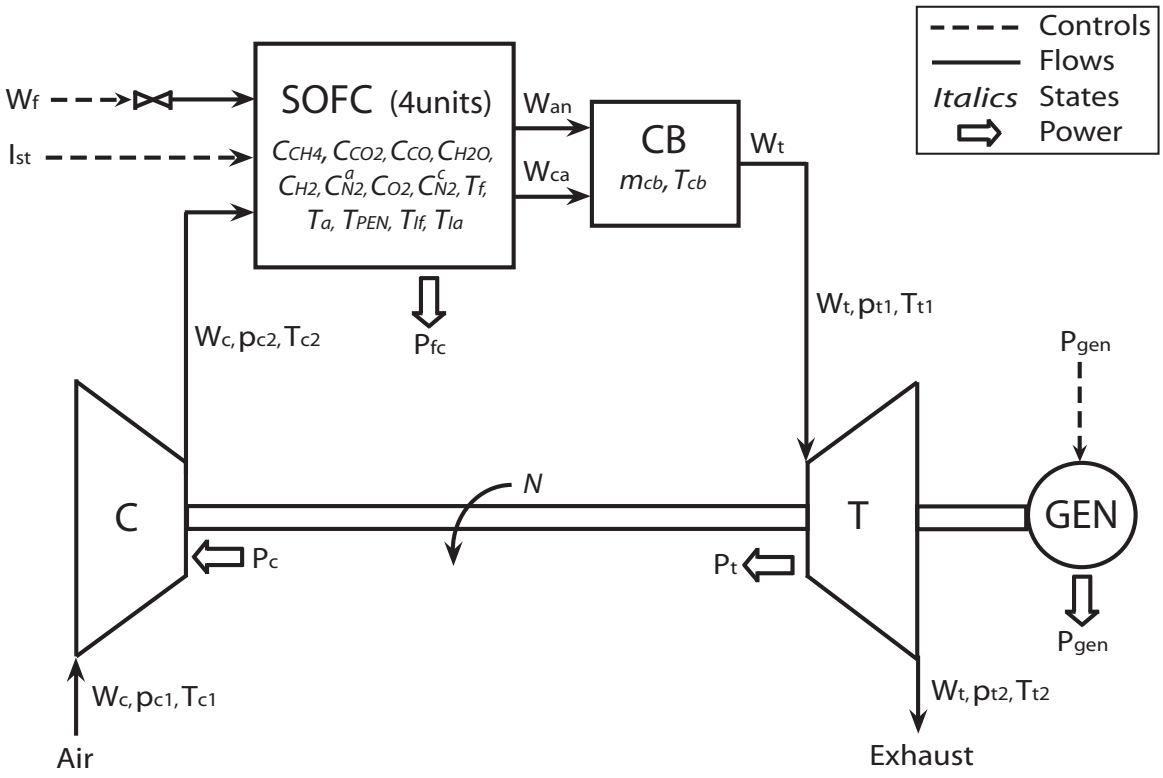

Figure 4.9: Hybrid SOFC/GT Schematic including inputs, controls, states and variables

CHAPTER 5

Steady State Optimization and Open Loop Analysis of a Hybrid Solid Oxide Fuel Cell and Gas Turbine System

In this chapter, results on steady state optimization, open loop analysis and model reduction will be delineated. In order to achieve maximum system efficiency, model-based optimization is performed using the gradient algorithm to determine the setpoints for the fuel flow, the generator load and the SOFC current. Feedforward control, which utilizes the actuator setpoints obtained from the optimization for each load point, is developed and the resulting system responses are analyzed. The analysis reveals that load transitions using feedforward control configuration is not possible for the highly integrated SOFC and GT system. System shutdown is observed when a large load step is applied. This phenomenon is attributed to the shaft rotational dynamics and the rapid increase in generator load. In Ch. 6, in order to avoid shutdown during load transition, a reference governor controller is developed and applied to the hybrid SOFC/GT system in order to filter the generator command. Finally, a proportional controller is used to regulate the fuel flow directly in the catalytic burner in order to allow for faster load transitions.

5.1 Steady State Optimization

The hybrid SOFC/GT system involves multiple actuators and inputs whose setting will dictate the system operation safety and efficiency. In this section, three inputs: the fuel flow supply, the current drawn from the SOFC and the load applied to the generator, are considered. For a given fuel flow, there are infinitely many combinations of currents drawn from the SOFC and loads applied to the generator that yield different net powers. Note that the net power produced, P_{net}, of the system is defined as the sum of the power output of the fuel cell P_{fc} and the power output of the generator P_{gen}:

$$P_{net} = P_{fc} + P_{gen}. \tag{5.1}$$

In order to determine the maximum steady state net power output for a given fuel flow the following optimization problem is solved using the Simulink model and the gradient optimization algorithm:

$$\max_{I_{st},P_{gen}} \ (P_{net}) \ \text{ for a given } W_f. \tag{5.2}$$

Note that this problem is equivalent to

$$\max_{I_{st},P_{gen}} \ \left(\eta_{SOFC/GT}\right) \ \text{ for a given } W_f, \tag{5.3}$$

where $\eta_{SOFC/GT}$ is the efficiency of the hybrid SOFC/GT system defined using the lower heating value of the fuel, Q_{LHV}, as:

$$\eta_{SOFC/GT} = \frac{P_{net}}{Q_{LHV} \cdot W_f}. \tag{5.4}$$

One can also show that (5.3) is equivalent to

$$\max_{I_{st},P_{gen},W_f} \ \left(\eta_{SOFC/GT}\right) \ \text{ for a given } P_{net}, \tag{5.5}$$

or

$$\min_{I_{st},P_{gen}} \ (W_f) \ \text{ for a given } P_{net}, \tag{5.6}$$

when optimization is performed over the entire range of net powers.

By repeating the optimization problem (5.2) for different fuel flows, the optimal steady state operation setpoints are obtained as shown in Fig. 5.1, which depicts the current density to be drawn from the SOFC unit[1], the required fuel flow and the power delivered by the generator as functions of the net power generated by the integrated system. The results can be used as static feedforward maps to schedule the actuators and power split to achieve maximum steady state efficiency for different power demands. This configuration is referred to in this work as the open loop control scheme.

When operating the hybrid system using the optimal input setting, the resulting fuel cell and generator power split ratio, P_{fc}/P_{net}; the fuel utilization, FU; and the cell voltage, V_{cell}, are shown in Fig. 5.2. The power split ratio is on average equal to 0.82, i.e., 82% of the net power is provided by the SOFC throughout the operational range. The fuel utilization in the SOFC defined as:

$$FU = \frac{\text{SOFC fuel consumption}}{W_f} \tag{5.7}$$

has a decreasing trend with respect to net power. Decreasing the fuel utilization implies that the pressure of fuel in the fuel cell increases, thus favoring the SOFC efficiency and

[1]Note that $I_{st} = A_c \cdot i$, where A_c is the cell area.

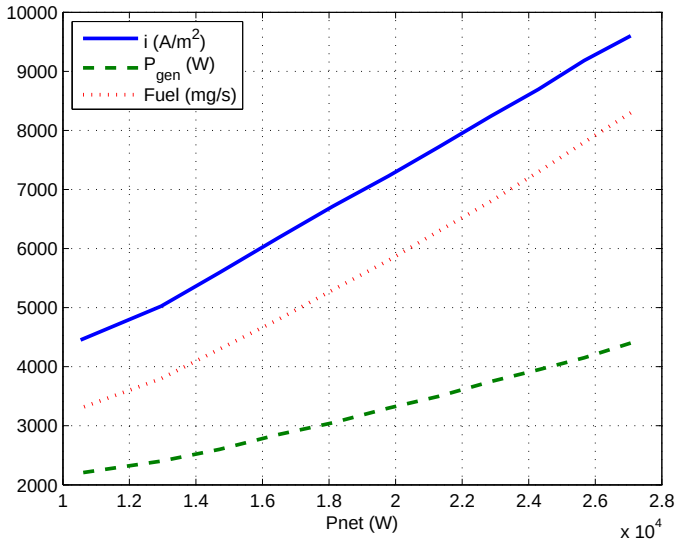

Figure 5.1: Steady State Optimal Setpoints (FF map) for current density (i), Fuel and generator load (P_{gen}) as a function of load

in turn the net power (through the voltage). Furthermore, with the decreasing of the fuel utilization in the SOFC, more fuel is burnt in the CB thus more energy is delivered to the turbine to support the compressor for air delivery. Finally, the increasing cell voltage with respect to the net power can be attributed to the decreased fuel utilization which, as mentioned above, leads to an increased fuel partial pressure in the SOFC.

Figure 5.3 shows the net power, P_{net}, and the fuel cell power, P_{fc}, as a function of SOFC fuel utilization (FU) and generator power, P_{gen}, for a constant fuel flow. Note that the algebraic relationship that couples the fuel utilization (FU), the current and the fuel flow can be expressed as:

$$W_f = \frac{I_{st} \cdot C_n \cdot M_f}{F \cdot FU(8x_{CH_4} + 2x_{CO} + 2x_{H_2})}, \tag{5.8}$$

where C_n is the number of cells, M_f is the molar weight of the fuel, F is Faraday's constant and $x_{(\cdot)}$ is the molar fraction of species $(\cdot)$ in a mole of fuel. It is noteworthy to see that again the optimal setpoint lies at the boundary of feasible operating points. Drawing more power than the optimal value by the generator for a given fuel flow will result in an infeasible operating point (i.e., P_{net}=0 kW). This is because the reduced power to the compressor will lead to reduced air in the SOFC, starting a vicious cycle for the hybrid system through the mechanical and thermal coupling that ends up in air starvation and system shut-down.

Another interesting observation from Fig. 5.3 is that when the generator power is reduced by an amount δP_{gen}, then there is a reduction in the net power more than δP_{gen}. From (5.1), this result implies that reducing the generator power also reduces the SOFC power.

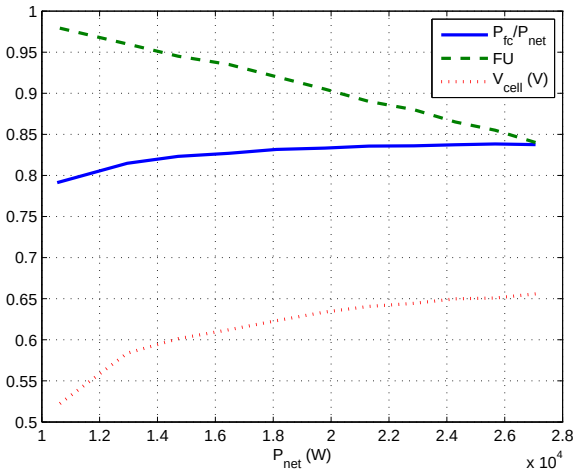

Figure 5.2: Steady State Optimal power ratio (P_{fc}/P_{net}), fuel utilization (FU) and voltage per cell

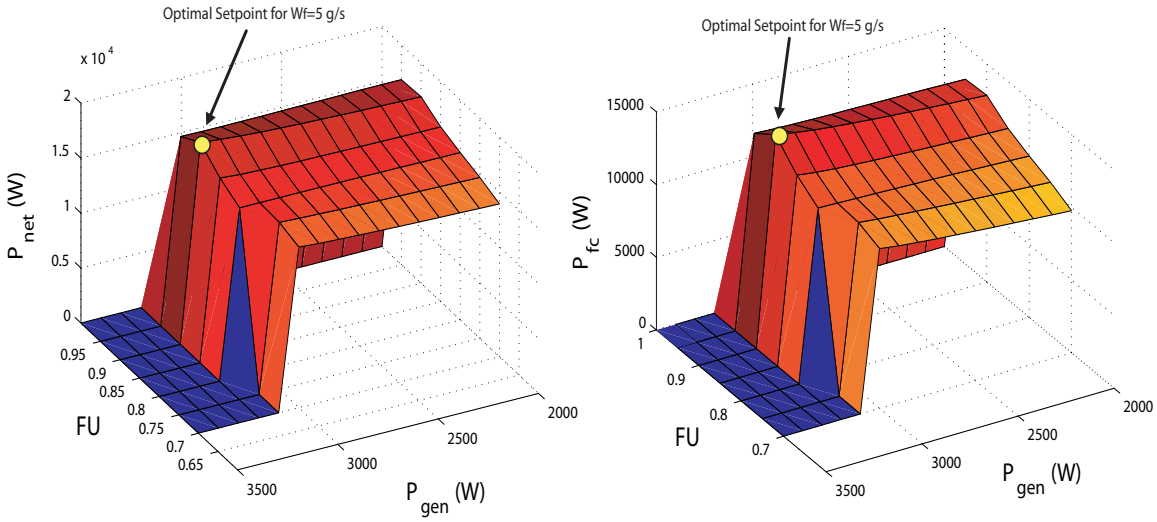

Figure 5.3: Net power map for fixed W_f=5g/s and variable Fuel Utilization (FU) and generator load (P_{gen})

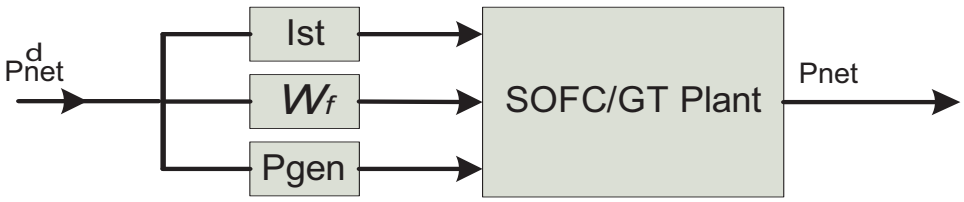

Figure 5.4: Open loop feedforward control for hybrid SOFC/GT system

Reducing P_{gen} from the optimal (maximum) setpoint implies more power will be delivered to the compressor, thereby sending more air to the SOFC which cools it down and results in reduced SOFC power output.

5.2 Open Loop Analysis

5.2.1 Open Loop Response

Without any feedback control in place, we consider the open loop response when a demanded load power step, from P^d_{net}=20 kW to P^d_{net}=25 kW, is applied. The open loop system configuration is shown in Fig. 5.4, where the input is the desired net power P^d_{net} and the output is the produced net power P_{net}. The optimal input settings, identified from the optimization, are used to change the fuel flow, the current, and the generator power from 5.8 to 7.6g/s, 7296 to 8946 A/m^2 and 3.30 to 4.05 kW, respectively, synchronized with the change in power demand. It is observed that the system shuts down in about 20 seconds after the steps are applied. For a smaller step though, from 20 to 20.5 kW, the shaft is able to support the applied load and the system reaches the desired net power after 31 s. During the 20 to 25 kW step, the large increase (step) in the generator load deprives the compressor from having enough power to supply the air during the transient to support the SOFC operation, causing the turbine shaft to stall and eventually the system to shut down. Therefore, open loop feedforward scheduling without load rate limiting or load filtering is not an option for rapid load following.

In order to understand the dynamics that cause the shutdown during the load transient, we consider the response when the steps in W_f, I_{st} and P_{gen} are applied separately. Figure 5.5, shows the P_{net} response when (a) all three actuators are stepped up from their optimum values corresponding to $P^d_{net} = 20\ kW$ to their optimum values corresponding to $P^d_{net} = 25\ kW$ and (b) when only I_{st} and W_f are stepped up from their optimum values corresponding to $P^d_{net} = 20\ kW$ to their optimum values corresponding to $P^d_{net} = 25\ kW$ while P_{gen} is constant at its optimum value corresponding to $P^d_{net} = 20\ kW$. Note that shutdown occurs only in case (a).

The response to a net power step down from 20 to 18 kW, is shown in Fig. 5.6. During a net power step down, due to the rapid reduction of the generator load, there is a significant

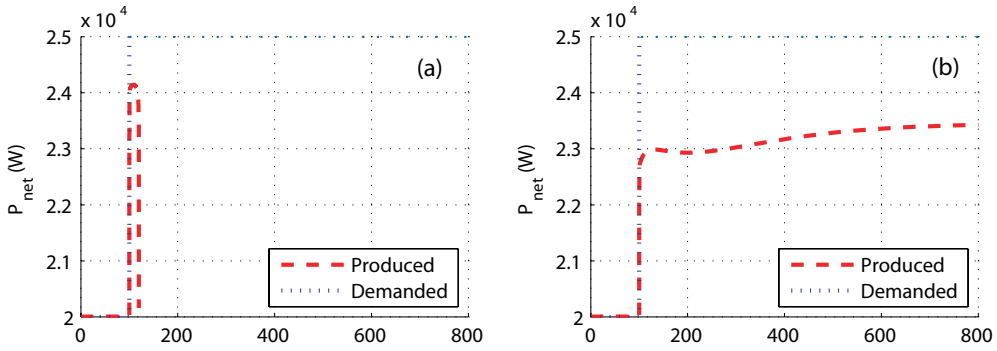

Figure 5.5: Load step response when (a) stepping up W_f, I_{st} and P_{gen} and (b) stepping up only W_f and I_{st}

overshoot in air supply to the SOFC. This causes a smooth reduction of the SOFC temperature. However due to the large SOFC thermal inertial, this temperature transient happens gradually and smoothly. Thus, no transient issues for load shedding can be identified.

5.2.2 Transient Response with Rate Limiter

Given that a rapid increase in the generator load was shown to be the main cause of system shutdown, an intuitive solution is to add a rate limiter to slow down the application of P_{gen}. Multiple rate limits are examined, varying from 3.3 to 6.7 W/s. From Fig. 5.7, one can see that the system shutdown is avoided, however, the net power response will depend on the rate limit.

To understand the response shown in Fig. 5.7, we refer to (5.1). As noted at the end of Sec. 5.1, if P_{gen} is decreased the SOFC power decreases as well. Thus, the net power is reduced directly through P_{gen} and indirectly through P_{fc}, when the generator power is reduced:

$$P_{net} = P_{fc}(P_{gen}) + P_{gen}. \tag{5.9}$$

The generator power affects the SOFC power via the GT coupling. Varying P_{gen} will affect air supply to the SOFC and in turn the SOFC temperature. Lower P_{gen} corresponds to higher shaft speed and more air cooling of the SOFC. The power of the SOFC, in turn, decreases with temperature (the rate of internal reforming reactions is decreased at lower temperatures).

Overall, if P_{gen} is not maximized at each time step, then the net power is lower and the load following performance is compromised. With this open loop configuration the fastest rate limiter on P_{gen} that will not cause shutdown for a 20 to 21 kW step is 6.5 W/s. This rate limit results in a P_{net} settling time of 168 s. Note that a constant rate limiter optimized for a given step will be suboptimal for smaller steps but insufficient to prevent shutdown for larger steps. In the next chapter, a more elaborate feedback control scheme is proposed

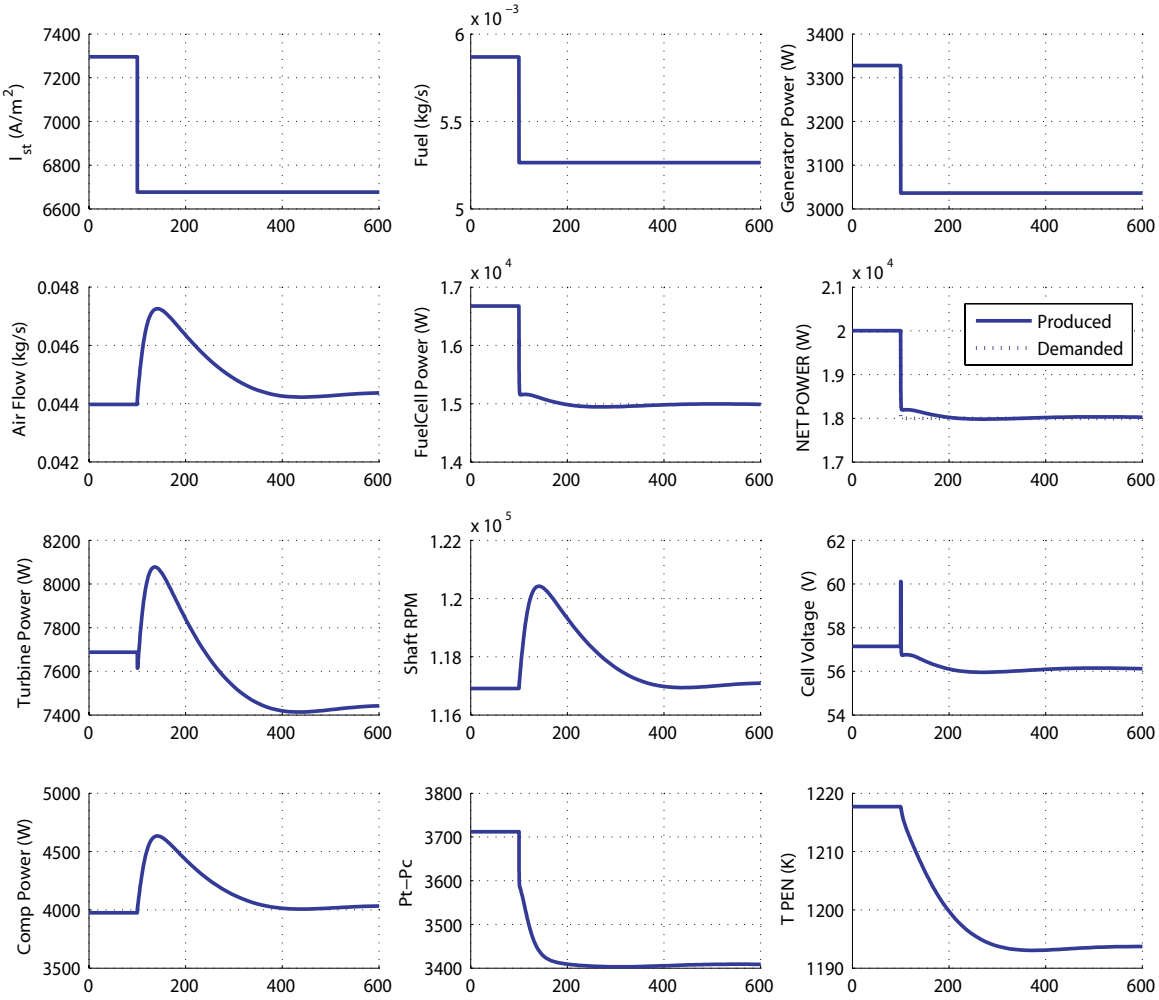

Figure 5.6: Load step response from 20 to 18 kW

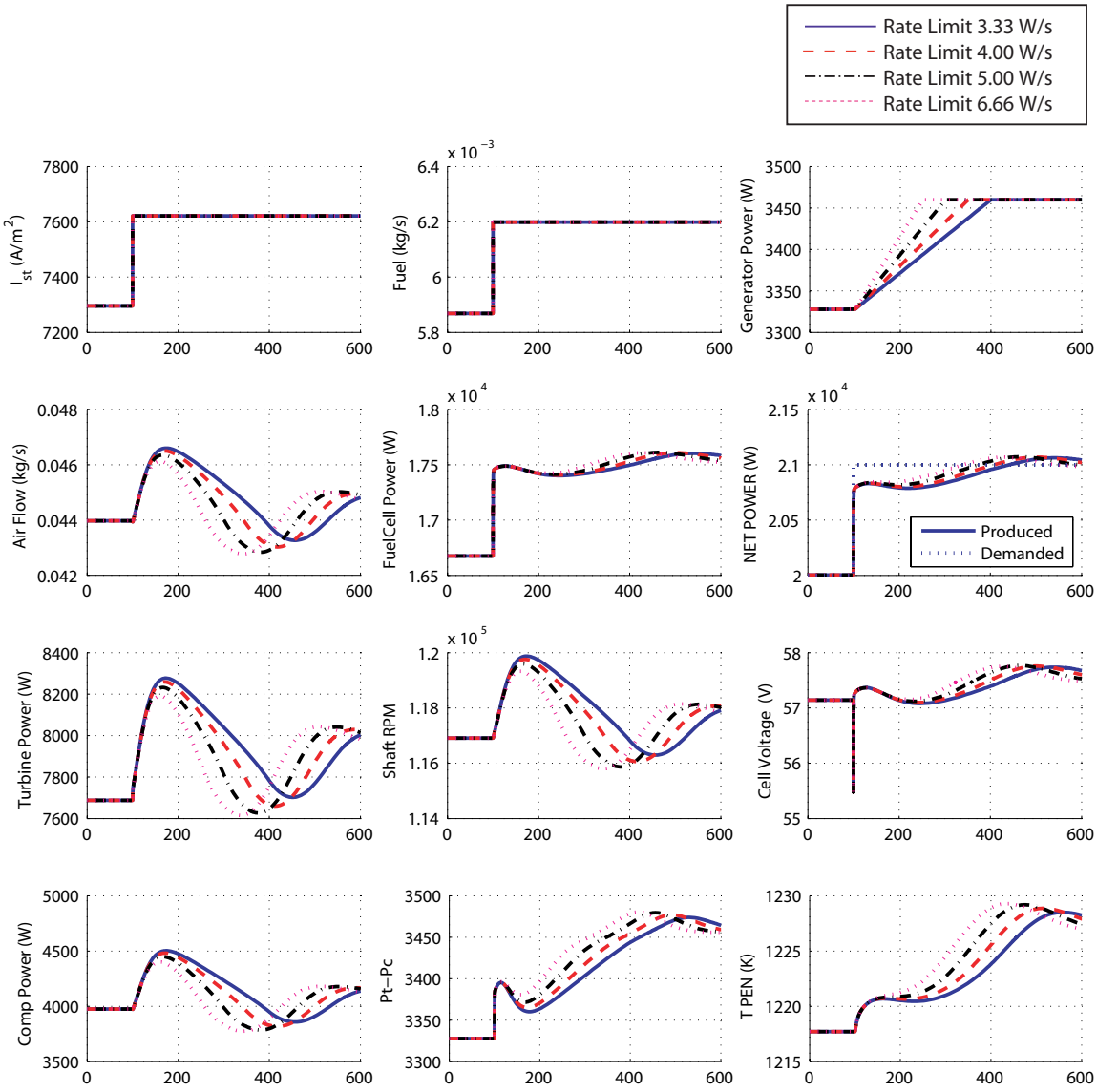

Figure 5.7: Step response from 20 to 21 kW with various rate limiters on P_{gen}

	T_{pen}			P_{net}			P_{tc}		
	O/U	DC	NMP	O/U	DC	NMP	O/U	DC	NMP
W_f	U	-	yes	O	+	no	O	0	
I_{st}	O	+	yes	U	-	yes	O/U	0	

	U_{cell}			W_c			N		
	O/U	DC	NMP	O/U	DC	NMP	O/U	DC	NMP
W_f	O	+	no	O	+	no	O	+	no
I_{st}	U	-	no	O/U	+	yes	O/U	+	yes

Table 5.1: Actuator authority table indicating overshoot (O), undershoot (U), positive or negative DC gain and non-minimum phase behavior.

that guarantees stable operation for any load step.

5.2.3 Actuator Authority Evaluation

In order to gain insights on the system's operation and understand the interactions between actuators and various system parameters, we proceed in presenting and analyzing the time and frequency response of various parameters to actuator signal variations. In the sequel, the actuator authority is evaluated with respect to its effects on the PEN temperature, net power P_{net}, shaft speed N, compressor air flow W_c, voltage U_c, as well the quantity $P_{tc} = P_t - P_c$ [2]. The Bode plots and the 1% step responses from the actuators to the parameters mentioned above are shown in Fig. 5.8-5.18. The linearization was performed at the equilibrium with setpoints corresponding to desired net power of 20 kW. Note that for the time responses shown, a separate step change in P_{gen} is not possible since the generator power is maximized for each W_f setpoint and any attempt to increase P_{gen} would result in system shutdown.

The characteristics of the responses of different variables with respect to the actuators are summarized in Table 5.1. This table indicates whether the response of a variable exhibits overshoot (O) and/or undershoot (U) during a 1% step increase in the corresponding actuator, whether the DC gain of the linear system is positive or negative and finally, whether the transfer function has a non-minimum phase (NMP) zero. Those characteristic are explained below and the main conclusions are presented. Note that the effects of the actuators on the voltage, the air flow and the rotational speed can be inferred via the effects of the actuators on the PEN temperature, the net power and P_{tc}.

[2]The quantity P_{tc} is shown later in this work to be a critical parameter in analyzing the shutdown phenomenon.

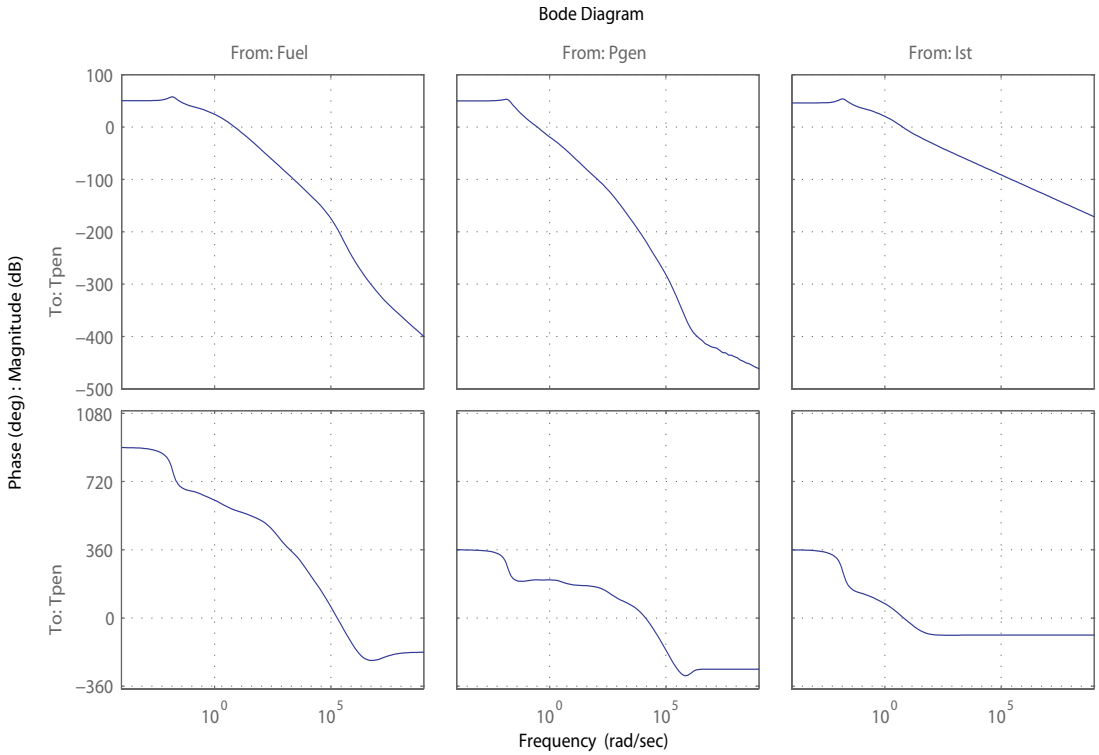

Figure 5.8: Bode Plots from (W_f, I_{st}, P_{gen}) to T_{pen}

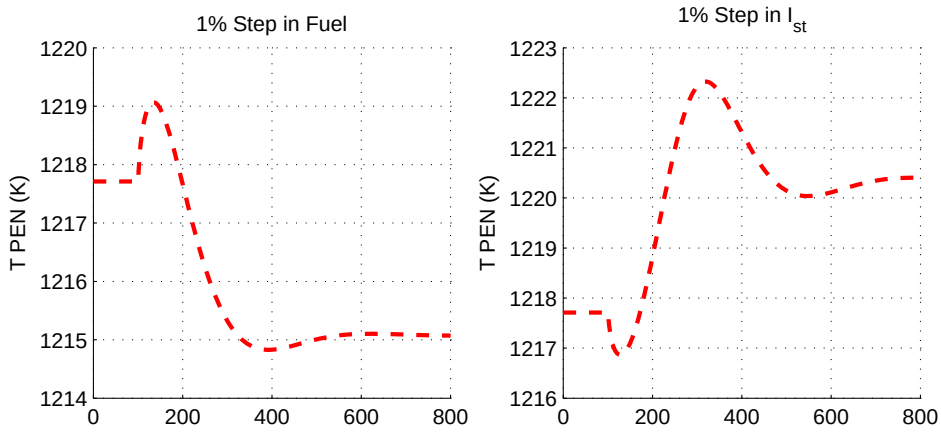

Figure 5.9: T_{pen} time response during a 1% step in W_f and I_{st} starting from the setpoints corresponding to 20 kW

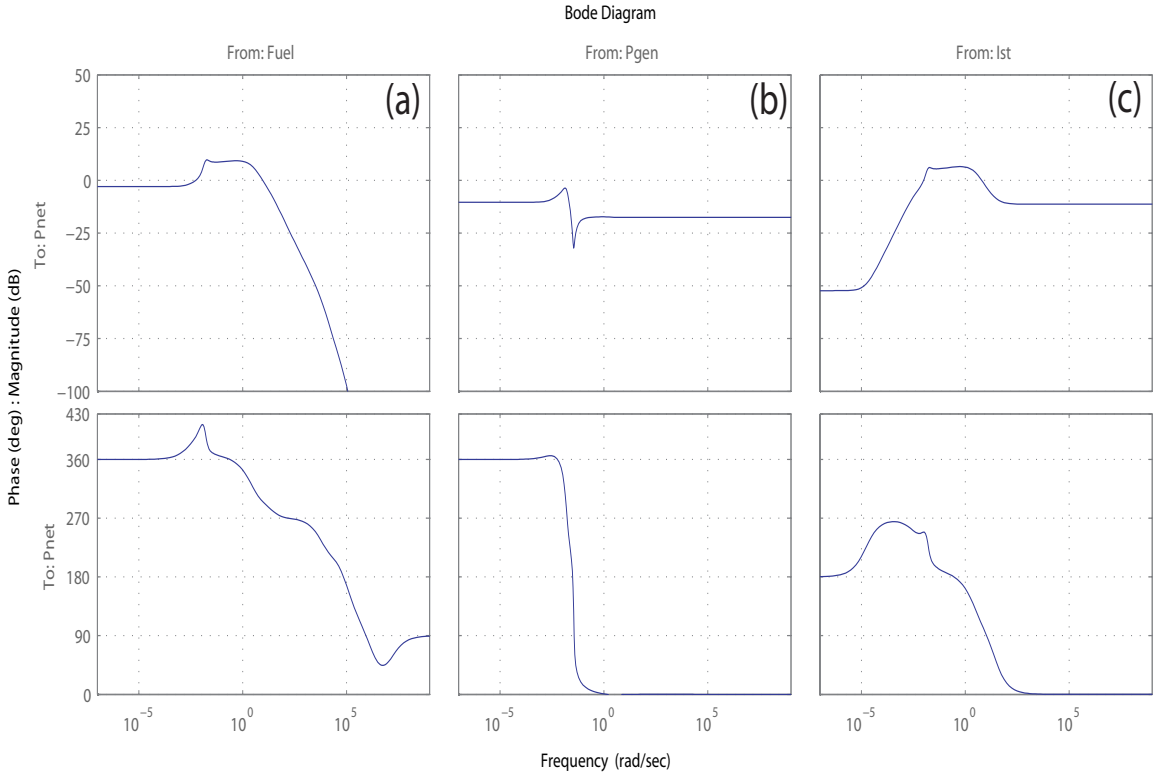

Figure 5.10: Bode Plots from (W_f, I_{st}, P_{gen}) to P_{net}

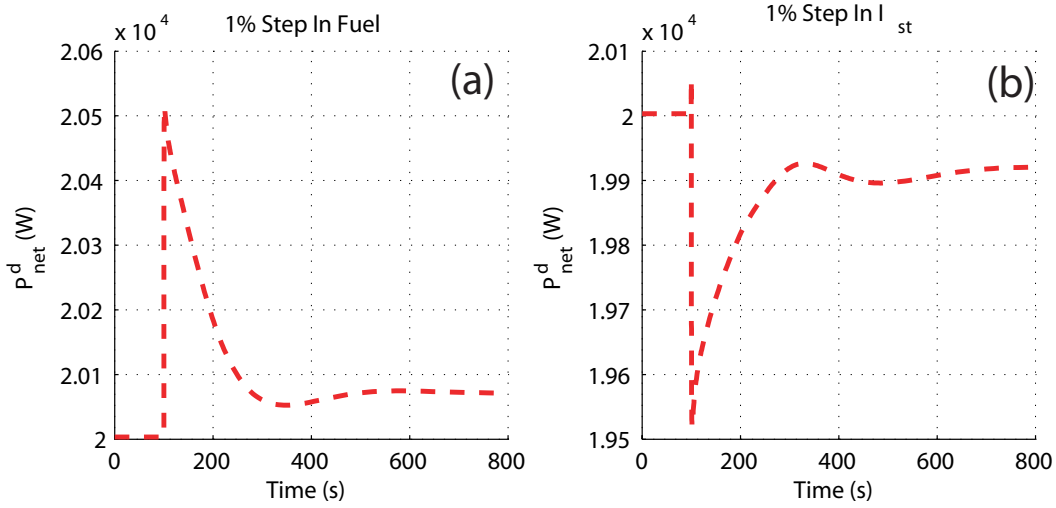

Figure 5.11: P_{net} time response during a 1% step in W_f and I_{st} starting from the setpoints corresponding to 20 kW

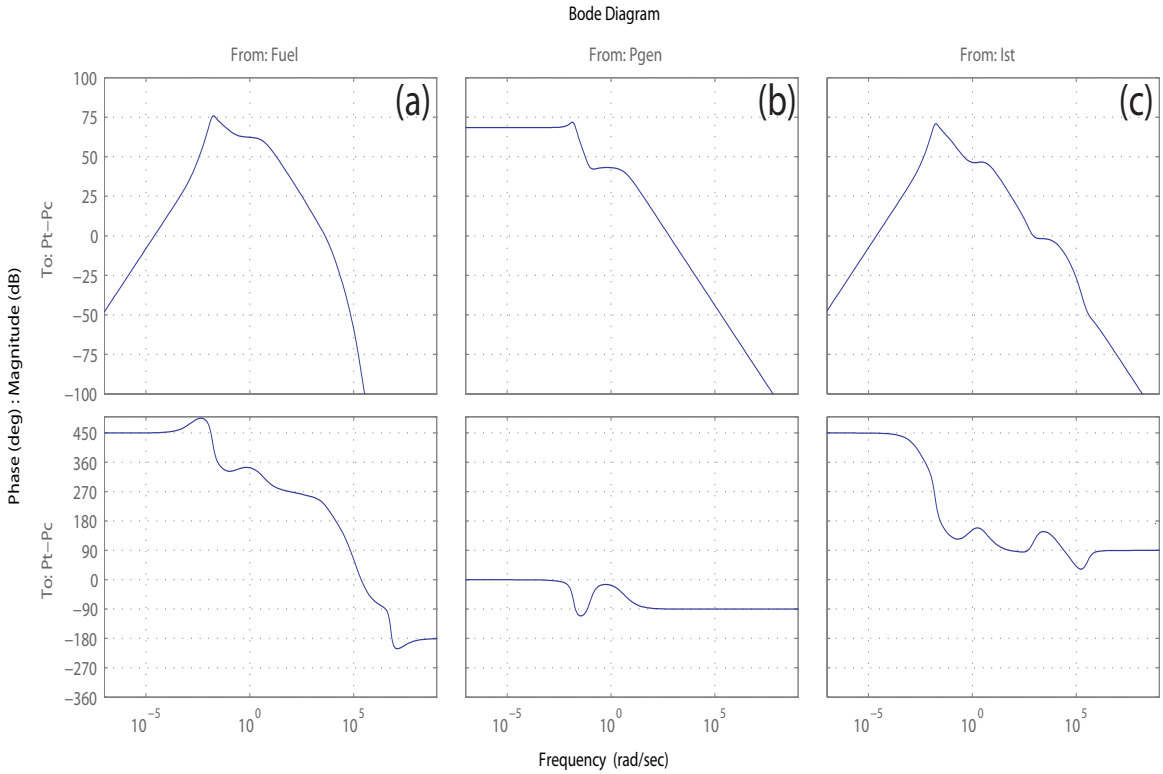

Figure 5.12: Bode Plots from $(W_f,\ I_{st},\ P_{gen})$ to $P_t - P_c$

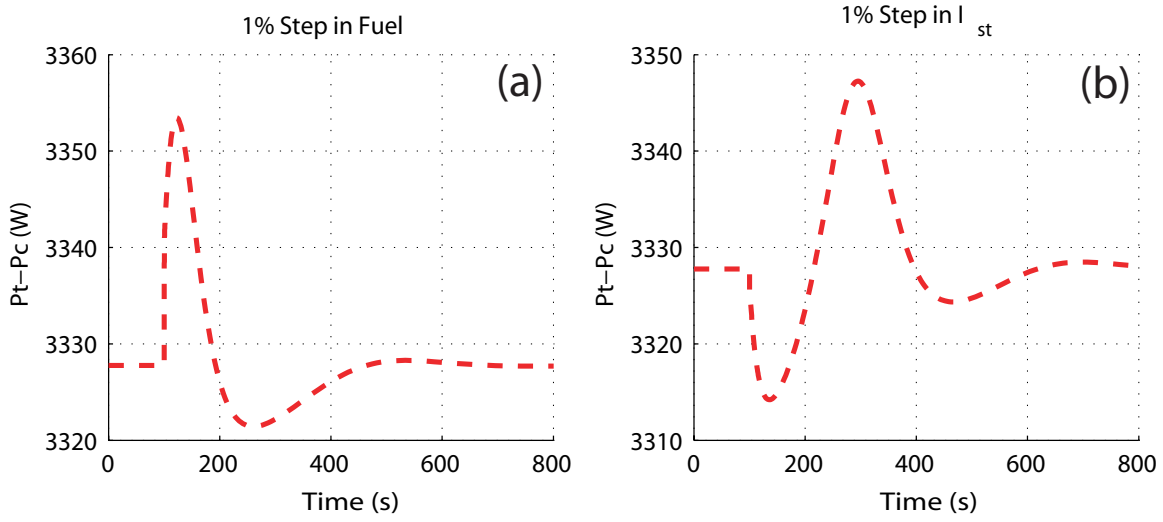

Figure 5.13: $P_t - P_c$ time response during a 1% step in W_f and I_{st} starting from the setpoints corresponding to 20 kW

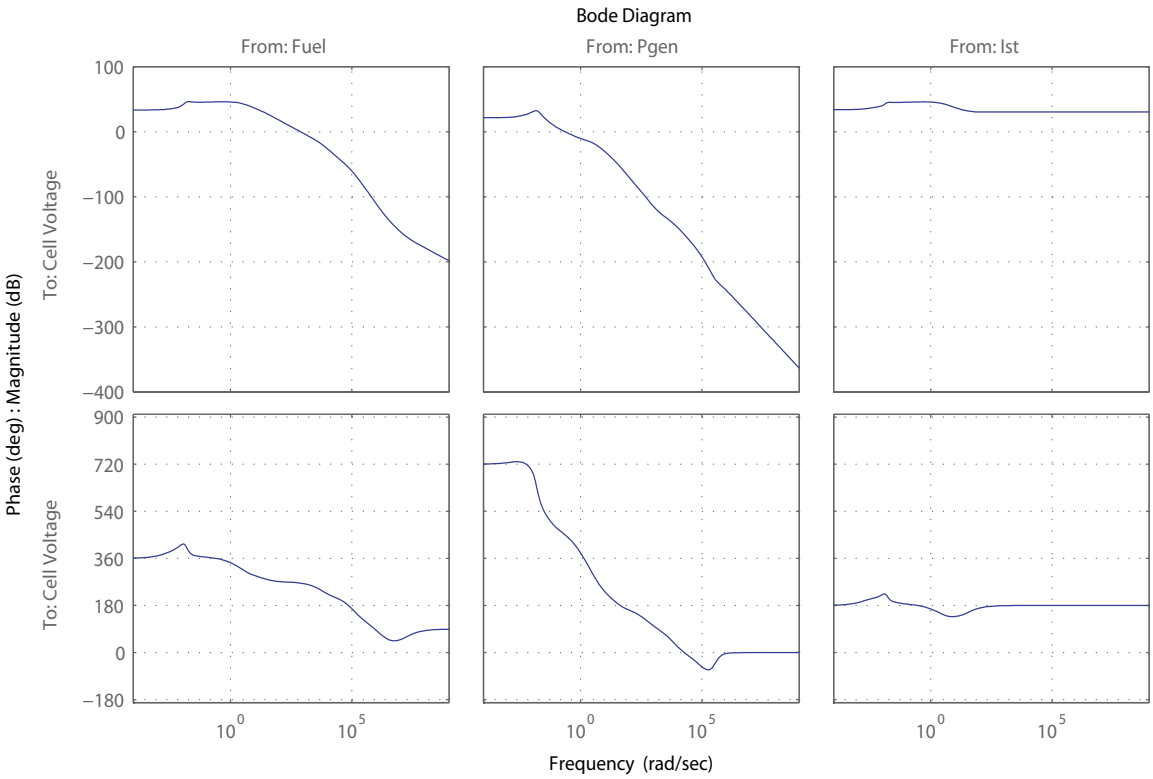

Figure 5.14: Bode Plots from (W_f, I_{st}, P_{gen}) to cell voltage

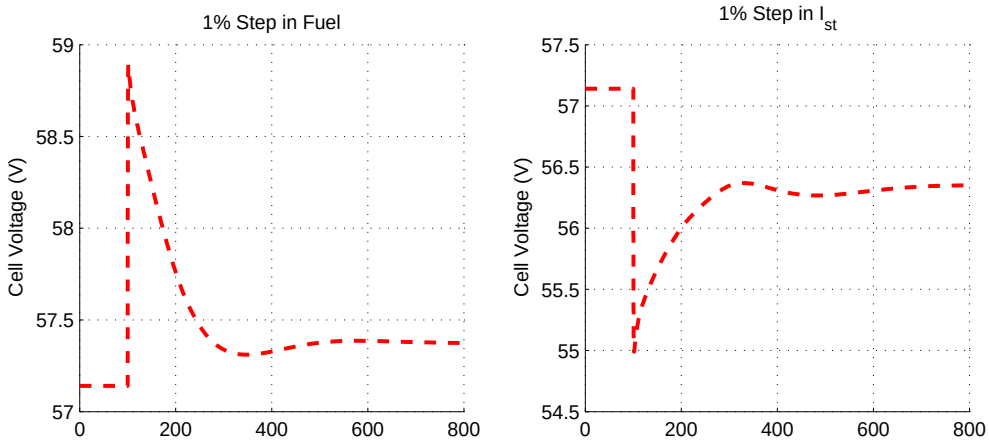

Figure 5.15: Voltage time response during a 1% step in W_f and I_{st} starting from the setpoints corresponding to 20 kW

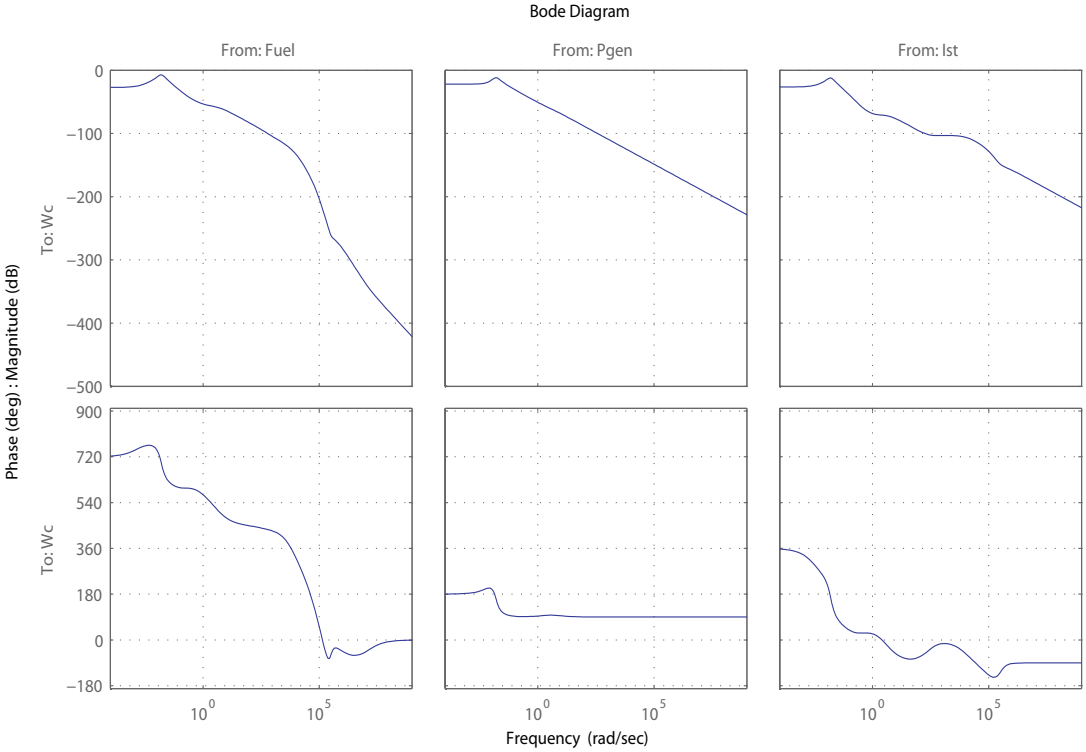

Figure 5.16: Bode Plots from (W_f, I_{st}, P_{gen}) to W_c

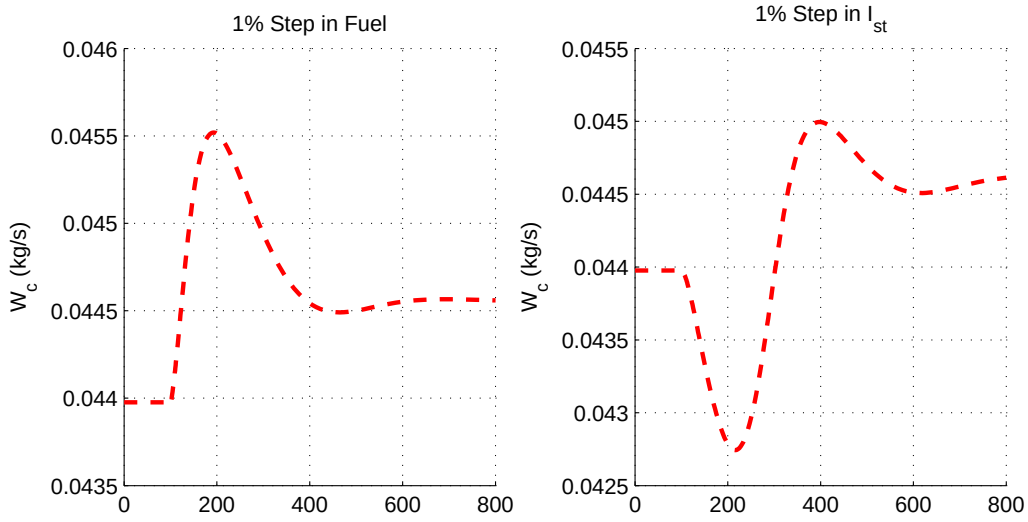

Figure 5.17: W_c time response during a 1% step in W_f and I_{st} starting from the setpoints corresponding to 20 kW

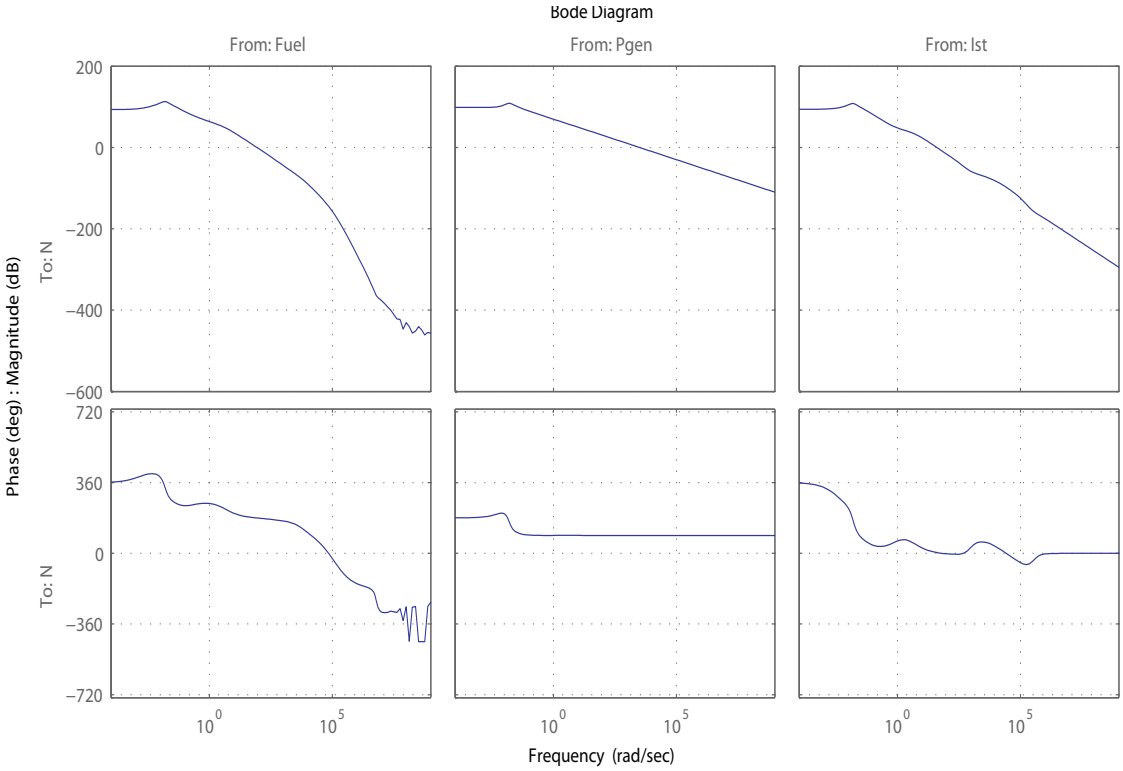

Figure 5.18: Bode Plots from (W_f, I_{st}, P_{gen}) to N

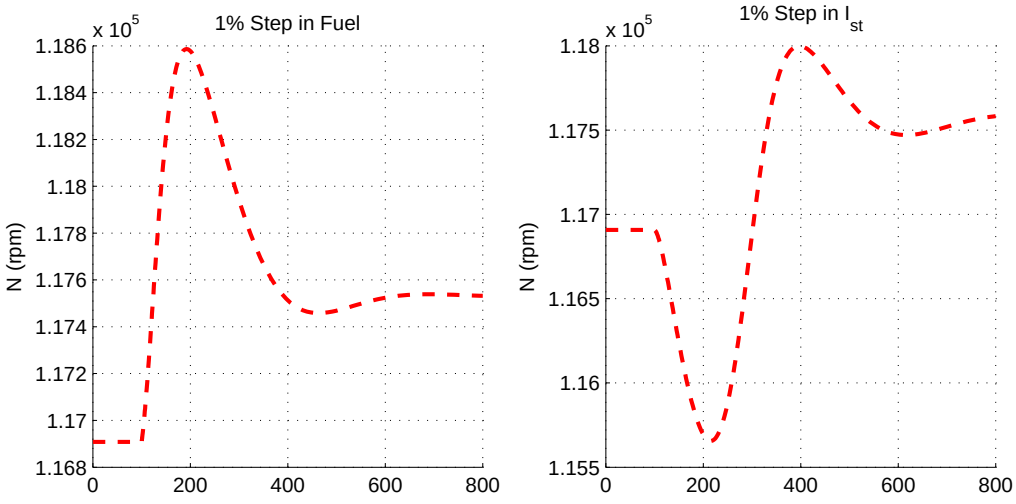

Figure 5.19: N time response during a 1% step in W_f and I_{st} starting from the setpoints corresponding to 20 kW

Actuator Authority on T_{pen}

A step increase in fuel flow causes initially an overshoot in the CB temperature since more fuel enters the CB. Due to the GT coupling though, higher temperature corresponds to higher rotational speed on the shaft. In turn, higher speed allows for more air into the SOFC which at lower frequencies (towards steady state operation) cools down the SOFC. Increasing the generator load causes a decrease in the shaft rotational speed and thus the PEN temperature is increased (less air flow into the SOFC). Finally, a step up in current drawn from the SOFC initially decreases the PEN temperature since fuel is depleted instantaneously (i.e., due to less heat from internal reforming reactions). Towards lower frequencies, less fuel corresponds to less turbine power and less air flow to the SOFC and thus the temperature increases.

Actuator Authority on P_{net}

A step increase in W_f causes a rapid overshoot in the SOFC voltage due to fuel pressure increase and in turn to the P_{net}. At steady state, increased W_f delivers higher P_{net} since the partial pressure of fuel is higher. A step increase in I_{st} causes an undershoot in voltage since the fuel is depleted instantaneously. At steady state, an increase in current results in decreasing the operating voltage. An increase in P_{gen} will cause the same increase in P_{net} (since $P_{net} = P_{fc} + P_{gen}$) at high frequencies. At steady state (since P_{fc} is also a function of P_{gen}) the fuel cell power will increase. The increase in P_{gen} decreases air supply to the SOFC and causes higher temperature. Higher SOFC temperature corresponds to higher SOFC power output.

Actuator Authority on $P_{tc} = P_t - P_c$

A step increase in W_f causes a rapid overshoot in P_{tc} due to the fast pressure (i.e., flow) dynamics which in turn cause a rapid overshoot in the turbine power. At steady state, P_{tc} is equal to its previous steady state value since P_{gen} is constant. A step increase in I_{st} will cause a significant undershoot in P_{tc} due to the fuel consumption increase and lower turbine inlet temperature. Thus, if a rapid increase in P_{tc} is desired, the fuel is a more suitable actuator. This result will be used in Ch. 6 to develop a control scheme that improves the transient response.

5.2.4 Shutdown Trajectory Characterization

In this section, more detailed analysis reveals that the shutdown is initiated by the gas turbine and specifically the shaft dynamics. The rotational speed of the shaft N, and thus the air flow to the SOFC, is a function of the power balance on the shaft. The rotational

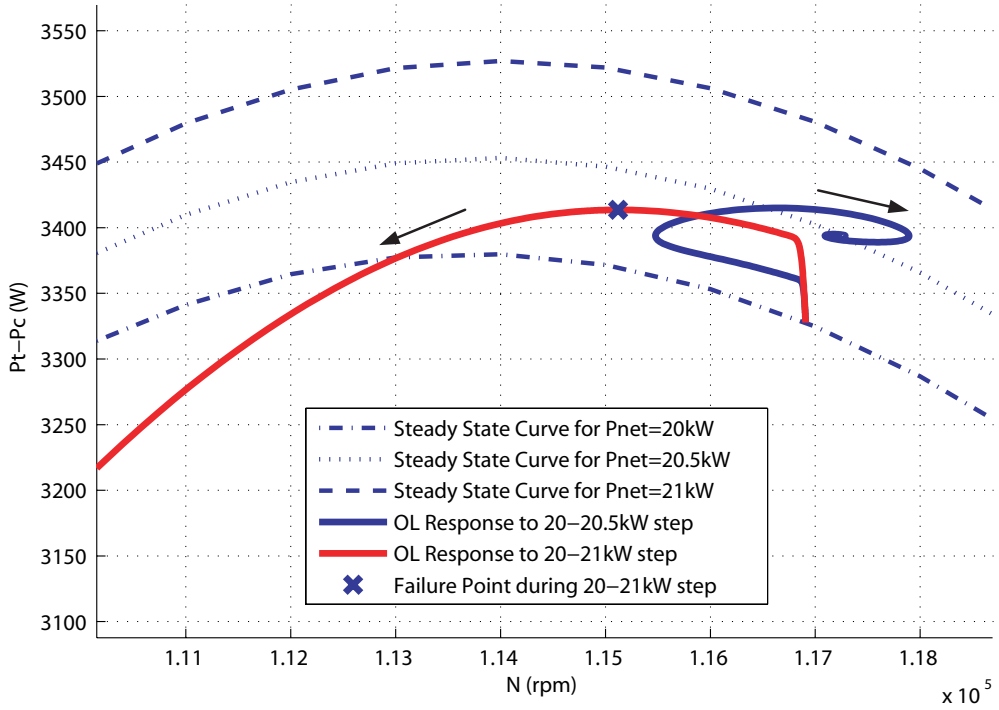

Figure 5.20: System response during a 20-20.5 kW and 20-21 kW step in a $P_t - P_c$ vs N plot

dynamics are governed by the equation:

$$\frac{dN}{dt} = \frac{P_t - P_c - P_{gen}}{\alpha \cdot N \cdot J} = \frac{P_{tc} - P_{gen}}{\alpha \cdot N \cdot J} \tag{5.10}$$

where the acceleration dN/dt is a function of the turbine power P_t minus the compressor power P_c and the generator power P_{gen} over the speed N and the shaft inertia J. A large load step corresponds to a large P_{gen} step, causing the speed to drop ($dN/dt < 0$). Figure 5.20 shows the trajectories on the $(P_t - P_c, N)$ plane for the responses to a step in P_{net}^d from 20 to 20.5 kW and from 20 to 21 kW. For the latter step, it can be seen that the trajectory will slide towards the lower left corner of the $(P_t - P_c, N)$ plane until the system shuts down, namely $N = 0$.

Given that the use of the full-order model for analytic investigation of the shutdown phenomenon is prohibitive due to its complexity, we attempt to develop an equivalent 2-state model to capture the effects of P_{gen} on the shaft rotational speed. The equivalent schematic of the SOFC/GT plant given in Fig. 5.21, where the shaft dynamics are separated from the SOFC, C and T models. To capture the effects of the P_{gen} input, we ignore the effects of W_f, I_{st} for the moment and approximate the dynamics from N to P_{tc} with simple first-order dynamics $1/(\tau s + 1)$. We know that at steady state, as shown in Fig. 5.20, the

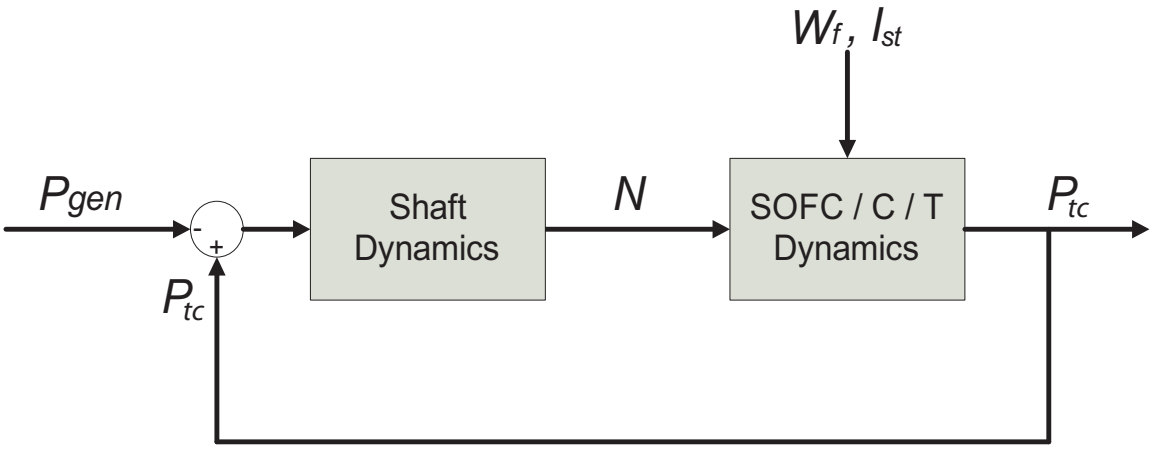

Figure 5.21: Equivalent schematic of SOFC/GT system with Shaft dynamics separated

relationship between N and P_{tc} can be approximated by a second-order polynomial of the form:

$$P_{tc} = aN^2 + bN + c, \tag{5.11}$$

with $a < 0$. Multiplying the right hand side of the equation with the first-order dynamics, the dynamic relationship between N and P_{tc} can be expressed as

$$\dot{P_{tc}} = \frac{a}{\tau}N^2 + \frac{b}{\tau}N + \frac{c}{\tau} - \frac{1}{\tau}P_{tc}. \tag{5.12}$$

For a given set of inputs ($W_f,\ I_{st},\ P_{gen}$)=(6.2 $g/s,\ 7620\ A/m^2,\ 3558\ W$), the parameters in (5.12) can be identified from the full-order model as

$$(a, b, c, \tau) = (-5.1 \cdot 10^{-6},\ 1.17,\ -63520,\ 0.005).$$

Thus, the equivalent second-order system can be expressed as:

$$\begin{bmatrix} \dot{P_{tc}} \\ \dot{N} \end{bmatrix} = \begin{bmatrix} \frac{a}{\tau}N^2 + \frac{b}{\tau}N + \frac{c}{\tau} - \frac{1}{\tau}P_{tc} \\ (P_{tc} - P_{gen})/(\alpha \cdot N \cdot J) \end{bmatrix}. \tag{5.13}$$

The following theorem, utilizes this second-order system to show that if during an increase in P_{gen} the shaft speed drops below the point where $\frac{dP_{tc}}{dN} > 0$ before it reaches its desired setpoint, the system will not be able to recover. This condition can be useful in detecting the shutdown phenomenon and can be utilized in a control scheme as a constraint. In case the control scheme (for example a reference governor) utilizes model-based simulations to determine the generator load that will not cause shutdown, then this constraint can be used to indicate the onset of shutdown and thus reduce simulation time.

Theorem 5.1 Consider the system in (5.13) with states $x = [N,\ P_{tc}]^{\mathrm{T}}$ and input P_{gen}. When an input step increase from P_{gen1} to P_{gen2} is applied and the operating point $x(t)$ enters the following set:

$$Z = \left\{ (P_{tc}, N) | \dot{N} < 0,\ \dot{P}_{tc} < 0,\ P_{tc} < P_{tc,ss},\ N < N_{ss} \right\} \tag{5.14}$$

then

$$\lim_{t \to \infty} N = 0$$

where $P_{tc,ss}$ and N_{ss} are the equilibrium points with input P_{gen2}.

Proof: We want to show that if $x(t) \in Z$, then $x(t)$ is outside the region of attraction of the stable equilibrium. Note that the system has the following two equilibrium points:

$$(N, P_{tc})_{ss1} = \left(\frac{-b + \sqrt{b^2 - 4a(c - P_{gen})}}{2a}, P_{gen} \right) \tag{5.15}$$

$$(N, P_{tc})_{ss2} = \left(\frac{-b - \sqrt{b^2 - 4a(c - P_{gen})}}{2a}, P_{gen} \right) \tag{5.16}$$

$$\tag{5.17}$$

where $(N, P_{tc})_{ss1}$ is a stable and $(N, P_{tc})_{ss2}$ is an unstable equilibrium point.

We can consider the following Lyapunov function (i.e., the distance of the operating setpoint x from the equilibrium x_{ss}) :

$$V(x) = \frac{1}{2} \|x - x_{ss}\|_2 = \frac{1}{2} (P_{tc} - P_{tc\ ss})^2 + \frac{1}{2} (N - N_{ss})^2 \tag{5.18}$$

with

$$V(x) > 0,\ \forall\ x \neq x_{ss},\ V(x_{ss}) = 0,\ \|x\| \to \infty \Rightarrow V(x) \to \infty. \tag{5.19}$$

The derivative of V can be expressed as

$$\dot{V}(x) = \dot{P}_{tc}(P_{tc} - P_{tc\ ss}) + \dot{N}(N - N_{ss}). \tag{5.20}$$

For

$$x(t) \in Z\ \Rightarrow\ \dot{V}(x) > 0, \tag{5.21}$$

which implies that the distance between the operating point and the equilibrium is increasing and thus the trajectory is heading away from the equilibrium. The second step is to show that if

$$x(t_o) \in Z \;\Rightarrow\; x(t) \in Z \;\forall\; t \geq t_o. \tag{5.22}$$

This can be verified using the quadratic form of the nonlinearity in (5.12) and the phase portrait of the system, shown in Fig. 5.22. Thus, conditions (5.21) and (5.22) imply that all the points that belong in Z do not belong in the region of attraction of the stable equilibrium.

Physically this theorem says that unless the power into the shaft $(P_t - P_c)$ is increasing when the speed is decreasing, then the system has no way of stabilizing itself. If the speed is dropping and at the same time the energy powering the shaft is dropping, the speed will keep dropping until the system shuts down. This same analysis applies to the full-order model developed here, but since the dynamics of P_{tc} cannot be expressed analytically we utilized the equivalent second-order model.

Furthermore, note that the equilibrium points lie on the intersection of the following curves:

$$aN^2 + bN + c - P_{tc} = 0 \tag{5.23}$$

$$P_{tc} - P_{gen} = 0. \tag{5.24}$$

where (5.24) is noted in in Fig. 5.22 ($P_{tc} = 3558$ kW). It can be seen that (5.23) is a manifold that attracts both the stable and unstable trajectories. This is a direct result of the fact that the time constant τ for the P_{tc} dynamics is relatively faster than that for the N dynamics. Thus, the trajectory converges to the curve in the (P_{tc}, N) plane that satisfies (5.23).

Shaft Energy Balance

Following the analysis on the previous section, it can be seen that in order to keep the operating point within the region of attraction of a stable equilibrium, there are two possible solutions:

- Limit the shaft speed deceleration. This can be achieved by filtering the load applied to the generator such that the drop in shaft speed will not drive the trajectory to an unsafe region, or
- Guarantee that P_{gen} is supported by increasing P_{tc} during the transient. This can be accomplished by feeding extra fuel into the system during the transient.

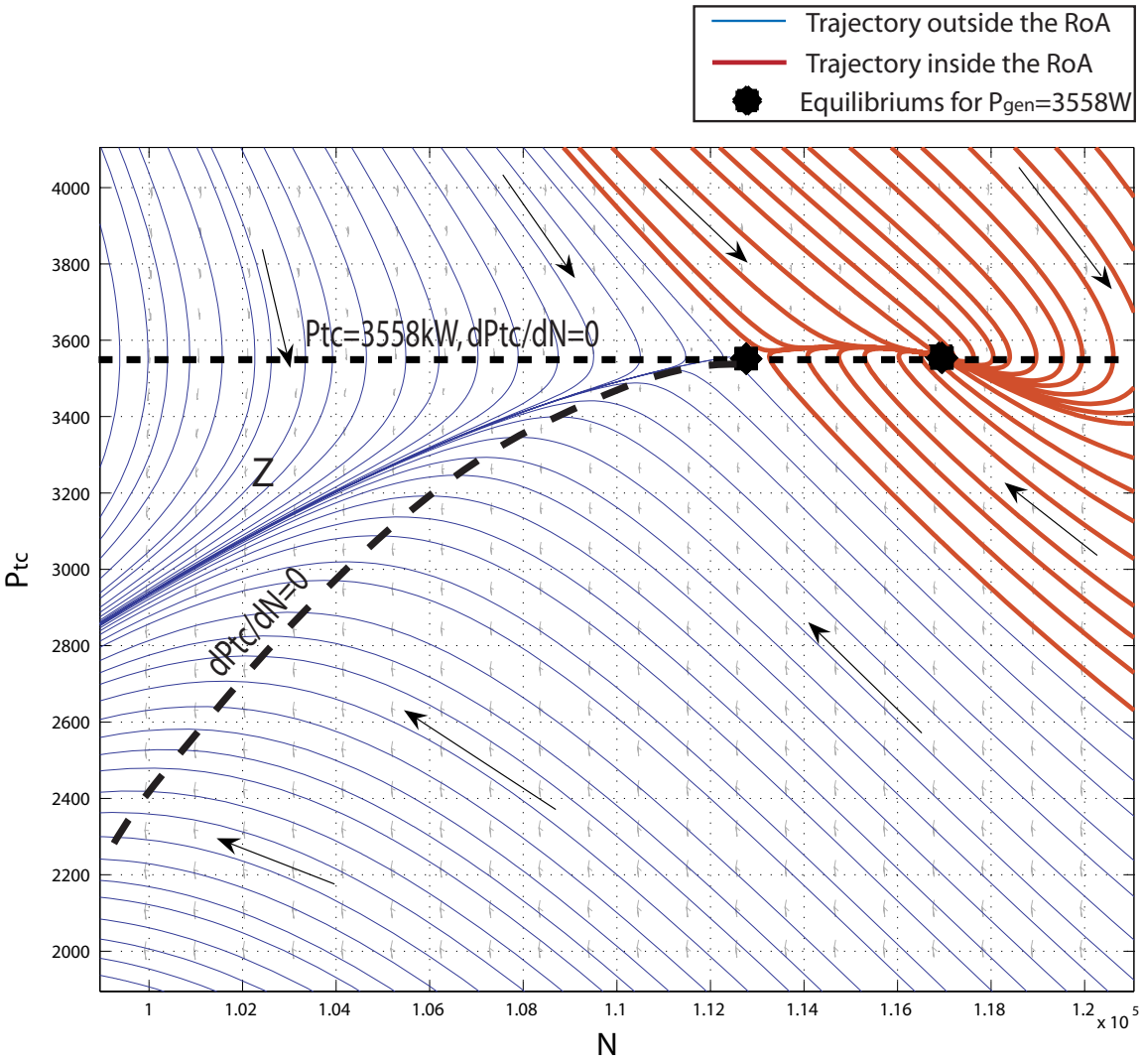

Figure 5.22: Phase portrait of simplified system with states P_{tc} and N

Another expression of the above solutions can be obtained by exploring the energy balance of the system. Integrating (5.10) yields:

$$\underbrace{\int (P_t - P_c)dt}_{E_{in}} - \underbrace{\int P_{gen}dt}_{E_{out}} = \frac{N^2(t) - N_o^2}{\alpha \cdot J}. \tag{5.25}$$

Note that the energy that we put into the shaft ($E_{in} = \int (P_t - P_c)dt$) minus the energy we draw from the shaft through the generator ($E_{out} = \int P_{gen}dt$) is a function of the initial and current rotational speed. Given the energy equation, the possible solutions to mitigate shutdown can be expressed as:

- Reduce E_{out} by filtering the generator load P_{gen} or
- Increase E_{in}, by adding extra fuel in the system during a transient to support the generator load.

These observations will be combined and implemented in the control scheme proposed in the next chapter. It will be shown that the proposed controller enhances both the stability by preventing shutdowns and the load following capabilities of the system.

5.3 Nonlinear Reduced-Order Model Development

The model shown in (5.13) captures only the effects of P_{gen} on the shaft dynamics. In order to gain further insights on the shutdown phenomenon and to identify the effects of all three actuators on the system shutdown dynamics, we proceed to develop a physics-based nonlinear reduced-order model with all three inputs included. First the states to be used for the reduced-order model are identified through linear analysis, including the use of linearization, balanced realization and truncation, followed by the development of the nonlinear reduced-order model and analysis on its dynamics.

5.3.1 Dominant States in SOFC/GT Model

Using linear analysis tools, it is shown that the important states in describing the transient system dynamics are the shaft speed, N, the CB temperature and CB mass. The nonlinear model expressed as

$$\dot{x} = f(x, u), \tag{5.26}$$

is linearized as:

$$\delta\dot{x} = A\delta x + B\delta u, \tag{5.27}$$

$$\delta y = C\delta x + D\delta u, \tag{5.28}$$

with

$$u = [P_{net}^d] \text{ and } y = [N]. \tag{5.29}$$

Note that the linearization was done at the P_{net}^d=20 kW equilibrium and includes the feedforward maps used for regulating I_{st}, W_f and P_{gen}. The linear plant is then normalized as

$$\delta\dot{x}_n = \underbrace{X_{ss}AX_{ss}^{-1}}_{A_n} \cdot \delta x_n + \underbrace{X_{ss}BU_{ss}^{-1}}_{B_n} \cdot \delta u \tag{5.30}$$

$$\delta y_n = \underbrace{Y_{ss}CX_{ss}^{-1}}_{C_n} \cdot \delta x_n + \underbrace{Y_{ss}DU_{ss}^{-1}}_{D_n} \cdot \delta u \tag{5.31}$$

where

$$\delta x_n = X_{ss}\delta x \tag{5.32}$$

$$\delta u_n = U_{ss}\delta u \tag{5.33}$$

$$\delta y_n = Y_{ss}\delta y \tag{5.34}$$

$$X_{ss} = diag\left(\frac{1}{x_{ss}^1}, ..., \frac{1}{x_{ss}^{55}}\right) \tag{5.35}$$

$$U_{ss} = 1/u_{ss} \tag{5.36}$$

$$Y_{ss} = 1/y_{ss}, \tag{5.37}$$

and x_{ss}^i for $i = 1, ..., 55$ are the steady state values of the states, $u_{ss} = 20\ kW$ and $y_{ss} = 116880 rpm$. Finally, a balanced realization is obtained from the normalized plant where each of the states is equally controllable and observable. Given that (A_n, B_n) is controllable, (A_n, C_n) is observable, A_n is stable and that W_c and W_o are the corresponding controllability and observability grammians, there exists a transformation matrix $\delta x_b = T_m \delta x_n$ such that:

$$\delta\dot{x}_b = T_m A_n T^{-1} \cdot \delta x_b + T_m B_n \cdot \delta u \tag{5.38}$$

$$\delta y_b = C_n \cdot T_m^{-1}\delta x_b + D_n T_m^{-1}\delta u \tag{5.39}$$

$$\bar{W}_c = T_m W_c T_m^{\mathrm{T}} \tag{5.40}$$

$$\bar{W}_o = T_m^{\mathrm{T}} W_o T_m^{-1} \tag{5.41}$$

with

$$\bar{W}_c = \bar{W}_o = diag([\sigma_1\ \sigma_2\ ...\ \sigma_n]), \tag{5.42}$$

where σ_i are the Hankel singular values. Thus, if $\sigma_i \gg 1$ then x_{bi} is strongly controllable and observable and if $\sigma_i \ll 1$ then x_{bi} is weakly controllable and observable [18]. A plot of

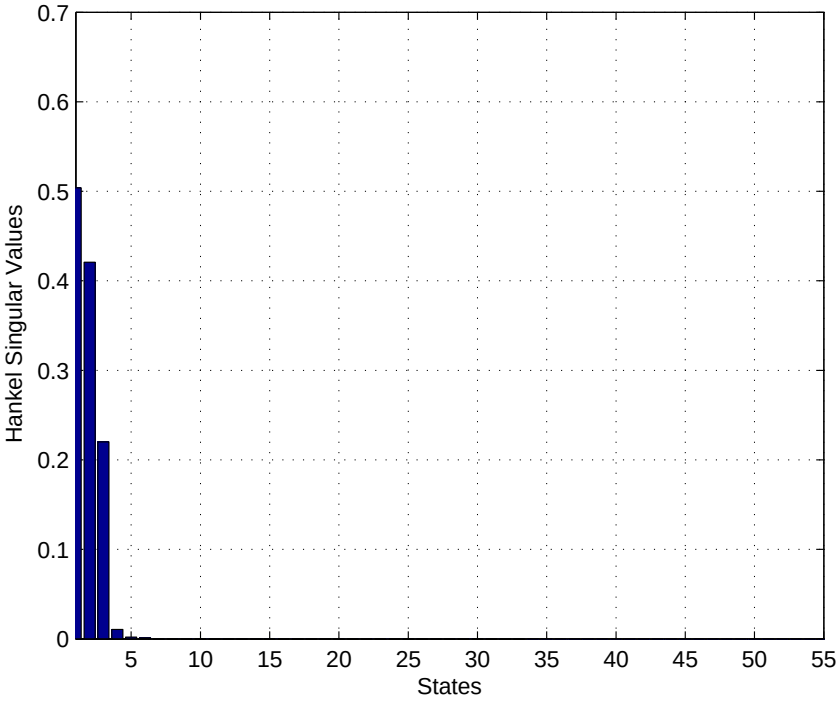

Figure 5.23: Hankel Singular Values for the states of the linearized, normalized and balanced realization model

the Hankel singular values for all 55 states is given in Fig. 5.23. It can be seen that only 3 are the important states in the balanced realization model. In addition, by inspecting the transformation matrix gains (TMG), we can obtain the dependency of these three states of the Balanced Realization Plant (BRP) to the original states. The four maximum gains in the first three rows of the transformation matrix are given in Table 5.2. The three dominant states are predominantly related to the CB temperature, CB mass and rotational speed of the GT shaft.

This result can also be explained physically since the rotational speed is a function of the power balance on the shaft and as such the turbine power is directly related to the CB temperature and mass flow. While the linear analysis helps in identifying the dominant states, the linear model however does not capture the inherently nonlinear relation between N and P_{tc} and consequently the linear model does not capture the shutdown phenomenon. In the sequel, the development of a nonlinear reduced-order model (ROM) that can capture the shutdown dynamics and the interaction between all three actuators and the shaft speed is presented.

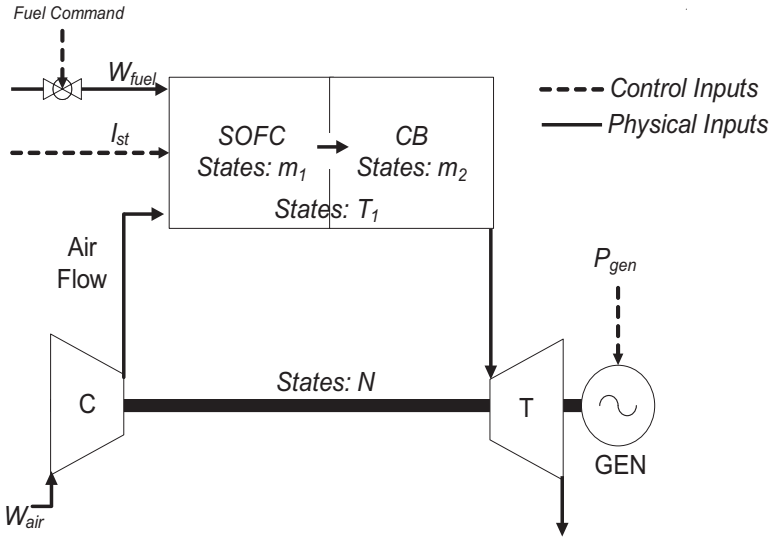

Figure 5.24: Reduced-Order Model Schematic

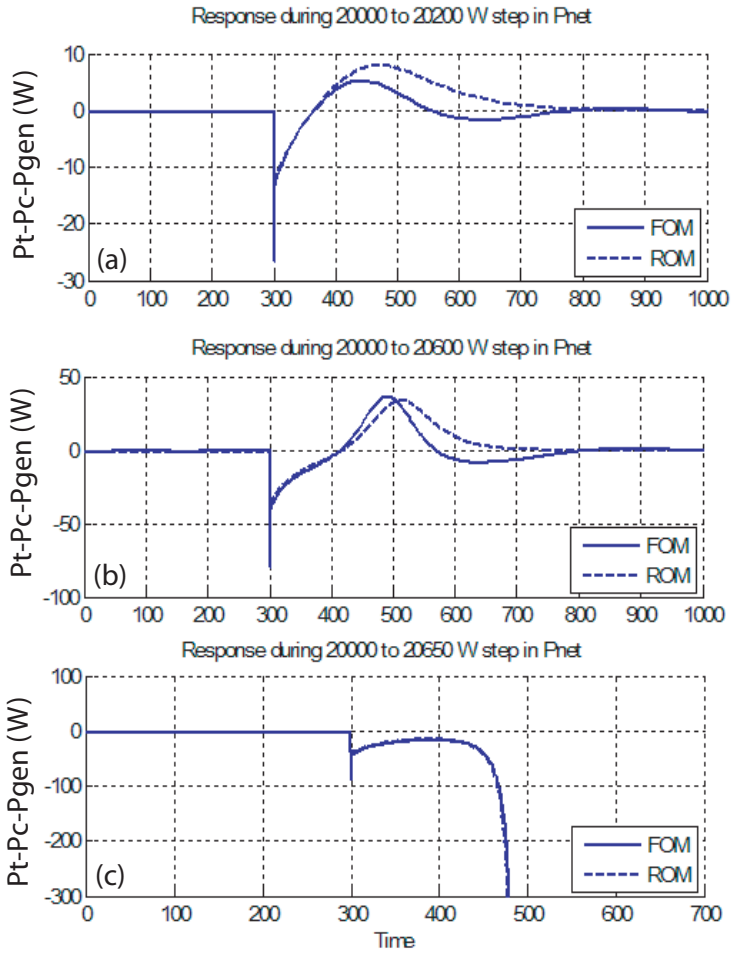

Figure 5.25: Response of Full and Reduced-Order Models for variable load steps

BRP State	HSV	TMG for m_{cb}	TMG for T_{cb}	TMG for N	Next Largest TMG
1	0.503	2.43	8.23	4.32	0.60
2	0.420	5.98	-12.21	-8.60	1.04
3	0.220	0.89	3.47	-0.60	0.01
4	0.010	1.21	-1.23	-11.34	0.18

Table 5.2: Hankel Singular Values (HSV) and Corresponding Transformation Matrix Gains (TMG) for the Balanced Realization Plant (BRP).

5.3.2 Reduced-Order Model

A schematic of the ROM is shown in Fig.5.24. The ROM incorporates the shaft dynamics:

$$\frac{dN}{dt} = \frac{P_t - P_c - P_{gen}}{\alpha \cdot N \ J}, \tag{5.43}$$

with the same GT models as in the full-order model (FOM). Since the GT model and the GT maps do not incorporate any dynamic states and are a key in capturing the nonlinear trends in the power response, they are kept unchanged in the reduced-order model. The SOFC and CB temperature dynamics are lumped and expressed as

$$m_A c_{P_A} \frac{dT}{dt} = H_{abs}^{air\ in} + H_{abs}^{fuel\ in} - H_{abs}^{out} - U_{st} I_{st}, \tag{5.44}$$

where m_A and c_{P_A} are the average mass and heat capacity of the SOFC and CB and the absolute outlet enthalpy (H_{abs}^{out}) is calculated assuming that all the reactions happen instantaneously. The instantaneous chemical equilibrium was analyzed in [87], where it is shown that the reaction kinetics are very fast compared to the temperature dynamics and thus can be ignored.

The static relationships that yield the turbine and compressor power are given as

$$P_t = W_t c_{P_t} T_{in_t} \left(1 - \left(\frac{p_{2t}}{p_{1t}}\right)^k\right) \eta_{ht}, \tag{5.45}$$

$$P_c = W_c c_{P_c} T_{in_c} \left(\left(\frac{p_{2t}}{p_{1t}}\right)^k - 1\right) \eta_{hc}^{-1}. \tag{5.46}$$

The power is a function of the flow (W), the heat capacity (c_P), the inlet temperature (T), the outlet/inlet pressure ratio (p_{2t}/p_{1t}) and the isentropic efficiency (η_h). Given the inlet and outlet conditions, pressure and temperature, the remaining parameters that define the power can be calculated based on the compressor and turbine maps incorporated in the model. Furthermore, the inlet conditions for the compressor and the outlet conditions

for the turbine are known and assumed constant (p_{1c} = 1atm, T_{in_c}=600K, p_{2t} = 1atm, T_{out_t}=300K) as in the FOM.

Finally, although only the CB mass was found to be an important state, in order to improve the accuracy of the ROM, two-mass dynamics are included:

$$\frac{dm_1}{dt} = W_c + W_{fuel} - W_{out}, \tag{5.47}$$

$$\frac{dm_2}{dt} = W_{out} - W_t, \tag{5.48}$$

where m_1 and m_2 are the mass in the SOFC and the CB volume, respectively. It was found that taking into account the mass distribution, i.e., the pressure drop between the compressor outlet and turbine inlet, the steady state matching of the FOM and ROM is improved. Comparing the response of the full and reduced-order models in terms of the shaft power ($P_t - P_c - P_{gen}$), the two model match well as shown in Fig. 5.25. Most importantly, the shutdown effect is captured during a 660W step as shown in Fig. 5.25c. Finally note that the period of time when the shutdown can be first identified, as shown in the previous section, is when $dN/dt < 0$ (i.e., when $P_t - P_c - P_{gen} < 0$). This characteristic is captured accurately by the ROM.

5.3.3 Region of attraction of Reduced-Order Model

In this section the region of attraction of the full-order model is identified and analyzed in the light of the shutdown phenomenon. Let us first define the region of attraction of a stable equilibrium of a dynamic system as:

> **Definition 5.1** *Region of Attraction* [32]: Let $x = x_{ss}$ be an asymptotically stable equilibrium point for the nonlinear system
>
> $$\dot{x} = f(x) \tag{5.49}$$
>
> where $f : D \to R^n$ is locally Lipschitz and $D \subset R^n$ is a domain containing x_{ss}. Let $\phi(t; x)$ be the solution of (5.49) that starts at the initial state x at time $t = 0$. The region of attraction of the equilibrium, denoted by $R_A(x_{ss})$, is defined by:
>
> $$R_A(x_{ss}) = \{x \in D | \phi(t; x) \text{ is defined } \forall\ t \geq 0 \text{ and } \phi(t; x) \to x_{ss} \text{ as } t \to \infty\}. \tag{5.50}$$

In this work, since the equilibrium point is a function of the external input (i.e., $x_{ss}(P^d_{net})$), the RoA, for simplicity, will be denoted as a function of net power, i.e., $R_A(P^d_{net})$. Through the feedforward maps, a given P^d_{net} corresponds to a predetermined set of inputs I_{st}, W_f and P_{gen}. The boundaries of the region of attraction for P^d_{net} = 20 kW for the hybrid

SOFC/GT system is shown in Figures 5.26 and 5.27 as a function of the states ($m_2,\ T,\ N$). Note that the state m_1 was not found to be important for the RoA, i.e., the RoA was shown to be invariant of m_1.

From the region of attraction boundaries it can be seen that if the initial condition for the mass and the rotational speed is high then the required initial condition requirement for the temperature is lowered. This trend can be explained by noting that the higher the initial temperature, mass and rotational speed are, the higher the turbine power (or turbine energy) is. The energy provided to shaft increases as temperature, mass and rotational speed increase. Thus, for example to reach the stable equilibrium starting at low mass, low rotational speed and $P_{net}^d = 20$ kW, the temperature has to be high in order to make up for the energy needed to support the load on the GT shaft.

The RoA provides a numerical tool to capture and understand the shutdown phenomenon. For example, consider the case that the system is settled at an equilibrium point $x_{ss}(P_{net1})$ with $P_{net1} < 20kW$. If it is required to step up the power to 20 kW, the system will shutdown if

$$x_{ss}(P_{net1}) \notin R_A(P_{net} = 20\ kW).$$

On the other hand if

$$x_{ss}(P_{net1}) \in R_A(P_{net} = 20\ kW),$$

the system can reach the desired equilibrium. The same two scenarios hold if at time $t = t_1$ the system is not at steady state but at some transient operating point $x_0 = (m_2,\ T,\ N)_0$ with input $P_{net}^d = P_{net1} < 20\ kW$. If

$$x_0 \in R_A(P_{net} = 20\ kW),$$

it is safe to switch the demanded net power to 20 kW. Otherwise the system will shutdown if that step is applied. This idea is utilized in the next chapter to determine whether a step in net power is possible and to develop a control scheme for the hybrid SOFC/GT system.

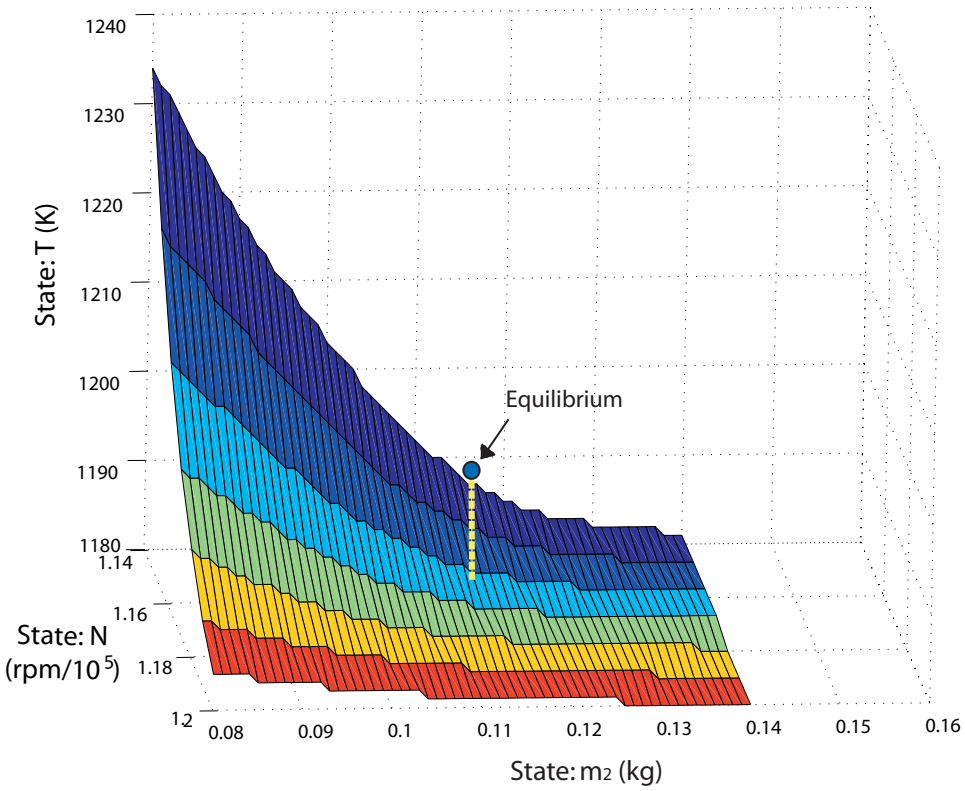

Figure 5.26: RoA lower boundary for reduced-order model and equilibrium ($m_2 = 0.114\ kg/s,\ T = 1189\ K,\ N = 116100\ rpm$) for $P_{net} = 20\ kW$ (3D)

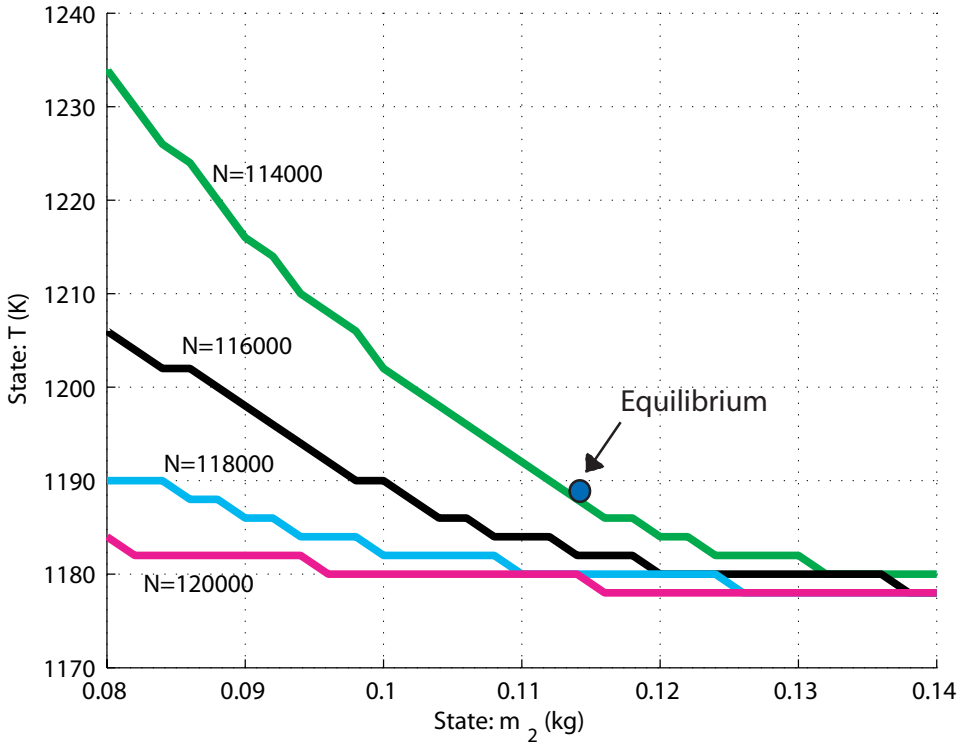

Figure 5.27: RoA lower boundary for reduced-order model and ($m_2 = 0.114\ kg/s,\ T = 1189\ K,\ N = 116100\ rpm$) for $P_{net} = 20\ kW$ (2D)

CHAPTER 6

Feedback Control Design for a Hybrid Solid Oxide Fuel Cell and Gas Turbine System

6.1 Introduction

In this chapter a feedback control scheme is presented to enhance both stability and performance for the hybrid SOFC/GT system. The control scheme is composed of a reference governor that modifies the generator command such that no shutdown occurs and a proportional controller that changes the fuel into the catalytic burner such that the load following performance can be improved. The reference governor uses an estimate of the region of attraction of the model to determine the allowable step size of the generator command. The proportional controller uses the turbine power as the feedback signal to calulate the extra required fuel in the catalytic burner or the fuel cell and consequently to increase the energy to the shaft during a transient. A combination of the incremental step reference governor (IS-RG) and the proportional (P) controller is presented at the end and shown to avoid shutdown and increase the response speed.

6.2 Incremental Step Reference Governor

Guided by the analysis of the shutdown dynamics in Ch. 5, we propose a load governor for the generator to throttle the load application whenever necessary to avoid shut down. While the controller is designed based on the reference governor approach found in [34, 35, 73], the novel aspect of this development lies in the implementation algorithm. In the conventional reference governor approach, the feasible step size of the reference command is determined online through repeated simulations and optimization. The model is simulated forward in time over a given horizon and if the constraints are violated for any time during the simulated period, the reference command is reduced and the simulation is reinitiated. If

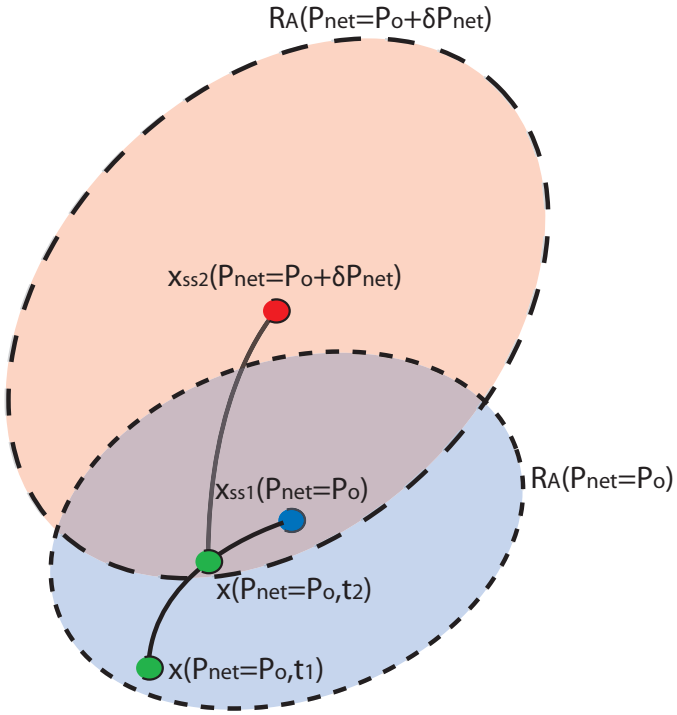

Figure 6.1: Schematic explaining the IS-RG principle

the constraints are satisfied for the simulated trajectory, the value of the reference command is increased by the bisection algorithm until it converges [73]. However, for the complex hybrid SOFC/GT model at hand (with 55 states), the conventional reference governor approach will be very computational demanding and thus infeasible due to the required simulation time.

In this work, the load governor for the generator is synthesized by analyzing the region of attraction of the equilibria corresponding to each intermediate command inputs. To make the implementation of the controller feasible, the region of attraction for each equilibrium is characterized in terms of the dominant states, namely (T_{cb}, m_{cb}, N). To describe the algorithm analytically, we first give the following definition:

Definition 6.1 *Permissible Incremental Step (IS) Change*
Let

$$x_1 = (T_{cb},\ m_{cb},\ N) \in R_A(P^d_{net} = P_0). \tag{6.1}$$

If

$$x_1 = (T_{cb},\ m_{cb},\ N) \in R_A(P^d_{net} = P_0 + \delta P_{net}), \tag{6.2}$$

then δP_{net} is a permissible IS change (i.e., the power can be increased by δP_{net}).

A graphic explanation of the permissible incremental step change is shown in Fig. 6.1. The operating point at time $t = t_1$ belongs to $R_A(P^d_{net} = P_0)$ but not to the $R_A(P^d_{net} =$

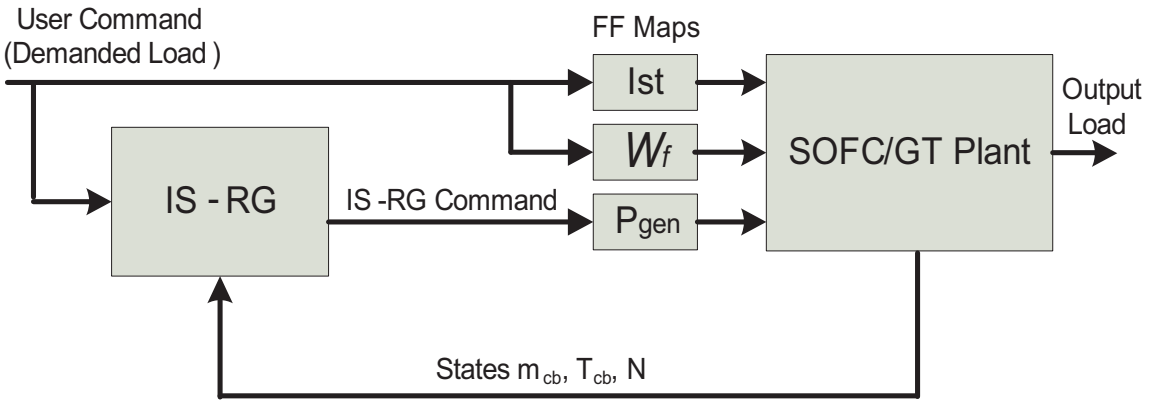

Figure 6.2: Schematic of the closed loop SOFC/GT plant with the IS-RG controller

$P_0 + \delta P_{net}$), thus δP_{net} is not a permissible incremental step at $t = t_1$. At time $t = t_2$ the operating point belongs in $R_A(P^d_{net} = P_0 + \delta P_{net})$, thus P_0 to $P_0 + \delta P_{net}$ is permissible.

A schematic of the proposed closed loop configuration, with the incremental step reference governor (IS-RG), is shown in Fig. 6.2. The IS-RG utilizes a lookup table of the RoA boundaries in order to determine whether an incremental step load δP_{net} is permissible. At each time t the IS-RG evaluates the permissibility of an incremental increase on net power δP_{net} . If the current operating point (m_{cb}, T_{cb}, N) at time t and with input P_{net_t} belongs to the region of attraction of the equilibrium with input $P_{net_t} + \delta P_{net}$ then the step can be applied without causing future system shutdown. A formal definition of the IS-RG is given here:

Definition 6.2 *Incremental Step - Reference Governor (IS-RG)*
For the dynamic system of the form $\dot{x}(t) = f(x, u)$, given the desired input $u_d(t)$ and $\delta P_{net} = constant$, the IS-RG calculates the input $u_p(t)$ according to:

$$u_p(t + \delta t) = \begin{cases} \min\left[u_p(t) + \delta P_{net},\ u_d(t)\right], & \text{if } \delta P_{net} \text{ is a permissible } IS; \\ \min\left[u_p(t),\ u_d(t)\right], & \text{if } \delta P_{net} \text{ is not a permissible } IS \end{cases}$$

where $u_p(t + \delta t)$ denotes the input to be applied at the next time step after t.

The IS-RG applies incremental steps to the reference command unitl the final desired setpoint is reached. To guarantee that the desired setpoint will be reached, i.e.,

$$\lim_{t \to \infty} u_p(t) = u_d,$$

a sufficient condition is that δP_{net} is chosen such that:

$$x_{ss}(P_{net} = P_0 + k\delta P_{net}) \in R_A(P_{net} = P_0 + (k+1)\delta P_{net}),\ k = 0, 1, 2, \dots , \tag{6.3}$$

i.e., the equilibrium with the current input, $P_0 + k\delta P_{net}$, should belong to the region of attraction of the equilibrium with $P_0 + (k+1)\delta P_{net}$. Condition (6.3) can be satisfied by choosing δP_{net} to be sufficiently small. If an intermediate equilibrium, x_{ss} does not belong to the region of attraction of the next equilibrium, we ran into the possibility of reaching an intermediate equilibrium for $P_{net} < P_{net}^{final}$ and remaining at that equilibrium without being able to increase the load any further. It is shown later that a small δP_{net} will not slow down the system as long as the sampling time is relatively faster than the system dynamics.

To summarize, given the permissible input u_p and the desired input u_d, the IS-RG algorithm is given below. Note that in case of a step down in the desired input, the controller takes no action in filtering the inputs and simply sets the permissible input equal to the desired. This is done for the SOFC/GT system since an equilibrium for a given input always belongs to the region of attraction of an equilibrium with a smaller input (i.e., lower P_{net}). Thus, response of the closed loop system with the IS-RG to a step down is identical to that of the open loop without the IS-RG, shown in Ch.5 (Fig. 5.6).

IS-RG Algorithm:

if $u_d > u_p$
  if δP_{net} **is a permissible IS**
    $u_p = u_p + \delta P_{net}$
  else
    $u_p = u_p$
  end
else
  $u_p = u_d$
end.

6.2.1 Implementation of the IS-RG on the ROM

The IS-RG is first implemented in the ROM, for which a schematic of its region of attraction was given in Sec. 5.3.3. The region of attraction boundaries are determined by simulating a grid of initial conditions for a range of net powers and checking whether the system converges to the stable equilibrium. Using optimization techniques, the boundary temperature $(T_{cb}^{P_{net}^d})_b$ of the RoA of the ROM is parametarized in terms of N and m_{cb} for each P_{net}^d as a quadratic funtion:

$$(T_{cb}^{P_{net}^d})_b = a^{P_{net}^d}(N) \cdot m_{cb}^2 + b^{P_{net^d}}(N) \cdot m_2 + c^{P_{net}^d}(N), \tag{6.4}$$

where the parameters $(a^{P_{net}^d}(N),\ b^{P_{net}^d}(N),\ c^{P_{net}^d}(N))$ are stored as static maps varying with P_{net}^d and N. At each time t, given the incremental step size δP_{net}, the measured states

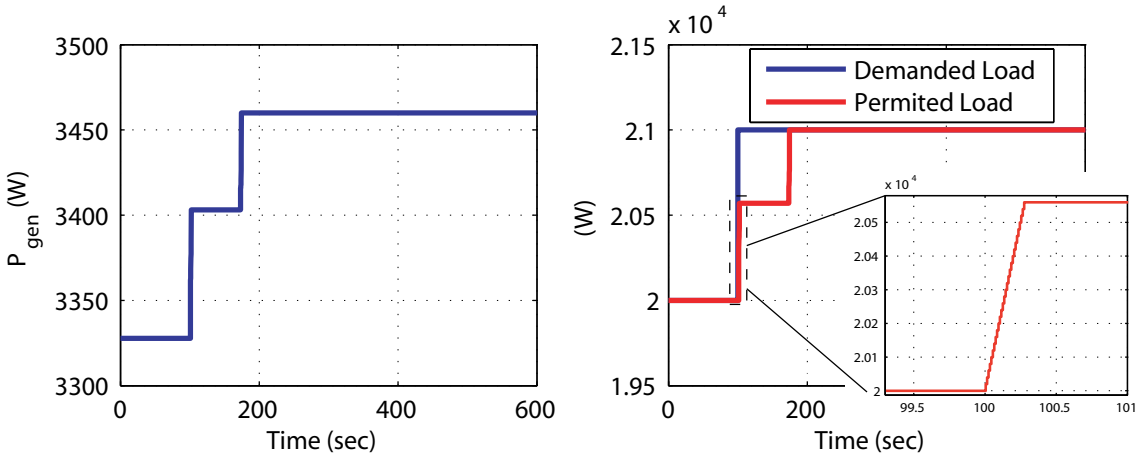

Figure 6.3: Closed Loop Load Step Response from 20 to 21 kW on the ROM with the IS-RG

$(T_{cb},\ N,\ m_{cb})$ and the desired load P_0, the IS-RG checks if

$$(T_{cb}^{P_0+\delta P_{net}})_b < T_{cb}.$$

If this condition is true, then δP_{net} is a permissible incremental step. Note that operating point $(T_{cb},\ N,\ m_{cb})$ with input P_0 always satisfies the following:

$$(T_{cb}^{P_0})_b < T_{cb}.$$

The response for a 20 to 21 kW step is shown in Fig. 6.3. No shutdown occurs during the transition and the final load is reached. Note that δP_{net} is chosen equal to 20 W such that condition (6.3) is satisfied. It can be seen though, that the individual steps of 560W and 440W in the demanded load appear as instantaneous. That is due to the fast sampling rate compared to the system dynamics. Each of those steps consists of multiple steps of amplitude δP_{net}. For example the 560W step occurs in 28 steps of $\delta P_{net} = 20\ W$ over a time period of 0.28 s, which is relatively short compared to the system's time constant.

6.2.2 Implementation of the IS-RG on the FOM

To integrate the IS-RG with the full-order model, the RoA is calculated and parametarized as a function of the dominant states m_{cb}, T_{cb} and N for the range of operating loads. An example of the RoA boundaries for P_{net} =20 kW is given in Fig. 6.4. If we set the initial conditions above this boundary and simulate the model, the stable equilibrium will be reached, i.e., every point above the boundary for a given N belongs to the $R_A(P_{net} = 20kW)$.

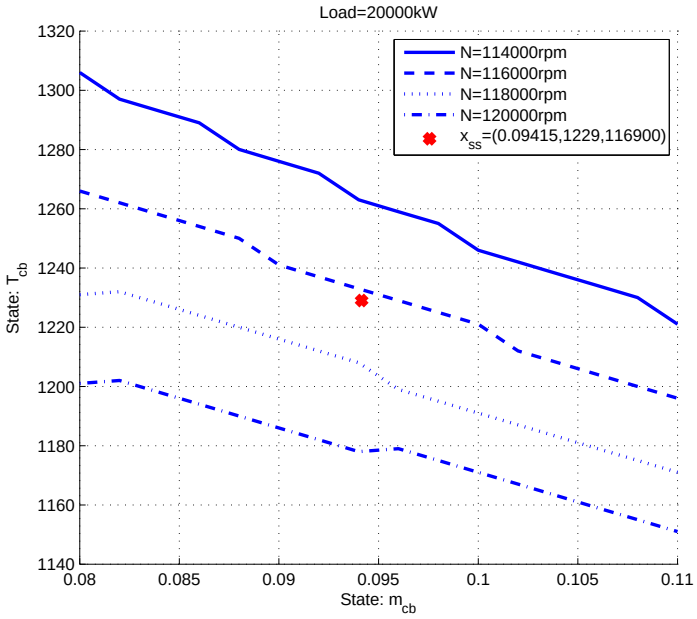

Figure 6.4: Lower boundaries of $R_A(P_{net} = 20kW)$ as functions of m_{cb}, T_{cb} and N

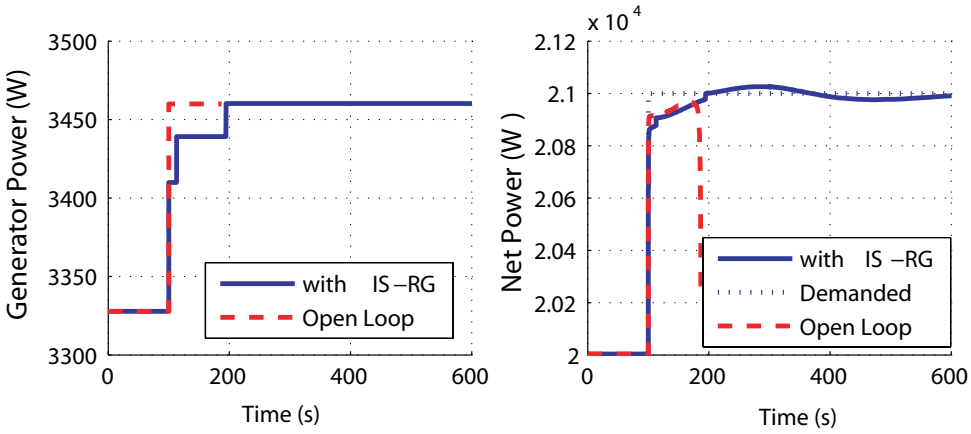

Figure 6.5: Open and Closed Loop Load Step Response from 20 to 21 kW

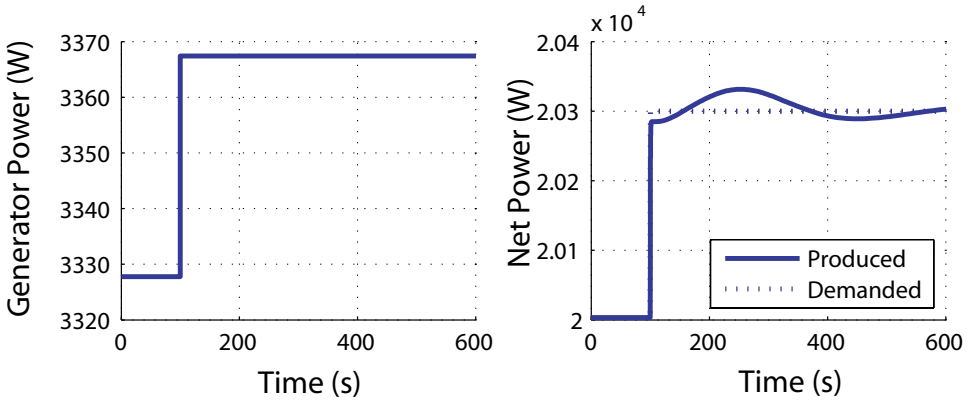

Figure 6.6: IS-RG Closed Loop Load Step Response from 20 to 20.3 kW

Linear functions are used to represent the RoA boundaries via curve fitting. Optimization techniques are employed to determine the parameters of those functions:

$$T_{cb\ B}^{P_{net}} = a^{P_{net}}(N) \cdot m_{cb} + b^{P_{net}}(N). \tag{6.5}$$

The parameters $a^{P_{net}}$ and $b^{P_{net}}$ are stored as lookup tables, indexed by N and P_{net}, for online implementation. Note that for the FOM, a linear expression was used to interpolate the RoA boundaries since the RoA was calculated for a smaller range of m_{cb} and thus was almost linear.

Following the methodology described above and utilizing the offline calculated estimates of the RoA, the IS-RG controller safeguards the system when a step load increase is applied. Fig. 6.5 shows the simulation of the closed loop FOM and IS-RG for a 20 to 21 kW step increase in desired net power. Note that for the same step the open loop system (without the IS-RG) shuts down shortly after the step is applied (dashed line in Fig. 6.5), while the open loop system with a P_{gen} rate limiter (Fig. 5.7) exhibits a settling time of 122 s. The size of δP_{net} is set to 20 W to ensure condition (6.3) is met. Furthermore, note that during a 20 to 20.3 kW step (small step) the IS-RG exhibits the same performance as the open loop plant since the equilibrium for $P_{net} = 20\ kW$ belongs in the $R_A(P_{net} = 20.3\ kW)$ (Fig. 6.6).

While the IS-RG avoids shutdown, its main function is to slow down the application of the generator load to ensure safe operation. It does not attempt to change the other dynamics of the system. In order to enhance the performance, the IS-RG controller will be combined with a proportional controller that controls the fuel flow into the CB during a transient to increase the E_{in} as proposed in Ch.5.

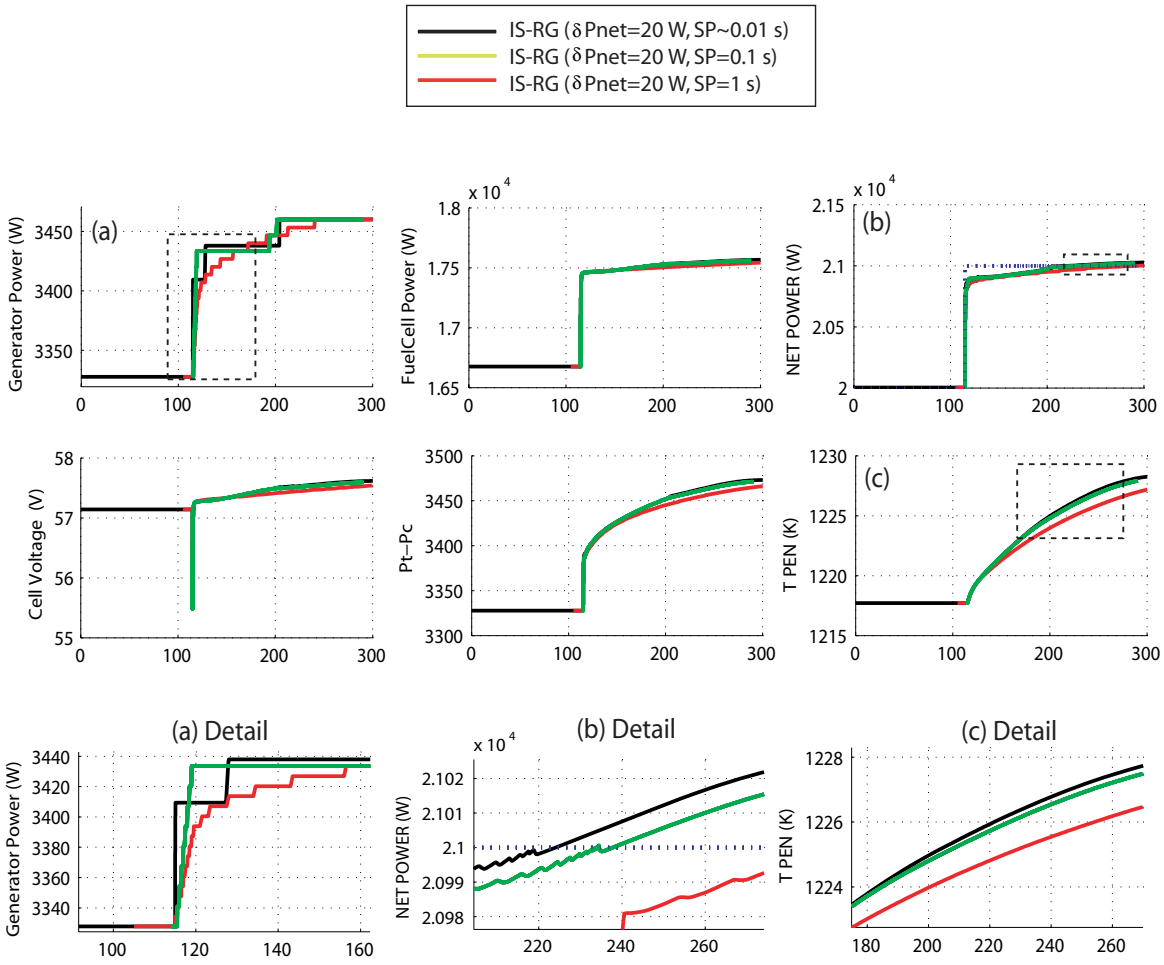

Figure 6.7: IS-RG Response with various sampling periods (SP) and δP_{net}

6.2.3 Effects of Sampling Period (SP) to Closed Loop Response

In this section the effects of sampling period (SP) of the IS-RG controller on the system response are examined. The controller is descritized using a sampler in the input (measurements) and a zero-order hold at the output (reference command). The sampling period of the controller, for the simulation results shown up to this point, was variable and determined by Matlab/Simulink©. On average, Matlab/Simulink© sets the sampling time of the controller during the transient equal to 0.01 s (i.e., 100 Hz). Figure 6.7, shows the system response for a 20 to 21 kW step for 0.01 s, 0.1 s and 1 s sampling periods and $\delta P_{net} = 20$ kW. Note that IS-RG response indicated in previous figures, is shown here with the black line.

It can be seen that for sampling frequencies of 100, 10 and 1 Hz, the system's settling time[1] during a 20 to 21 kW step increase in load is 76, 77 and 83 s, respectively. This simulation shows that for a 10 times increase in the IS-RF sampling period, the settling time deteriorates by 1%, while for a 100 increase in sampling period, the settling time deteriorates by 9%. This result shows that, without requiring high sampling frequency, the IS-RG can achieve the performance at the desired level.

This comparison also verifies the result mentioned in Sec. 5.2.2, where the slower the P_{gen} reaches the desired setpoint, the slower the response of P_{net} is. Not maximizing the P_{gen} allows for more air in the SOFC, resulting in decreased SOFC temperature and consequently less SOFC power (Figure 6.7c and Figure 6.7c-Detail).

6.2.4 Comparison of IS-RG with conventional RG

Compared to the IS-RG, the conventional RG approach utilizes online optimization to determine the step size at each time. For a dynamic system of the form $\dot{x} = f(x, u)$ with desired input $u = u_d$, the reference governor calculates an input $u = u_{rg}$ with $K \in [0, 1]$ such that

$$u_{rg}(t + \delta t) = u_{rg}(t) + K(u_d - u_{rg}(t)) \tag{6.6}$$

where $K = 0$ if no further increase of the input can be achieved or $K = 1$ if applying the desired input is possible [23, 73]. The way K is determined for a dynamic system of the form $\dot{x} = f(x, u)$ is via an online optimization problem formulated as:

$$\max_{K} \{u_{rg}\}, \text{ such that } O_f \text{ is statisfied} \tag{6.7}$$

[1]Settling time (ST) in this work is defined as the period of time required to transition from 10% to 90% of the demanded step load, i.e., time from 10% of $(P_{net}^{final} - P_{net}^{initial})$ to 90% of $(P_{net}^{final} - P_{net}^{initial})$.

and O_f is the set of constraints applied to the states of the system. In the case of the hybrid SOFC/GT system, the constraints can be expressed as:

$$O_f = \{x \in R_A(P_{net} = u_{rg}(t))\} \tag{6.8}$$

where the operating point x has to belong within the region of attraction of the equilibrium point with the current input ($u_{rg}(t)$).

The optimization problem is solved using the regions of attraction calculated for the FOM. Note that the optimization is not performed via repeated simulations. Instead, the offline calculated RoA maps are used.

Bisection optimization technique was used to determine at each time step the value of K. Assuming that $K = 0$ yields an allowable input that does not violate the constraints as posed in (6.8) (i.e., we start from a stable equilibrium), let us define $h(K)$ as:

$$h(K) = \begin{cases} 1, & \text{if } O_f \text{ is satisfied;} \\ 0, & \text{if } O_f \text{ is not satisfied} \end{cases} \tag{6.9}$$

where it is assumed $h(K = 0) = 1$. Given an interval $[K_r, K_l]$ with right limit (i.e., lower limit) K_r and left limit (i.e., higher limit) K_l, the bisection algorith is summarized as:

Bisection Algorithm:

while $|K_r - K_l| > \epsilon$
  $K_m = (K_r + K_l)/2$
  If $h(K_l) \cdot h(K_m) > 0$
    $K_l = K_m$
  else
    $K_r = K_m$
  end if
end while

where ϵ is set to 0.01 in order to prevent the optimization from running infinitely. A comparison of the IS-RG and the RG presented here is given in Fig. 6.8. The responses of the two closed loop systems match well while the time[2] required to simulate 1000sec for the closed loop FOM and IS-RG is 285.2sec while for the closed loop FOM and conventional RG is 341.7sec. Furthermore, 84.2sec are required in order to simulate the plant in open loop configuration using as input for P_{gen} the command the the IS-RG yields. Thus, subtractict 84.2sec from either closed loop times, one can see that a reduction of 22% is achieved in computational efficiency.

[2]Note that the simulation time was measured using the command *cputime* in Matlab/Simulink.

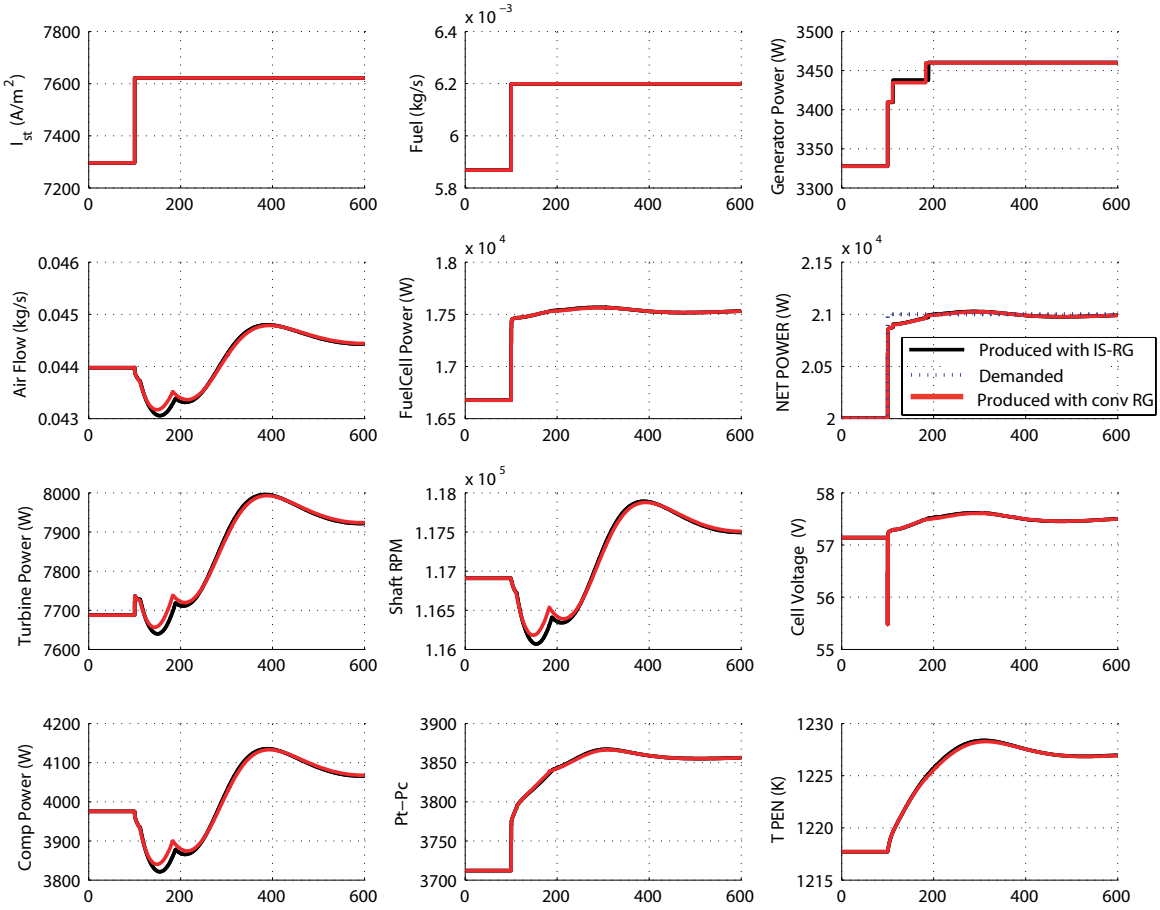

Figure 6.8: Comparison of IS-RG and conventional RG closed loop systems

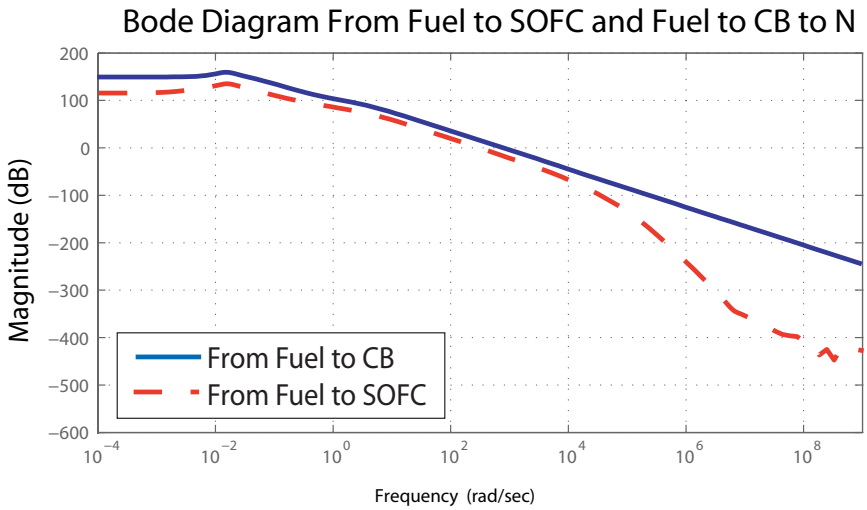

Figure 6.9: Bode plots from fuel in CB and from P_{gen} to P_{tc}

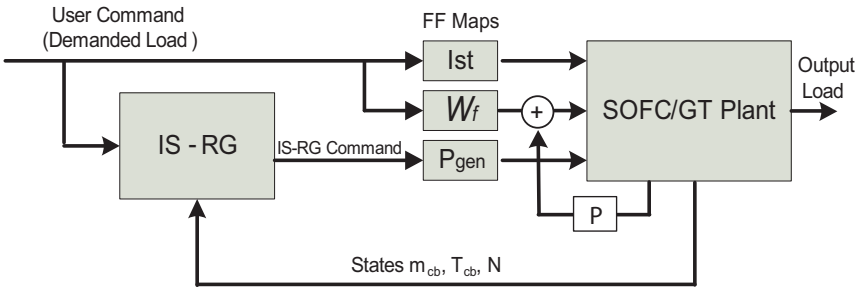

Figure 6.10: Bode plots from fuel in CB and from P_{gen} to P_{tc}

6.3 Proportional CB Fuel Controller

The RoA of the SOFC/GT model was shown to be a strong function of the CB temperature and mass (besides the shaft speed). In order to allow for larger and faster load steps we choose to add extra fuel in the system during the transient. The extra fuel will eventually reach the CB and increase both its temperature and mass flow in order to allow for rapid support of the generator load and thus improve the load following performance of the plant. Two options are avaliable for adding extra fuel during load transitions, one is to add fuel directly in the SOFC and the other to bypass the SOFC and feed the fuel directly into the CB. As far as controlling the shaft speed and avoiding shutdown are conserned, feeding fuel into the CB or the SOFC have similar effects as shown by the Bode plot in Fig. 6.9 while adding fuel in the CB has a higher control authority compared to adding fuel in the SOFC. The corresponding control configuration is shown in Fig. 6.10, where via a proportional controller extra fuel is added into the system.

The extra fuel flow into the system, W_{ef}, is controlled proportionally to the turbine power deficiency, i.e., the current turbine power P_t minus the desired turbine power P_t^* as

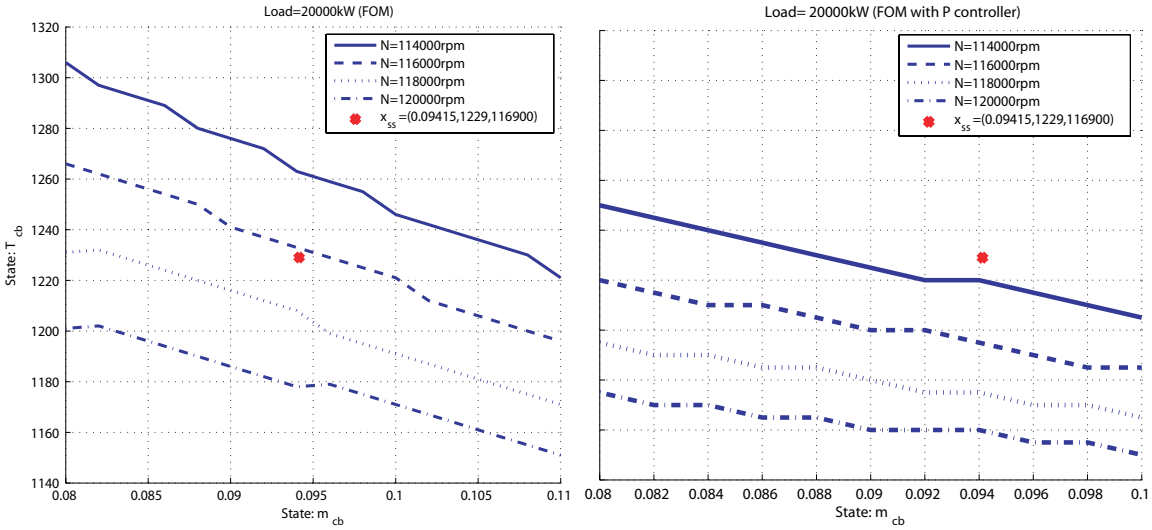

Figure 6.11: Region of attraction for the open loop plant and the closed loop with the CB fuel proportional controller

a function of the demanded net power:

$$W_{ef} = K_P \left(P_t^*(P_{net}) - P_t\right) \tag{6.10}$$

where $P_t^*(P_{net})$ is the desired turbine power as a function of the net power and the extra fuel flow, W_{ef}, is determined via the power deficiency of the turbine. The proportional control was chosen since the fuel flow increases the turbine inlet temperature which is proportional to the turbine power.

The region of attraction with the proportional controller for regulating the fuel in the CB is shown in Fig. 6.11. For comparisson, the RoA of the system without the proportional controller is shown as well. The proportional controller expands the RoA of the system since it is now possible to reach the equilibrium point from a lower energy point than before (without the P controller) due to the added energy from the extra fuel input. This fact allows the combination of the IS-RG with the proportional control with no need for redesigning the IS-RG.

The system responses with the IS-RG, the proportional controller that adds extra fuel in the SOFC and the proportional controller that adds extra fuel in the CB are shown in Fig. 6.12. The overshoot of the fuel allows for larger and faster P_{gen} steps, contributing to improved load following capabilities by reaching the final setpoint faster. Increasing further the value of the proportional gain K_P will increase the response speed even more but will also increase the temperature gradient in the CB.

The tuning of either P controllers, depends on the constraints set on the temperature gradient of the SOFC or the CB. An guide for tuning the P controller for adding fuel in

the CB is outlined as follows: The relationship between the controller gain, the average CB temperature temporal gradient (K/s) and the settling time during a 20 to 21 kW step in P_{net} is given in Figure 6.13. If no constraints exist, a large gain will allow a step in the generator load directly to the final load. If temperature gradient constraints, O_{tg}, and settling time constraints, O_{st}, are posed for the system as:

$$O_{tg} = (T_{cb} \text{ gradient} \leq a) \tag{6.11}$$
$$O_{st} = (\text{Settling time} \leq b), \tag{6.12}$$

with corresponding values of the controller gain

$$K_{tg} = \left\{K \in R^1 \mid O_{tg} \text{ is satisfied}\right\} \tag{6.13}$$
$$K_{st} = \left\{K \in R^1 \mid O_{st} \text{ is satisfied}\right\} \tag{6.14}$$

then a controller gain can be selected such that both constraints are met. For less fuel consumption and thus better system efficiency, if $K_{st} \leq K_{tg}$, the controller gain should be chosen equal to K_{st}. Note that if $K_{st} > K_{tg}$, then no value of the controller gain exists such that both contstraints are satisfied.

An example on tuning the proportional controller gain is illustrated in Fig. 6.14. Let the constraints be

$$O_{tg} = (T_{cb} \text{ gradient} \leq 0.35\ K/s) \tag{6.15}$$
$$O_{st} = (\text{Settling time} \leq 68\ s), \tag{6.16}$$

and the controller gains that satisfy those contraints, as shown in Fig. 6.14, are

$$K_{tg} \leq 1 \cdot 10^{-6} \tag{6.17}$$
$$K_{st} \geq 0.39 \cdot 10^{-6}. \tag{6.18}$$

For minimum fuel consumption and maximum system efficiency the smallest controller gain is chosen:

$$K = K_{st} = 0.39 \cdot 10^{-6}. \tag{6.19}$$

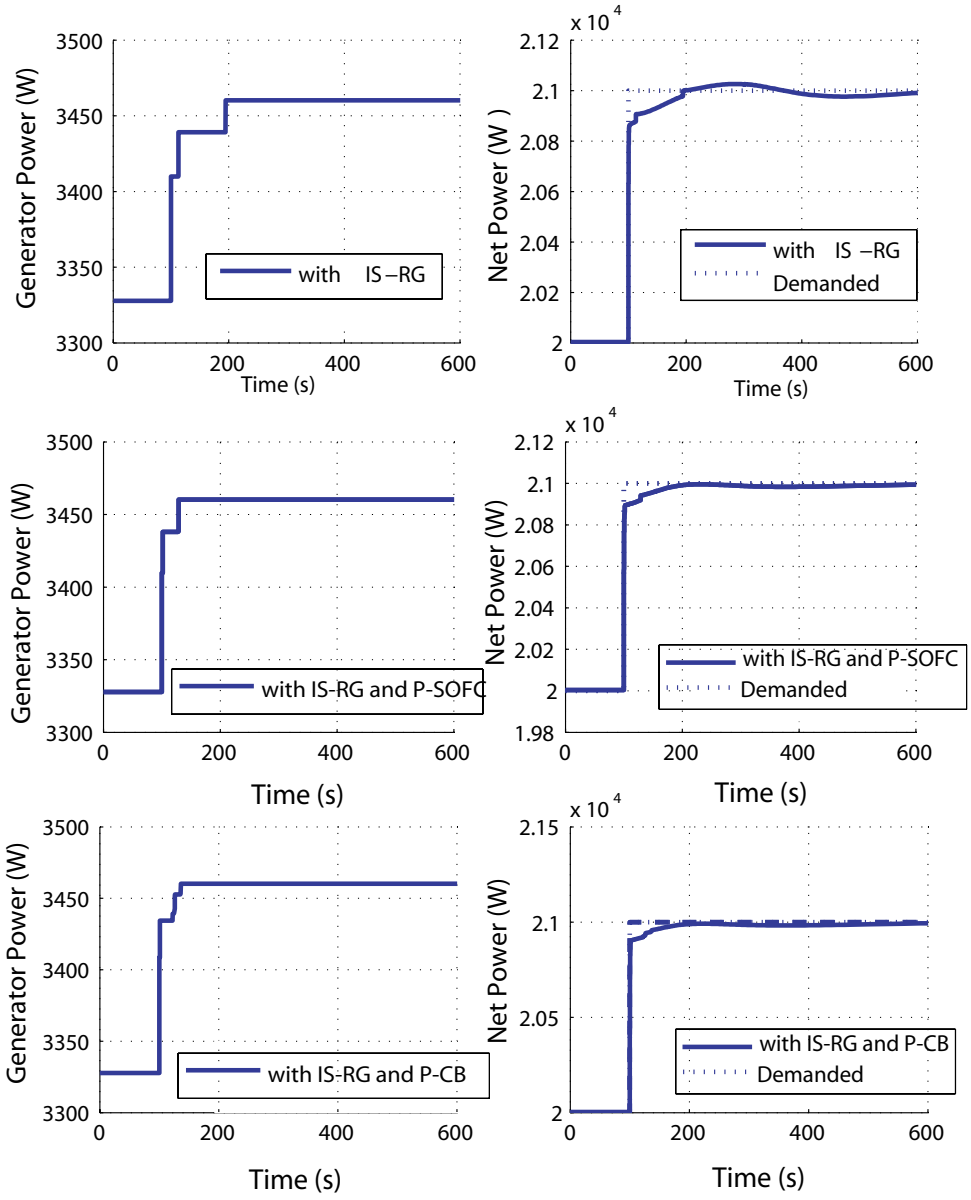

Figure 6.12: Step Response from 20 to 21 kW with IS-RG and P control of fuel in CB ($P-CB$) and SOFC ($P-SOFC$)

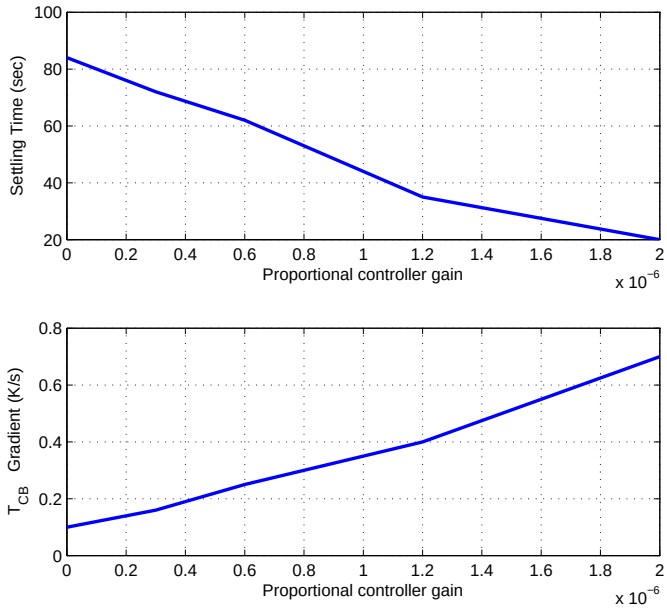

Figure 6.13: Settling time and T_{cb} gradient for variable K during a 20-21 kW step in P_{net}

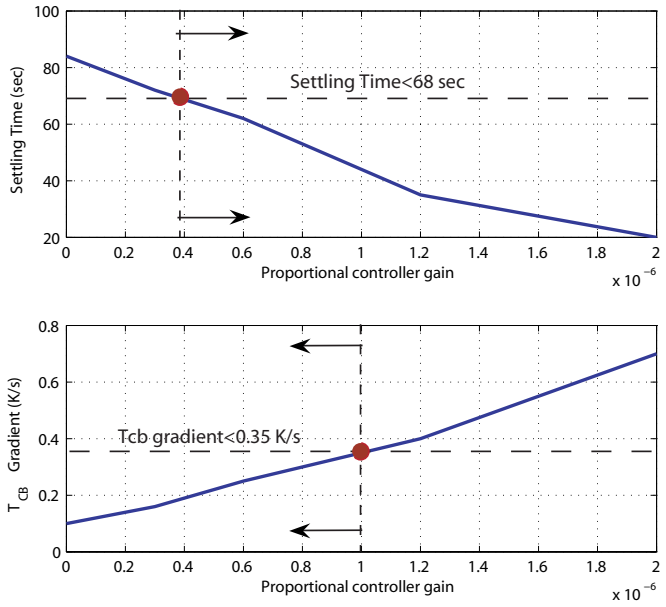

Figure 6.14: Example on tuning the proportional controller gain

CHAPTER 7

Summary, Conclusions and Future Work

7.1 Summary

In this work the control-oriented analysis of two integrated fuel cell systems with energy recuperation devices is presented. The first one, presented in Ch. 2-3, incorporates a CPOX reformer, a PEM fuel cell and a CB for energy recuperation while the second one, presented in Ch.4-6, incorporates an SOFC, a GT and a CB for energy recuperation. A summary of the control analysis results is given below:

- *Chapters 2-3 : CPOX reformer system with heat recirculation*
  In Ch. 2 a control-oriented model of the CPOX-based reformer system is presented. The modeling equations are summarized while optimization techniques are utilized to determine the optimal fuel and air operating points for the whole range of operation of the system. It is shown that running the system in open loop configuration will cause CPOX reactor overheating and hydrogen starvation during load transitions. The root causes are identified as the large pressure drop of the HDS which in turn causes oxygen to carbon ratio discrepancies in the CPOX during transient operation. In Ch. 3, a feedback control scheme is proposed to mitigate the issues associated with open loop operation. The observer-based control scheme utilizes as measurements the CPOX and the CB temperature. It is important to note that the CB, besides increasing the steady state efficiency of the system, is also used for the control design by providing vital measurements. The measurement of the CB temperature is shown to be vital in ensuring proper and fast estimation of the states of the plant. Furthermore, robustness evaluation of the feedback control scheme is examined under various uncertainty scenarios, namely CPOX and HDS clogging, fuel composition variations and CB modeling uncertainty. The controller was shown to be robust against all the scenarios examined while the closed loop response showed little or no deterioration in performance.

- *Chapters 4-6 : SOFC/GT hybrid system*
  In Ch 4, the hybrid SOFC/GT system is presented and its operation is explained. A dynamic, nonlinear and control-oriented model of the system is described where the individual component models are delineated. In Ch. 5, the optimal steady state setpoints for the generator load, the fuel flow and the SOFC current are derived by maximizing the system's efficiency. Those setpoints are then used for open loop analysis where the system dynamics are characterized. It is shown that the system will shutdown in case of large and rapid power transitions while the shutdown phenomenon is analyzed. The shaft dynamics and the GT nonlinearities are shown to initiate a vicious cycle between the SOFC and the GT, that eventually leads to the shutdown. Finally, in Ch. 5, a reduced-order model including the lumped SOFC and CB mass dynamics, the average SOFC and CB temperature dynamics and the nonlinear shaft dynamics is shown to accurately capture the shutdown phenomenon.
  In Ch. 6, an incremental step reference governor is proposed, which in combination with a proportional controller for regulating the fuel flow to the CB, is able to mitigate shutdown during rapid and large load transitions. The IS-RG utilizes the region of attraction of the reduced-order model to check whether an incremental step is permissible. Combining the IS-RG with a proportional fuel controller manages to enhance both system stability and performance, by avoiding the shutdown and reducing the settling time of the system. It is important to note that the proposed control scheme enhances the robustness of the IS-RG since it expands the RoA.

7.2 Conclusions

The important conclusions of this work are highlighted below:

- The energy recuperation devices (ERDs) promote system efficiency and provide measurements that facilitate in the system observability and improve the closed loop system performance. The CB temperature (in the reformer and the SOFC system) and the GT shaft rotational speed (in the SOFC system) are shown to facilitate the control design.

- If the dominant coupling dynamics between the FC system and the ERDs are thermal-based, then the system operation is less susceptible to issues caused from this coupling. If the dominant coupling dynamics are pressure-based then the FC system can be led to shutdown during load transitions if proper control schemes are not incorporated to regulate the energy balance between the FC system and the ERD.

- The use of optimal steady state setpoints for load transitions makes the system susceptible to transient issues and imposes the need for advanced control schemes. The optimal steady state setpoints lie on the boundary of operation of the system and uncertainties or disturbances can cause instability.

- In a fuel reformer, the hydro desulphurization (HDS) process introduces a large pressure drop in the fuel path and requires proper control of the fuel flow to avoid discrepancies from the desired fuel-air ratios. If the HDS process is chosen to be included in the reformer (i.e., online desulphurization), extra fuel flow has to be added during load transitions to ensure that the desired amount of fuel is desulphurized.

- An incremental step reference governor (IS-RG) is proposed to filter the generator load command and avoid system shutdown. The IS-RG is shown to exhibit the similar performance to a conventional RG but required less computational effort since no simulations are done. Furthermore, there is no requirement for high sampling rates.

7.3 Review of Important Assumptions

The important assumptions utilized here are summarized below in order to highlight the limitations of the developed models and motivate the extensions of this work.

- All the reactors in this work, except the SOFC, are modeled as lumped parameter volumes with homogenous pressure and temperature. No spacial distribution of the temperature, pressure or the reactants is captured in a single volume. The control design imposes the constraint for low-order control-oriented modeling tools, thus a highly complex distributed parameter model would be infeasible. The SOFC model that included spacial distribution of several variables had to be simplified for the controls analysis.

- The developed models are not suitable for analyzing the start up dynamics of the system. The auxiliary devices used for start up as well as the start up dynamics are not modeled in this work.

- It is assumed that all gases obey the ideal gas law.

- No heat losses to the environment are taken into account.

- For the reformer system examined, the HDS process was assumed perfect, removing all the sulphur from the fuel stream. Similarly, the CO removal in the WROX reactor was assumed complete. The effects of sulphur and CO in the reformer were not modeled or examined in this work.

- The fuel entering the hybrid SOFC system was assumed pre-reformed. The reformer model and dynamics were not included in this model. Furthermore, the air entering the SOFC system was assumed preheated. The HEX between the turbine exhaust and the air inlet was not included in the analysis.

7.4 Future Work

The work presented in this dissertation can be extended in several directions including:

- *Model Validation*
  The modeling techniques used for components such as the heat exchangers, the blower, the gas turbine and the mixer can be found in the literature and have been widely validated. Models for other components such as the PEM fuel cell, the SOFC and the catalytic burner, require further tuning and parameter calibration in order to match experimental results. Even though the qualitative trends (i.e., the transient response) are expected to match a real system, the quantitative results (i.e. the steady state values) presented in this work might vary if the model is tuned based on experimental data. Furthermore, validation of the integrated system models would be significant in supporting the analysis and results presented in this work.

- *Model Expansion*
  For the SOFC/GT system examined, only the core system components were modeled and integrated into the system. Additional balance of plant components such as heat exchangers, reformer etc., would pose even more challenges with respect to the system's operation and performance. Integrating those components into the system and examining the overall system would be a significant extension to this work. An example of an integrated SOFC based system with a reformer and other balance of plant components is shown in Fig. 7.1. In this system, the exhaust from the turbine is utilized in preheating the inlet air and fuel flows to the reformer, where a portion of the fuel is pre-reformed. Power conditioning units are responsible for connecting the SOFC and the generator to the power bus from which the propulsion motor and other loads draw power. Finally, other components, such as a water evaporator and a heat recovery unit are incorporated for full exploitation of the SOFC exhaust energy.

- *Further Control Analysis*
  Control issues such as the thermal management of the SOFC in the case of a hybrid SOFC/GT system or active air flow control for the catalytic burner were not addressed in this work. In addition, if the SOFC/GT model is integrated with balance of plant components, other control issues might arise. Understanding and mitigating the control issues not addressed in this work will give a broader perspective on the complete control loops required for those systems.

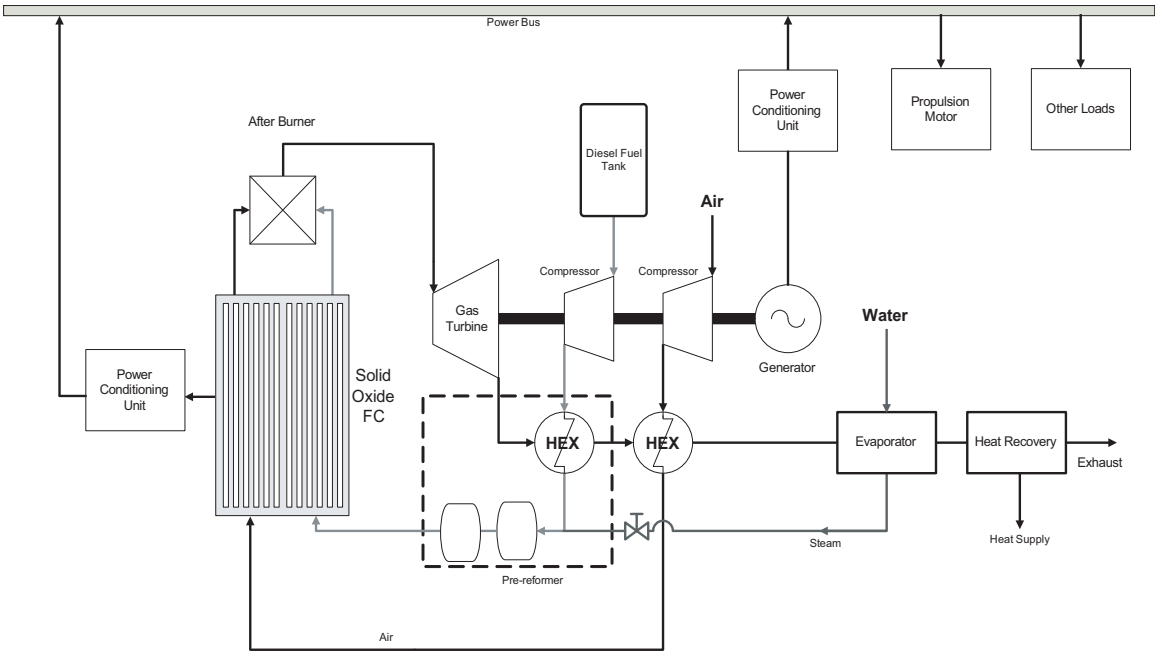

Figure 7.1: Integrated SOFC/GT system with reformer and balance of plant components included

- *Steady State Setpoints*
  In this work the optimal steady state setpoints were determined in terms of system efficiency and utilized for the controls analysis. Even though the designed controllers allow load transitions using those setpoints, in an actual application some of the steady state efficiency achieved can be sacrificed for improved system robustness. Operating at suboptimal efficiency setpoints (i.e., at lower steady state efficiency) will allow for easier load transitions. A trade off analysis between the steady state efficiency (i.e. the operating setpoints) and the transient robustness would be a useful extension of this work.

7.5 Potential Applications

Besides the application of the developed control algorithms to physical fuel cell-based systems, a list of other potential applications of this work and the developed models is given in this section:

- *Hybridization Analysis*
  The developed models can be utilized for analyzing the requirements for external power sources such as batteries or ultra-capacitors. The designed control schemes managed to improve significantly the transient speed of the system but depending on the requirements, another power source can be incorporated into the system to

further enhance the system's performance. Furthermore, to safeguard the fuel cell system and promote robustness, it might be required to slow down the rate at which load is drawn from the stack and supplement that load deficiency via a hybrid power source. The developed models can be used for the sizing, optimization, design and analysis of such hybrid configurations.

- *Fault Diagnosis*
  Fault diagnosis is another potential use for the models and the theory developed within the scope of this dissertation. The transient faults identified in this work can be predicted by utilizing the mathematical models and the theory developed for the systems examined. For example, in the case of the SOFC/GT system, shutdown can be diagnosed according to Theorem 5.1. This theory enables the detection of system shutdown before it occurs using simple measurements of rotational speed, pressure and temperature. In the case of the reformer system examined, measurement of the fuel and air flows can predict reactor overheating and potential hydrogen starvation. The designed control schemes are designed to safeguard the system against such faults but due to modeling errors, disturbances or other uncertainties they can still occur in an actual application. The dynamic analysis presented in this work can be used to detect such faults and allow the user or a high-level controller to take action before there is permanent damage to the system.

- *Online Parameter Estimation*
  The FC system is a chemical-based system and depends highly on the reaction rates and the corresponding catalysts. The performance of the reactors and the corresponding catalysts are known to degrade significantly over time and thus require precise monitoring in order to compensate for the degrading performance with adjustments on the control scheme (i.e., adaptive control). The developed models can be utilized for online parameter estimation. Measuring directly certain parameters is unfeasible, so the designed models can facilitate in estimating parameters that are hard to measure and then utilize those estimates to online tune the controller gains.

- *Cost versus Performance Analysis*
  If detailed information on the manufacturing and operating cost of each subsystem or component becomes available, the developed open or closed loop schemes can be used to optimize the performance of the system under certain cost constraints or optimize the system's cost (i.e., minimize) under performance constraints. Also, given that the developed models can predict the power output and the system efficiency, studies on the cost of power production can be performed.

BIBLIOGRAPHY

BIBLIOGRAPHY

[1] *Communication with UTRC*, 2004.

[2] *Communication with SOFCo-EFS*, 2005.

[3] Parag Adhangale and David Keffer. A grand canonical monte carlo study of the adsorption of methane, ethane, and their mixtures in one-dimensional nanoporous materials. *Langmuir, 18*, pages 10455–10461, 2002.

[4] P. Aguiar, C.S. Adjiman, and N.P. Brando. Anode-supported intermediate temperature direct internal reforming solid oxide fuel cell i: model-based steady-state performance. *Journal of Power Sources*, (Vol. 138, 120-136), 2004.

[5] Karnik Amey, Sun Jing, and Buckland Julia. Control analysis of an ejector based fuel cell anode recirculation system. *Proceedings of the American Control Conference*, (484-489), 2006.

[6] S. F. Au, S. J. McPhail, N. Woudstra, and K. Hemmes. The influence of operating temperature on the efficiency of a combined heat and power fuel cell plant. *Journal of Power Sources*, (Vol. 122, 37-46), 2003.

[7] F. Barbir and T. Gomez. Efficiency and economics of proton exchange membrane fuel cells. *Int. Journal of Hydroqen Energy*, (Vol. 22, 1027-1037), 1997.

[8] P. Beckhaus, A. Heinzel, J. Mathiak, and J. Roes. Dynamics of h_2 production by steam reforming. *Journal of Power Sources 127 pp.294-299*, 2004.

[9] Shyamal K. Bej. Revamping of diesel hydrodesulfurizers: Options available and future research needs. *Fuel Processing Technology 85*, (1503-1517), 2004.

[10] F. Calisea, M. Dentice d'Accadia, A. Palombo, and L. Vanoli. Simulation and exergy analysis of a hybrid solid oxide fuel cell (sofc)gas turbine system. *Energy*, (Vol. 31/32783299), 2006.

[11] S. Cavallaro and S. Freni. Ethanol reforming in a molten carbonate fuel cell. *Iht. J. Hydrogen Energy Vol. 21, No. 6, pp. 465-469*, 1996.

[12] S.H. Chan and H.M. Wang. Thermodynamic and kinetic modelling of an autothermal methanol reformer. *Journal of Power Sources 126 pp.8-15*, 2004.

[13] A.K. Chaniotis and D. Poulikakos. Modeling and optimization of catalytic partial oxidation methane reforming for fuel cells. *Journal of Power Sources 142 pp.184-193*, 2005.

[14] Tsang-Dong Chung, Yau-Pin Chyou, Wen-Tang Hong, Yung-Neng Cheng, and Kin-Fu Lin. Influence of energy recuperation on the efficiency of a solid oxide fuel cell power system. *Energy and Fuels*, (Vol. 21, 314-321), 2007.

[15] A.L. Dicks. Hydrogen generation from natural gas for the fuel cell systems of tomorrow. *Journal of Power Sources*, 61:113–124, 1996.

[16] M.Y. El-Sharkh, A. Rahman, M.S. Alam, P.C. Byrne, A.A. Sakla, and T. Thomas. A dynamic model for a stand-alone pem fuel cell power plant for residential applications. *Journal of Power Sources 138 pp.199-204*, 2004.

[17] A. Ersoz, H. Olgun, S. Ozdogan, C. Gungor, F. Akgun, and M. Trs. Autothermal reforming as a hydrocarbon fuel processing option for pem fuel cell. *Journal of Power Sources 118 pp.384-392*, 2003.

[18] J.S. Freudenberg. A first graduate course in feedback control, 2002. University of Michigan, EECS 565 Coursepack.

[19] T.H. Gardner, D.A. Berry, K.D. Lyons, S.K. Beer, and A.D. Freed. Fuel processor integrated H_2S catalytic partial oxidation technology for sulfur removal in fuel cell power plants. *Fuel*, 81:2157–2166, 2002.

[20] Todd H. Gardner, David A. Berry, Kenneth David Lyons, Stephen K. Beer, and Adam D. Freed. Fuel processor integrated h2s catalytic partial oxidation technology for sulfur removal in fuel cell power plants. *Fuel Magazine 81 pp.2157-2166*, 2002.

[21] Union Gas. Natural gas properties. *http://www.uniongas.com*.

[22] H. K. Geyer, R. K. Ahluwalia, and R. Kumar. Dynamic response of steam reformed, mathanol fueled polymer electrolyte fuel cell systems. *IEEE 0-780:3-3547-3-7/16*, 1996.

[23] E. G. Gilbert and Ilya Kolmanovsky. Discrete-time reference governors for systems with state and control constraints and disturbance inputs. *Proceedings of the Conference on Decision and Control*, (Vol. 2, 1189-1194), 1995.

[24] R. W. Glazebrook. Efficiencies of heat engines and fuel cells:the methanol fuel cell as a competitor to otto and diesel engines. *Journal Of Power Sources*, (Vol. 7, 215-256), 1982.

[25] Haluk Gorgun, Murat Arcak, Subbarao Varigonda, and Scott Bortoff. Observer designs for fuel processing reactors in fuel cell power systems. *International Journal of Hydrogen Energy, 30*, (447-457), 2005.

[26] Haluk Gorgun, Murat Arcak, Subbarao Varigonda, and Scott A. Bortoff. Observer designs for fuel processing reactors in fuel cell power systems. *International Journal of Hydrogen Energy 30 pp.447-457*, 2005.

[27] Comas Haynes. Clarifying reversible efciency misconceptions of high temperature fuel cells in relation to reversible heat engines. *Journal of Power Sources*, (Vol. 92, 199-203), 2001.

[28] W. He and Kas Hemmes. Operating characteristics of a reformer for molten carbonate fuel-cell power-generation systems. *Fuel Processing Technology 67, pp.61-78*, 2001.

[29] Theophilos Ioannides. Thermodynamic analysis of ethanol processors for fuel cell applications. *Journal of Power Sources 92 pp.17-25*, 2001.

[30] H.J. Jahn and W. Schroer. Mathematical model of a residential fuel cell power plant and its application to start up optimisation. *Fuel Cells Magazine, 4, No.4*, 2004.

[31] T. Katrasnik, S. Rodman, and F. Trenc. Improvement of the dynamic characteristic of an automotive engine by a turbocharger assisted by an electric motor. *Transactions of the ASME*, (Vol. 125, 590-595), 2003.

[32] Hassan Khalil. *Nonlinear Systems*. 3rd Edition, Prentice Hall, 2002.

[33] Shinji Kimijima and Nobuhide Kasagi. Cycle analysis of micro gas turbine molten carbonate fuel cell hybrid system. *JSME International Journal*, (Vol. 48, 65-74), 2005.

[34] Ilya Kolmanovky, Elmer Gilbert, and Kok Tan. Nonlinear control of discrete time linear systems with state and control constraints: A reference governor with global convergence properties. *Proceedings of the IEEE Conference on Decision and Control*, (Vol. 1, 144-149), 1994.

[35] Ilya Kolmanovky and Jing Sun. A multi-mode switching-based command tracking in network controlled systems with pointwise-in-time constraints and disturbance inputs. *Proceedings of the World Congress on Intelligent Control and Automation*, (Vol. 1, 199-204), 2006.

[36] Prapan Kuchonthara, Sankar Bhattacharya, and Atsushi Tsutsumi. Energy recuperation in solid oxide fuel cell (sofc) and gas turbine (gt) combined system. *Journal Of Power Sources*, (Vol. 117, 7-13), 2003.

[37] Prapan Kuchonthara, Sankar Bhattacharya, and Atsushi Tsutsumi. Energy recuperation in solid oxide fuel cell (sofc) and gas turbine (gt) combined system. *Journal of Power Sources*, (Vol. 117 / 713), 2003.

[38] J. Lampert. Selective catalytic oxidation: a new catalytic approach to the desulfurization of natural gas and liquid petroleum gas for fuel cell reformer applications. *Journal of Power Sources 131 pp.27-34*, 2004.

[39] A.L. Larentis, N.S. de Resende, V.M.M. Salim, and J.C. Pinto. Modeling and optimization of the combined carbon dioxide reforming and partial oxidation of natural gas. *Applied Catalysis*, 215:211–224, 2001.

[40] James Larminie and Andrew Dicks. *Fuel Cell Systems Explained*. John Wiley & Sons Inc, West Sussex, England, 2000.

[41] Bard Lindstrom and Lars J. Pettersson. Hydrogen generation by steam reforming of methanol over copper-based catalysts for fuel cell applications. *International Journal of Hydrogen Energy 26 pp.923-933*, 2001.

[42] Zhong-Wen Liu, Jun Ki-Won, Roh Hyun-Seog, and Park Sang-Eon. Hydrogen production for fuel cells through methane reforming at low temperatures. *Journal of Power Sources 111 pp.283-287*, 2002.

[43] Ahmet Lokurlu, Thomas Grube, Bernd Hohlein, and Detlef Stolten. Fuel cells for mobile and stationary applicationscost analysis for combined heat and power stations on the basis of fuel cells. *International Journal of Hydrogen Energy*, (Vol. 28, 703-711), 2003.

[44] Michael D. Lukas, Kwang Y. Lee, and Hossein Ghezel-Ayagh. An explicit dynamic model for direct reforming carbonate fuel cell stack. *IEEE Transactions On Energy Conversion, Vol. 16, No. 3,*, 2001.

[45] W. L. Lundberg, S. E. Veyo, and M. D. Moeckel. A high-efficiency solid oxide fuel cell hybrid power system using the mercury 50 advanced turbine systems gas turbine. *Journal of Engineering for Gas Turbines and Power*, (Vol. 125/51), 2003.

[46] A. F. Massardo and F. Lubelli. Internal reforming solid oxide fuel cell-gas turbine combined cycles (irsofc-gt): Part acell model and cycle thermodynamic analysis. *Journal of Engineering for Gas Turbines and Power*, (Vol. 122 / 27-35), 2000.

[47] J. Mathiak, Heinzel A., Roes J., Kalk Th., H. Kraus, and Brandt H. Coupling of a 2.5 kw steam reformer with a 1 kw_{el} pem fuel cell. *Journal of Power Sources 131 pp.112-119*, 2004.

[48] J. D. Naber, D. L. Siebers, S. S. Di Julio, and C. K. Westbrook. Effects of natural gas composition on ignition delay under diesel conditions. *Combustion and Flame, 99*, pages 192–200, 1994.

[49] Dirk Neumann and Gotz Veser. Catalytic partial oxidation of methane in a high-temperature reverse-flow reactor. *AIChE Journal, Vol. 51, No. 1*, 2005.

[50] Joan M. Ogden, Steinbugler Margaret M., and Kreutz Thomas G. A comparison of hydrogen, methanol and gasoline as fuels for fuel cell vehicles: implications for vehicle design and infrastructure development. *Journal of Power Sources 79 pp.143168*, 1999.

[51] Jens Palsson, Azra Selimovic, and Lars Sjunnesson. Combined solid oxide fuel cell and gas turbine systems for efficient power and heat generation. *Journal of Power Sources*, (Vol. 86 / 442448), 2000.

[52] Panos Papalambros and Douglass Wilde. *Principles of Optimal Design: Modeling and Computation.* Cambridge University Press, 2nd edition, 2000.

[53] J. Pasel, J. Meissner, Z. Pors, C. Palm, P. Cremer, R. Peters, and J. Stolen. Hydrogen production via autothermal reforming of diesel fuel. *Fuel Cells WILEY-VCH Verlag GmbH, 4, No.3*, 2004.

[54] R. Peters, R. Dahl, U. Kluttgen, C. Palm, and D. Stolten. Internal reforming of methane in solid oxide fuel cell systems. *Journal of Power Sources 106 pp.238-244*, 2002.

[55] R. Peters, H.G. Dusterwald, and B. Hohlein. Investigation of a methanol reformer concept considering the particular impact of dynamics and long-term stability for use in a fuel-cell-powered passenger car. *Journal of Power Sources 86 pp.507-514*, 2000.

[56] Power and Energy Website. www.powerandenergy.com. 2007.

[57] Jay T. Pukrushpan, Anna G. Stefanopoulou, and Huei Peng. Control of fuel cell breathing. *IEEE Control Systems Magazine*, (0272-1708), 2004.

[58] Jay Tawee Pukrushpan. *Modeling and Control of Fuel Cell Systems and Fuel Processors*. PhD thesis, University of Michigan, 2003.

[59] Jay Tawee Pukrushpan, Anna Stefanopoulou, and Huei Peng. *Control of Fuel Cell Power Systems : Principles, Modeling, Analysis and Feedback Design*. Springer, 1st edition, 2004.

[60] J.T. Pukrushpan, A.G. Stefanopoulou, and S. Varigonda. Control-oriented model of fuel processor for hydrogen generation in fuel cell applications. *IFAC Symposium on Advances in Automotive Control*, April 2004.

[61] R. A. Roberts and J. Brouwer. Dynamic simulation of a pressurized 220 kw solid oxide fuel-cell/gas-turbine hybrid system: Modeled performance compared to measured results. *Transactions of the ASME*, (Vol. 3 / 18-25), 2006.

[62] Wakeman Russell and Wright Danny. Closed loop turbocharger control with transient wastegate functions. *SAE Special Publications*, (131-135), 1986.

[63] J.L. Silveira and L.A. Gomes. Fuel cell cogeneration system, a case of technoeconomic analysis. *Renewable and Sustainable Energy Reviews*, (Vol. 3, 233-242), 1999.

[64] Marc Sommer, Arnold Lamm, Andreas Docter, and David Agar. Modelling and dynamic simulation of a fuel cell system with an autothermal gasoline reformer. *Journal of Power Sources 127 pp.313-318*, 2004.

[65] Chunshan Song. An overview of new approaches to deep desulfurization for ultra-clean gasoline, diesel fuel and jet fuel. *Catalysis Today 86*, (211263), 2003.

[66] Rak-Hyun Song, Chao-Soo Kim, and Dong Ryul Shin. Effects of flow rate and starvation of reactant gases on the performance of phosphoric acid fuel cells. *International Journal of Power Sources, 86*, (289-293), 2000.

[67] Tae Won Song, Jeong Lak Sohna, Tong Seop Kim, and Sung Tack Ro. Performance characteristics of a mw-class sofc/gt hybrid system based on a commercially available gas turbine. *Journal of Power Sources*, (Vol. 158 / 361-367), 2006.

[68] S. Springmann, M. Bohnet, A. Docter, A. Lamm, and G. Eigenberger. Cold start simulations of a gasoline based fuel processor for mobile fuel cell applications. *Journal of Power Sources 128 pp.13-24*, 2002.

[69] A.G. Stefanopoulou and I. Kolmanovsky. Analysis and control of transient torque response in engines with internal exhaust gas recirculation. *, IEEE Transactions on Control System Technology, Vol.7, No.5*, (555-566), 1999.

[70] Christoph Stiller, Bjrn Thorud, and Olav Bolland. Safe dynamic operation of a simple sofc/gt hybrid system. *Journal of Engineering for Gas Turbines and Power*, (Vol. 128 / 551-559), 2006.

[71] Christoph Stiller, Bjrn Thorud, Olav Bolland, Rambabu Kandepu, and Lars Imsland. Control strategy for a solid oxide fuel cell and gas turbine hybrid system. *Journal of Power Sources*, (Vol. 158 / 303315), 2006.

[72] Jie Sun, Xinping Qiu, Feng Wu, Wentao Zhu, Wendong Wang, and Shaojun Hao. Hydrogen from steam reforming of ethanol in low and middle temperature range for fuel cell application. *International Journal of Hydrogen Energy 29 pp.1075-1081*, 2004.

[73] Jing Sun and Ilya Kolmanovsky. A robust load governor for fuel cell oxygen starvation protection. *American Control Conference*, June 2004.

[74] Kiyotaka Takeda, Akihiro Baba, Yukio Hishinuma, and Takemi Chikahisa. Performance of a methanol reforming system for a fuel cell powered vehicle and system evaluation of a pefc system. *JSAE Review 23 pp.183-188*, 2002.

[75] Kinya Tawara and Takeshi Nishimura. New hydrodesulfurization catalyst for petroleum-fed fuel cell vehicles and cogenerations. *Ind. Eng. Chem. Res., 40, 2367-2370*, 2001.

[76] V. Tsourapas, J. Sun, and A. Stefanopoulou. Modeling and dynamics of a fuel cell combined heat power system for marine applications. *IASME Transactions*, 2(1):287–293, 2004.

[77] V. Tsourapas, J. Sun, and A. Stefanopoulou. Dynamics, optimization and control of a fuel cell based combined heat power (chp) system for shipboard applications. *American Control Conference*, 2005.

[78] Vasilis Tsourapas, Anna Stefanopoulou, and Jing Sun. Model-based control of an integrated fuel cell and fuel processor with exhaust heat recirculation. *Control Systems Technology, IEEE Transactions*, (Vol. 15, Issue 2, 233245).

[79] Vasilis Tsourapas, Jing Sun, and Anthony Nickens. Control oriented modeling and analysis of a hybrid solid oxide fuel cell and gas turbine (sofc/gt) system. *Fuel Cell Seminar*, (212-216), 2006.

[80] Hideyuki Uechi, Shinji Kimijima, and Nobuhide Kasagi. Cycle analysis of gas turbinefuel cell cycle hybrid micro generation system. *Journal of Engineering for Gas Turbines and Power*, (Vol. 126 / 755-762), 2004.

[81] Ardelan Vahidi, Anna Stefanopoulou, and Huei Peng. Model predictive control for starvation prevention in a hybrid fuel cell system. *American Control Conference*, (834-839), 2004.

[82] S. Varigonda and S. A. Bortoff. Multivariable control design for the water gas shift reactor in a fuel processor. *American Control Conference*, 2004.

[83] Tsourapas Vasilis, Stefanopoulou Anna G, and Sun Jing. Model-based control of an integrated fuel cell and fuel processor with exhaust heat recirculation. *IEEE Transactions on Control Systems Technology*, (Vol. 15, 233-245), 2007.

[84] Christian Wchter, Reinhart Lunderstdt, and Franz Joos. Dynamic model of a pressurized sofc/gas turbine hybrid power plant for the development of control concepts. *Journal of Fuel Cell Science and Technology*, (Vol. 3 / 271-279), 2006.

[85] W. Wiese, B. Emonts, and R. Peters. Methanol steam reforming in a fuel cell drive system. *Journal of Power Sources 84 pp.187193*, 1999.

[86] Handa Xi. Dynamic modeling and control of planar sofc power systems. *University of Michigan, Department of Naval Architecture and Marine Engineering, Ph.D. Thesis*, 2007.

[87] Handa Xi, Jing Sun, and Vasilios Tsourapas. A control oriented low order dynamic model for planar sofc using minimum gibbs free energy method. *Journal of Power Sources*, (Vol. 165 / 253266), 2007.

[88] Masanori Yamaguchi, Tadayoshi Saito, Minoru Izumitani, Shigehisa Sugita, and Yasuyuki Tsutsumi. Analysis of control characteristics using fuel cell plant simulator. *IEEE Transactions on Industrial Electronics, Vol. 31, No. 5*, 1990.

[89] W.J. Yang, S.K. Park, T.S. Kim, J.H. Kim, J.L. Sohn, and S.T. Ro. Design performance analysis of pressurized solid oxide fuel cell/gas turbine hybrid systems considering temperature constraints. *Journal of Power Sources*, (Vol. 160 462-473), 2006.

[90] Yaofan Yi, Ashok D. Rao, Jacob Brouwer, and G. Scott Samuelsen. Analysis and optimization of a solid oxide fuel cell and intercooled gas turbine (sofcicgt) hybrid cycle. *Journal of Power Sources*, (Vol. 32 77-85), 2004.

[91] J.C. Zhang, L.F. Song, J.Y. Hu, S.L. Ong, W.J. Ng, L.Y. Lee, Y.H. Wang, J.G. Zhao, and R.Y Ma. Investigation on gasoline deep desulfurization for fuel cell applications. *Energy Conversion and Management No.4*, 2004.

[92] J. Zhu, D. Zhang, and K.D. King. Reforming of CH_4 by partial oxidation: thermodynamic and kinetic analyses. *Fuel*, 80:899–905, 2001.